Astron. Astrophys. 305, 171–208 (1996)

ASTRONOMY AND ASTROPHYSICS

# O-star mass-loss and wind momentum rates in the Galaxy and the Magellanic Clouds

## Observations and theoretical predictions*

**J. Puls[1], R.-P. Kudritzki[1,2], A. Herrero[3], A.W.A. Pauldrach[1], S.M. Haser[1], D.J. Lennon[1], R. Gabler[1], S.A. Voels[4], J.M. Vilchez[3], S. Wachter[5], and A. Feldmeier[1]**

[1] Universitäts-Sternwarte München, Scheinerstr. 1, D-81679 München, Germany
[2] Max-Planck-Institut für Astrophysik, Karl-Schwarzschild-Str. 1, D-85740 Garching, Germany
[3] Instituto de Astrofisica de Canarias (IAC), La Laguna, Tenerife, Spain
[4] Goddard Space Flight Center, Greenbelt, MD 20771, USA
[5] University of Washington, Department of Astronomy,FM-20, Seattle, WA 98195, USA

Received 27 January 1995 / Accepted 12 April 1995

**Abstract.** A new, very fast approximate method is presented to determine mass-loss rates of O-stars from $H_\alpha$ line profiles. The method uses H and HeII departure coefficients from unified model atmospheres parametrized in a simple way as function of wind velocity together with photospheric NLTE line profiles as the inner boundary condition for a numerically exact radiative transfer solution to derive a wind contaminated $H_\alpha$ -profile. The method is also applied to $H_\gamma$ to determine stellar gravities corrected for wind emission.

A detailed analytical discussion of $H_\alpha$ line formation in O-star winds is given and it is demonstrated that former very simple approaches considering only optically thin wind emission lead to significant systematic errors. Scaling relations and generalized curves of growth are presented that connect mass-loss rate, terminal velocity, stellar parameters and $H_\alpha$ equivalent width.

The method is applied to samples of O-stars in the Galaxy, LMC and SMC and mass-loss rates are derived from $H_\alpha$ in combination with terminal velocities measured from IUE and HST spectra. The results reveal that a tight empirical relation exists between the radius modified stellar wind momentum rate $\dot{M}v_\infty R_*^{0.5}$ and the stellar luminosity. The variations of this relationship between the Galaxy, LMC and SMC are explained in terms of different abundances. Furthermore, for almost all objects with dense winds (mostly supergiants), the commonly used velocity field exponent $\beta$ could be *derived*, indicating a typical value of $\beta \approx 1$.

A comparison with the improved theory of radiation driven winds (as presented recently by Pauldrach et al. 1994) shows that the observed wind momentum-luminosity relationship can be understood qualitatively in terms of the theory. However, there exist significant systematic discrepancies as a function of effective temperature, luminosity class and wind performance number $\eta = \dot{M}v_\infty c/L$. We stress that these discrepancies would not have been detected with previous simplified $H_\alpha$ -approaches.

The deficiencies of the theory are discussed and suggestions for future improvements are made.

**Key words:** line: formation – stars: atmospheres – stars: distances – stars: early-type – stars: mass-loss – Magellanic Clouds

## 1. Introduction

Mass-loss is ubiquitous during the evolution of massive stars. It is the keystone to understanding the transition from the zero age main sequence to the Wolf-Rayet stage through phases of Of-stars, supergiants, Ofpe/WN-stars, Luminous Blue Variables etc. (for a recent rediscussion of the evolutionary scenario see Langer et al. 1994). Moreover, since the strength of mass-loss is obviously correlated with the stellar parameters, in particular the luminosity, this correlation can in principle be utilized to determine distances to massive luminous stars in other galaxies. Kudritzki et al. (1992), for instance, have used the theory of radiation driven winds to determine stellar masses, radii and distances from the observed values of mass-loss rate and ter-

*Send offprint requests to*: J. Puls (first address above)

* based upon observations made with the NASA/ESA Hubble Space Telescope, obtained at the Space Telescope Science Institute which is operated by the Association of Universities for Research in Astronomy, Inc., under NASA grant NAS 5-26555. Also based upon data obtained at the European Southern Observatory, La Silla, Chile and on observations made with the INT operated on the island of La Palma by the RGO in the Spanish Observatorio del Roque de los Muchachos of the Instituto de Astrofisica de Canarias.

minal velocity of the winds of massive stars. Consequently, the precise determination of mass-loss rates is extremely important.

In this connection it has become clear that for O-stars an accurate and also versatile method is to use the strength of the stellar wind emission in $H_\alpha$ (Klein & Castor 1978; Leitherer 1988/1988a). In this method, the observed equivalent width of $H_\alpha$ is corrected for "photospheric absorption" by subtracting the equivalent width of a synthetic $H_\alpha$ line formed in a hydrostatic model atmosphere (with appropriate $T_{\rm eff}$ and $\log g$) to yield the equivalent width of the stellar wind emission. This latter value is then analytically transformed into a mass-loss rate via the equation of continuity assuming optically thin line emission, a constant value of the departure coefficient $b_3$ of the third level of hydrogen plus a constant ratio of wind temperature $T_e$ to effective temperature $T_{\rm eff}$ and a "$\beta$-type" velocity law.

The advantage of this method is that its application is straightforward and easy and that it is certainly more accurate than the use of UV resonance lines, where the ionization correction is still a source of large uncertainty. Very recently, Lamers & Leitherer (1993, "L&L") have used this method to redetermine the mass-loss rates of galactic O-stars. They have also tested the theory of radiation driven winds using the analytical approach by Kudritzki et al. (1989) and radiative line force parameters as published by Pauldrach et al. (1990). The result they found was a possible defect of the theory is not predicting enough stellar wind momentum with increasing "wind performance number" $\eta = \dot{M} v_\infty c/L$.

The disadvantage of the method is that it uses only the observed *equivalent width* and not the line *profile*, wasting important information, e.g. about the shape of the velocity field (the "$\beta$"- exponent). Moreover, in the context of the optically thin approximation, the consideration of line *emission* only and the neglect of line *absorption* is certainly incorrect, as we shall show below (see Sect. 2.2.1). In addition, $H_\alpha$ is never *completely* optically thin throughout the wind (in particular in cases of dense winds), and the simple subtraction of a photospheric equivalent width may be too simple, if precision is required. Finally the assumption of constant departure coefficients might introduce additional errors.

A more consistent and precise approach is the concept of "unified model atmospheres" as introduced by Gabler et al. (1989, 1990) and recently improved by Sellmaier et al. (1993) and Schaerer & Schmutz (1994). In this approach, hydrodynamical atmospheres with a smooth transition between the sub- and supersonic layers are used together with the correct multi-line NLTE radiative transfer in the comoving frame to calculate $H_\alpha$ profiles. However, the effort to calculate such atmospheric models is huge and, since a wide parameter space ($T_{\rm eff}$, $\log g$, $N({\rm He})/N({\rm H})$, $\dot{M}$, $R_*/R_\odot$, $v_\infty$, shape of velocity field) has to be investigated per star, the investigation of a large sample of objects by this approach is difficult.

Therefore, we introduce in this paper a compromise which combines the advantages of the "unified model atmospheres" with the simplicity of the original "core-halo $H_\alpha$ concept" by Klein & Castor (1978) and Leitherer (1988). The idea is very simple. We use unified model atmospheres to parametrize the run of hydrogen ($b_2, b_3, b_4, b_5$) and ionized helium ($b_4, b_6, b_8, b_{10}$) departure coefficients as function of depth in the supersonic atmosphere. This parametrization is then applied to solve the exact equation of transfer for the $H_\alpha$/HeII, $H_\beta$/HeII and $H_\gamma$/HeII line profile blends in the expanding stellar wind assuming an incident hydrostatic NLTE line profile as the inner boundary condition. This procedure needs only a few seconds per profile on a work station and leads to results almost indistinguishable from unified model atmosphere calculations.

In Sect. 2, we introduce this method together with a detailed discussion of analytical solutions and resulting scaling relations. Moreover, we discuss the dependence on the HeII blend, on the $\beta$-exponent, on the electron temperature, on $v_\infty$ and present a generalized curve of growth.

Then, in Sect. 3, we apply our new method to determine mass-loss rates and $\beta$-exponents from $H_\alpha$ for O-stars in the Galaxy and the Magellanic Clouds. We use terminal velocities determined from UV-resonance line fits obtained from IUE and HST spectra. The method is also used to correct for wind emission in $H_\gamma$ for the determination of stellar gravities. We compare with the previous work and conclude that the use of line *profiles* (vs. their equivalent widths) and the relaxation of the optically thin approximation is a significant improvement.

In Sect. 4 we discuss the wind momentum-luminosity relation of O-stars. Solving analytically the hydrodynamic equations of radiation driven winds, we show that such a relation must exist if the basic concept of the theory is correct. This conclusion is nicely confirmed by the observations, which also indicate, as expected, a trend with metallicity. We then reinvestigate whether the theory in its improved form with additional metal line opacities (see Pauldrach et al. 1994) still has quantitative defects, as found previously by Lamers & Leitherer (1993).

## 2. H-alpha line formation

### *2.1. General assumptions and approximations*

In the following subsection, we will describe our basic assumptions and approximations which are used to derive mass-loss rates from $H_\alpha$ .

#### 2.1.1. Hydrodynamical structure

In the present paper, the stellar wind is assumed to be *stationary, smooth* (i.e., no shocks and no clumps) and *spherically symmetric*.

*Stationarity.* The intention of this paper is to derive time averaged rates of mass-loss based on the *mean* atmospheric situation (i.e., average density, velocity and ionization/excitation stratification). We are confident that this concept is reasonable, since the observed degree of line profile variability (both optical and UV) is neglegible on time-scales longer than the wind flow times. Of course, this statement is not true for the few cases of observed dramatic changes in spectral appearance, as for LBVs such as R127 (Stahl et al. 1983)

*Smooth flow.* It is now generally accepted that the winds around hot stars have a time-dependent and inhomogeneous structure consisting of shocks, clumps and blobs. The observational evidence for this comes from the presence of black and broad troughs in saturated UV P Cygni profiles (Lucy 1982; Puls et al. 1993, 1995) and the X-ray emission of hot stars (e.g. Chlebowski et al. 1989 and references therein, Hillier et al. 1993; Cassinelli et al. 1994). Moreover, some direct evidence for clumping in the *outer* parts of Wolf-Rayet winds is provided by the observations and analyses of distinct blobs (e.g. Robert & Moffat 1990). In terms of theory, shocks and wind inhomogeneities are induced by the intrinsic instabilities of radiation driven winds (cf. Owocki 1992 and references therein; Feldmeier 1995).

Therefore, at first glance, the assumption of a stationary wind without clumping seems questionable, particularly as the $H_\alpha$ opacity/emissivity scales with the square of the density (the influence of this principal effect was firstly discussed by Abbott et al. 1981 and Lamers & Waters 1984). On the other hand, the wind emission contribution to $H_\alpha$ for O-stars comes from lower wind layers, typically between 1.0 and 1.5 stellar radii. Very recent hydrodynamical simulations for *self-excited* wind instabilities show that these layers are unaffected by shocks and that instabilities only occur further out in the wind (Owocki 1995). This agrees with the fact that the observed X-rays most probably also arise in the outer layers (see Hillier et al. 1993) and that the broad absorption troughs in saturated P Cygni profiles can also be interpreted as arising from small-scale structures in the *outer* wind (Owocki 1995).

Nevertheless, instabilities producing a small density contrast might still be present in the $H_\alpha$ forming region, *if* the wind is triggered by photospheric perturbations (sound waves, non-radial pulsations, "strange mode" oscillations). In such cases the location of the onset of structure formation depends crucially on the damping by the diffuse radiation force (Lucy 1984; Owocki & Rybicki 1985) which in present simulations is only approximated (Owocki 1991; Feldmeier 1995). However, almost all recent hydrodynamical simulations including photospheric perturbations show pronounced inhomogenious structures only above 1.5 stellar radii. Therefore we conclude that the neglect of clumping does most probably not induce large systematic errors for *O-star* mass-loss determinations. (For WR-winds, the situation seems to be different, since the analysis of the mass spectrum of the observed blobs implies a factor three overestimate in the mass-loss derived from IR and radio observations, cf. Moffat & Robert 1994).

A second line of reasoning in favour of our assumption was given by L&L and Puls et al. (1993a). Briefly, they have argued that because of the same $\rho^2$ dependency of both the radio and the $H_\alpha$ emission and the fact that both rates agree for those objects with $H_\alpha$ *and* radio mass-loss rates , this would imply the same clumping factor in regions close to ($H_\alpha$ ) and far away from the star (radio). As this is rather unlikely, since in the lower wind the formation of structure just sets in, whereas in the outer part any structure should have stabilized, it is most probable that the degree of clumping in the lower wind part is small, if present at all, and will not affect the derived values of mass-loss rates.

*Spherical symmetry.* In the following, we will assume a spherically symmetric density stratification and velocity field. This assumption is well justified at least for objects with a small rotational velocity ($v \sin i \lesssim 100$ km/s) both because in this case the resulting polar variation of the *effective* gravity is weak and the observed intrinsic polarisation in those objects is small (e.g. Hayes 1975; Lupie et al. 1987). The only effect which has to be accounted for is the influence of the average centrifugal correction on the stellar mass (cf. also Herrero et al. 1992).

For stars with a large rotational rate, the effects of an explicitly two-dimensional density structure (cf. Bjorkmann & Cassinelli 1993) have still to be explored, so that the derived mass-loss rates are only order of magnitude results.

### 2.1.2. Core-halo structure, Stark broadening and rotation

*Core-halo structure.* In contrast to a consistent "unified atmosphere" approach (Gabler et al. 1989; Schaerer & Schmutz 1994), which avoids any artificial division between photosphere and wind, our treatment explicitly comprises only the line formation in the wind. However, the underlying photospheric profile (calculated by means of plane-parallel NLTE atmospheres (Giddings 1980; Butler & Giddings 1985; Husfeld et al. 1989) is taken into account consistently, i.e., as lower boundary in the transfer algorithm and not only as an additional constant to correct the equivalent width of the wind profile. The continuum at the frequencies of the Balmer lines is adopted to be optically thin in the wind, which is a good approximation for O-stars but fails for WR-stars. We will, however, use reliable photospheric continuum fluxes approximated by radiation temperatures taken from unified model atmospheres.

*Stark broadening.* In our above approach of line formation, the Stark broadening of $H_\alpha$ and the neighbouring HeII blend is accounted for in the photospheric "input" profiles, whereas the line profile in the wind is assumed to be only Doppler broadened. Since Stark broadening becomes effective for electron densities $\gtrsim 10^{13}\mathrm{cm}^{-3}$, whereas the electron density in the sonic region of typical O-star winds is of the order of a few $10^{12}\mathrm{cm}^{-3}$, this approximation is acceptable as long as the *different pressure* at which the Stark wings are formed either in a hydrostatic or in an expanding atmosphere is accounted for. The procedure to fulfil this restriction is discussed in Sect. 3.1.2.

*Rotation.* In the present paper, we have neglected the influence of the *differential* rotation on the line formation process. The stellar rotation is here accounted for by a *final* convolution of the emergent profile with the rotational profile for the *photospheric* value of $v \sin i$. Although this approximation may fail for intermediate wind densities, it should give satisfying results both for thin winds (where the line is formed very close to the photosphere) and thick winds (where the wings become almost

independent on any normalized convolution). In a forthcoming paper (Petrenz & Puls, in prep.), we will discuss the influence of the differential rotation in detail. Test calculations (cf. also Schaerer & Schmutz 1994) indicate that the major effect arises for profiles with an equivalent width around zero (which together with a large $v \sin i$ are *not* present in our sample). In any case the equivalent width is almost completely preserved even under differential rotation, since this process does not modify the number of photons emitted in the wind.

### 2.2. *Analytic treatment of the pure Hydrogen problem for constant departure coefficients*

Having discussed now our basic assumptions and approximations, we are turning to the actual problem of $H_\alpha$ line formation in typical O-star winds[1]. In order to understand the final results derived at the end of this section thoroughly – with special emphasis on the dependence of the equivalent width on the wind parameters – we will initially consider the pure Hydrogen problem, i.e., we neglect the He-blend. We will also assume constant departure coefficients for the hydrogen NLTE occupation numbers and constant electron temperatures, which is not too bad as we will see below. In addition, we will solve the radiative transfer in the Sobolev approximation. (All these simplifications will be dropped in Sects. 2.3 to 2.5 and more exact solutions will be presented there.)

In the Sobolev approximation and spherical symmetry, the optical depth $\tau$ of a resonance zone (with directional derivative $\mathrm{d}\,\mu v/\mathrm{d}\,z$ along impact parameter p) is given by

$$\tau = \frac{A}{r^4 v^2 \frac{\mathrm{d}\mu v}{\mathrm{d}z}} = \frac{A}{r^3 v^3 \left(1+\mu^2\sigma\right)} \tag{1}$$

where the radius $r$ is calculated in units of $R_*$ as well as p and z. $v$ is the velocity in units of the terminal velocity $v_\infty$, $\mu$ is the cosine of the angle between the photon's path and the velocity vector and the curvature parameter $\sigma$ measures the deviation from homogenous expansion (cf. Castor 1970):

$$\sigma = \mathrm{d}\,\ln\, v/\mathrm{d}\,\ln\, r - 1 \tag{2}$$

In the parameter $A$ we have absorbed all constants of the $H_\alpha$ transition and the wind parameters, and $A$ is given by

$$A = 49.30\, T_e^{-1.5} \left[ b_2 \exp\left(\frac{3.945}{T_e}\right) - b_3 \exp\left(\frac{1.753}{T_e}\right)\right] \times \times \frac{1+I_{\mathrm{He}}Y}{(1+4Y)^2}\,\frac{\dot{M}^2}{R_*^3 v_\infty^3}\,. \tag{3}$$

$b_{2,3}$ are here the *non-LTE* departure coefficients of the lower and upper level with respect to ionized hydrogen, $Y = n_{\mathrm{He}}/n_{\mathrm{H}}$ is the Helium abundance(by number) with respect to Hydrogen, $I_{\mathrm{He}}$ the number of free electrons provided per He atom (assumed to be 2 throughout this paper), $T_e$ the electron temperature in $10^4$ K, $\dot{M}$ the mass-loss rate in $10^{-6}\,\mathrm{M}_\odot$/yr, $R_*$ the stellar radius in $\mathrm{R}_\odot$ and $v_\infty$ the terminal velocity in 1000 km/s. For typical O-Star parameters, $A$ lies in the range from $10^{-7}$ to $10^{-1}$, so that in the largest part of the wind the transition is *optically thin* (cf. Eq. 1).

With the usual p-z geometry and taking into account that the receding part of the atmosphere can contribute only via non-core rays, the emergent residual line intensity $R_x$ measured by an observer in units of the continuum is given by

$$R_x(x>0) = \frac{\frac{1}{2}\int_0^1 P_x \mathrm{e}^{-\tau}\mathrm{d}p\,\mathrm{d}p + \frac{1}{2}\int_0^\infty \frac{S}{I_c}\left(1-\mathrm{e}^{-\tau}\right)\mathrm{d}p\,\mathrm{d}p}{\frac{1}{2}\int_0^1 \mathrm{d}p\,\mathrm{d}p} \tag{4}$$

$$R_x(x<0) = \frac{\frac{1}{2}\int_0^1 P_x\,\mathrm{d}p\,\mathrm{d}p + \frac{1}{2}\int_1^\infty \frac{S}{I_c}\left(1-\mathrm{e}^{-\tau}\right)\mathrm{d}p\,\mathrm{d}p}{\frac{1}{2}\int_0^1 \mathrm{d}p\,\mathrm{d}p}\,, \tag{5}$$

where we have assumed an optically thin continuum in the wind. $x$ is here the frequency displacement with respect to rest wavelength measured in units of maximum Doppler shift $x = \left(\nu/\nu_0 - 1\right)\, c/v_\infty$, $P_x$ the photospheric profile, $I_c = B_\nu(T_{\mathrm{rad}})$ the continuum intensity at $x = 0$ (assumed to be non-varying over the profile, $T_{\mathrm{rad}}$ the corresponding radiation temperature) and S the *NLTE* source function of the transition. Both the source function and the Sobolev optical depth have to be evaluated at the location of the corresponding resonance zone defined by

$$\mu v(z,p) = x. \tag{6}$$

Integrating over frequency, the equivalent width $W_\lambda$ (throughout this paper redefined to be *positive for net-emission*) can be expressed as the sum of three terms

$$W_\lambda = W_\lambda^{\mathrm{em}} + W_\lambda^{\mathrm{core}} + W_{\lambda,\mathrm{phot}}^{\mathrm{red}}\,, \tag{7}$$

where the first term gives the contribution from the emission lobes of the wind

$$W_\lambda^{\mathrm{em}} = 4\,\frac{v_\infty \lambda_0}{c}\int_0^1 \mathrm{d}x \int_1^\infty \frac{S}{I_c}\left(1-\mathrm{e}^{-\tau}\right)\mathrm{d}p\,, \tag{8}$$

the second term the contribution of the (absorbing and emitting) material in front of the stellar disk

$$W_\lambda^{\mathrm{core}} = 2\,\frac{v_\infty\lambda_0}{c} \times \times \left\{ \int_0^1 \mathrm{d}x \int_0^1 \left[\frac{S}{I_c} + \left(P_x - \frac{S}{I_c}\right)\mathrm{e}^{-\tau}\right]\mathrm{d}p - 1 \right\} \tag{9}$$

[1] The reader may note that an analogue investigation with respect to optically thin IR HeII line emission in optically thick WR-winds was performed by Hillier et al. (1983), however assuming a $\rho \sim r^{-2}$ dependence of the density which is valid in the line forming region under their consideration.

and $W_{\lambda,\rm phot}^{\rm red}$ is the equivalent width of the *red* part of the photospheric profile, which is *not* processed by the wind.

The reader may note that for $S \equiv I_c$ and $P_x \equiv 1$ (i.e., no photospheric profile) the emission/absorption processes in front of the stellar core completely cancel each other resulting in $W_\lambda^{\rm core} = 0$. Hence, in this case the total equivalent width depends exclusively on the emission in the lobes.

### 2.2.1. The optically thin approximation

Taking into account that $\tau$ is smaller than unity in a large part of the wind, Eqs. (8,9) may be expanded in $\tau$ to first order as

$$W_\lambda = W_\lambda^{\rm phot} + 2\,\frac{v_\infty \lambda_0}{c} \times \qquad (10)$$
$$\times \left\{ \int_0^1 {\rm d}x \left[ \int_0^\infty \frac{S}{I_c} \tau p {\rm d}p + \int_1^\infty \frac{S}{I_c} \tau p {\rm d}p - \int_0^1 P_x \tau p {\rm d}p \right] \right\}$$

where the first term is the *total* equivalent width of the photospheric profile. $S/I_c\,\tau$ can be expressed as

$$S/I_c\,\tau = \bar{b}_3\,\tau(b_{2,3} \equiv 1)$$
$$\bar{b}_3 = b_3\,\frac{{\rm e}^{h\nu_{\rm L}/kT_{\rm rad}} - 1}{{\rm e}^{h\nu_{\rm L}/kT_{\rm e}} - 1} \qquad (11)$$

where $\tau(b_{2,3} \equiv 1)$ is the optical depth for departure coefficients equal to unity (see Eqs. (1,3)). As we will show in the next sections, $b_3$ is not too different from unity and $T_{\rm rad}$ and $T_{\rm e}$ are quite similar. Also, $P_x$ (for O-stars) is close to unity (except for a small range of frequencies near $x \approx 0$), which means that all three integrands of Eq. (10) are of the same order. Interestingly, the third term in the parenthesis - which accounts for absorption of photospheric radiation by wind material in front of the stellar disc - has been neglected by Leitherer (1988) and L&L, who considered the optically thin pure wind emission only and derived their formula for the equivalent width in a different way. In our case, if we neglect the third integral and recall that the integration over $\int {\rm d}x \int \tau p {\rm d}p$ along the resonance zones ${\rm d}x = {\rm d}\mu v$ can be transformed to (cf. Eq. 1)

$$\int_0^1 {\rm d}x \int_{0,1}^\infty \tau(x,p) p {\rm d}p = \int_{0,1}^\infty p {\rm d}p \int_0^\infty \frac{A}{\left(r^4 v^2\right)(z,p)} {\rm d}z\,. \qquad (12)$$

and then switch to polar coordinates, we also recover Leitherer's (1988, Eq. 4) result

$$W_\lambda = 2\,\frac{v_\infty \lambda_0}{c}\,\bar{b}_3 A(b_{2,3} \equiv 1) \int_1^\infty (1 + \mu_*(r))\,\frac{{\rm d}r}{r^2 v(r)^2} +$$
$$+ W_\lambda^{\rm phot}\,, \qquad (13)$$

where $\mu_*(r) = (1 - 1/r^2)^{\frac{1}{2}}$ is the finite cone angle subtended by the stellar disk. By this equation the observed equivalent width

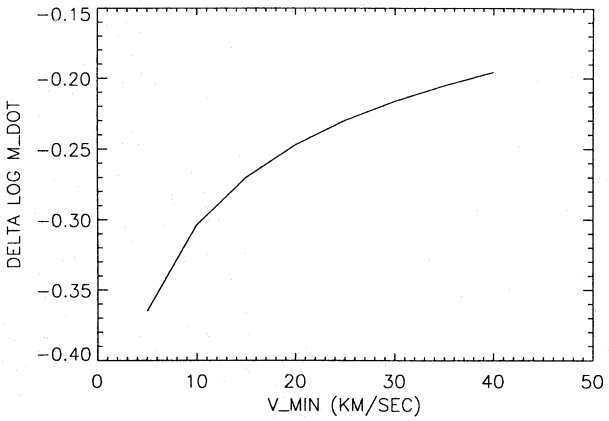


**Fig. 1.** Difference in the determination of $\log \dot{M}$ as function of $v_{\rm min}$ for a fixed value of observed equivalent width $W_\lambda'$, if Eq. (13) is used instead of Eq. (15). $\beta = 1$ and $v_\infty = 2{,}000$ km/s were adopted

(corrected for the photopheric profile) $W_\lambda' = W_\lambda^{\rm obs} + |W_\lambda^{\rm phot}|$ is immediately related to the mass-loss rate by

$$\log(W_\lambda') = \log\left(\frac{\dot{M}^2}{R_*^3 v_\infty^2}\right) + {\rm const}(T_e, \bar{b}_3, Y, \text{velocity field})\,. \qquad (14)$$

To estimate the error introduced by the neglect of the third term in Eq. (10), we adopt $S/I_c \approx P_x$, which then yields

$$W_\lambda = 4\,\frac{v_\infty \lambda_0}{c}\,\bar{b}_3 A(b_{2,3} \equiv 1) \int_1^\infty \frac{\mu_*(r){\rm d}r}{r^2 v(r)^2} + W_\lambda^{\rm phot}\,. \qquad (15)$$

The significant difference between Eqs. (13) and (15) is obvious. Using Eq. (15) instead of Eq. (13) leads to a different constant in the relation between observed equivalent width and mass-loss rate as given by Eq. (14).
Using a typical $\beta$ velocity field

$$v(r) = \left(1 - \frac{b}{r}\right)^\beta \qquad (16)$$

$$b = 1 - \left(\frac{v_{\rm min}}{v_\infty}\right)^{1/\beta} \qquad (17)$$

we can easily calculate the difference in $\log \dot{M}$ which results by applying either Eq. (13) or Eq. (15). An example is given in Fig. 1 indicating the error can be as large as a factor of 2.

However, Eq. (15) also repesents a rather inaccurate approach. This is demonstrated in Fig. 2, where the results of a *correct* radiative transfer calculation (solution of the formal integral in (p,z) geometry) is compared with those obtained by Eq. (15) and (13). Figure 2 also contains the results using the formal integral obtained from the Sobolev approximation (Eqs. 4,5) showing that for $\log(A) \lesssim -4$ the $H_\alpha$ wind contribution comes mostly from the region around the sonic point, where this approach inevitably fails (cf. e.g. Sellmaier et al. 1993). On the other hand, for $\log(A) > -4$ the SA results coincide perfectly

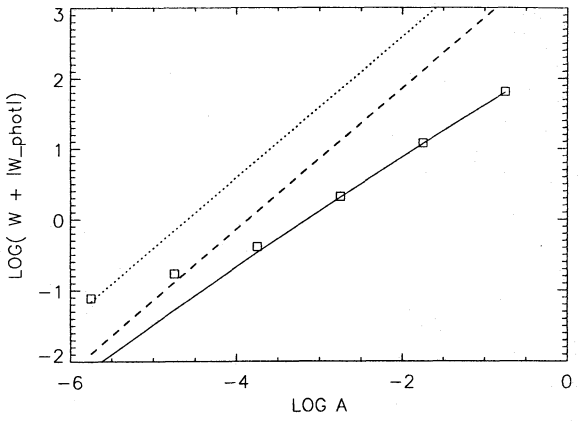


**Fig. 2.** Logarithm of $H_\alpha$ stellar wind equivalent width as function of mass-loss parameter $\log A$ (Eq. 3). Open rectangles: solution of *correct* radiative transfer; solid line: Sobolev approximation; dashed: optically thin approximation (Eq. 15); dotted: optically thin approximation (Eq. 13)

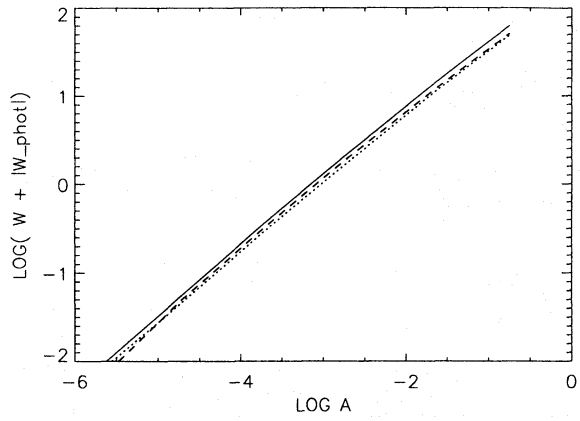


**Fig. 3.** As Fig. 2. Solid: Sobolev approximation; dashed: Sobolev approximation, taking into account only resonance zones with $\tau \leq 1$; dotted: approximation by Eq. (21)

with the exact calculation. Hence, the difference between Eqs. (13,15) and the exact solution is not caused by the fact that the SA is used. Obviously the true reason must be the assumption that $H_\alpha$ is optically thin throughout the full wind from $r = 1$ to $r \to \infty$.

To investigate this in more detail we firstly disentangle the contribution of optically thick and thin layers to the equivalent width $W'_\lambda$. This is done in Fig. 3 where the full SA solution (Eqs. 4,5) is compared with a SA solution where only resonance zones with $\tau \leq 1$ are accounted for. We see that the difference is small and that about 80 % of the equivalent width arises from optically thin layers. The reason why the optically thin approach of Eqs. (13, 15) overestimates $W'_\lambda$ so badly must therefore result from the fact that the optically thin assumption is applied also in optically *thick* regions, since then the expansion of $(1 - \exp(-\tau))$ by $\tau$ inevitably leads to a dramatic overestimation of the arising equivalent width. (Simply speaking, the resulting intensities from optically thick resonance zones are too large by a factor $\tau \gg 1$ if the optically thin approximation is inconsistently applied.) Hence, instead of starting the integration at $r = 1$ in Eq. (15) we have to introduce a lower boundary $r_0 > 1$ which terminates the optically thin emitting volume at $\tau_0 = 1$. $r_0$ can be found from Eq. (1) via

$$(r_0 v(r_0))^3 \left(1 + \mu^2 \sigma(r_0)\right) = A. \tag{18}$$

For the case of $\beta = 1$, which will be used in the following as a typical value, we obtain as a solution

$$r_0^{\rm r} = b + (A/b)^{\frac{1}{2}} \; ; \qquad r_0^{\rm t} = b + (A)^{\frac{1}{3}} \, , \tag{19}$$

where $r_0^{\rm r}$, $r_0^{\rm t}$ are the values for a radial ($\mu = 1$, $p = 0$) and a tangential ($\mu = 0$, $p = r_0^{\rm t}$, $z = 0$) ray, respectively. The reader may note that because of the change of sign in $\sigma$ at $r = (1 + b)$ the $\tau_0 = 1$ surface is prolate (with respect to the observer) in the case of $A > 1$, oblate in the case $A < 1$ and a sphere for $A = 1$.

Since $b$ is always very close to unity, $r_0$ is always larger than 1.01 for $\log A > -5$ and consequently $v(r_0)$ becomes much larger and independent of the minimum velocity $v_{\rm min}$. This means that we can replace $b$ in Eq. (17) by $b = 1$ and then modify Eq. (15) by

$$\int_1^\infty \frac{\mu_*(r){\rm d}r}{r^2 v(r)^2} \quad \to \int_{r_{(\tau_0=1)}}^\infty \frac{\mu_*(r){\rm d}r}{(r-1)^2} \; =$$

$$= 2\left(\left(\frac{2}{r_{(\tau_0=1)} - 1} + 1\right)^{\frac{1}{2}} - 1\right) + \arccos\frac{1}{r_{(\tau_0=1)}} - \frac{\pi}{2} \tag{20}$$

For small values of $h =: (r_{(\tau_0=1)} - 1)$ this integral can be approximated by $\approx 2^{3/2} h^{-1/2}$, so that the equivalent width in the optically thin limit (and $\beta = 1$) is proportional to

$$W'_\lambda \sim \frac{v_\infty A}{h^{\frac{1}{2}}} \sim v_\infty A^{\frac{3}{4}} \; \ldots \; v_\infty A^{\frac{5}{6}}$$

depending which value for $r_{(\tau_0=1)}$ (cf. Eq. 19) is applied. Thus, it is now clear that the "exact" slope ${\rm d}\log(W'_\lambda)/{\rm d}\log(A) \approx 0.75 \ldots 0.80$ of the results in Fig. 2, compared to the slope of unity in Eq. (13,14,15) which has been quoted as the standard value for optically thin emission in previous papers (Leitherer 1988; Panagia 1988; Scuderi et al. 1992), stems from the increasing size of the optically thick core which is also a function of $A$.

Performing finally some numerical calculations applying either $r_0^{\rm r}$ or $r_0^{\rm t}$ to Eq. (20), it turned out that the use of $r_0^{\rm t}$ (i.e., the largest possible value) gives sufficient accuracy compared to the results of Fig. 3. Hence, the optically thin contribution to the equivalent width of $H_\alpha$ ($\approx 80$ % of the total emission) for a $\beta = 1$ velocity field can be approximated by

$$W_\lambda = 4 \, \frac{v_\infty \lambda_0}{c} \, \bar{b}_3 A(b_{2,3} \equiv 1) \times$$

$$\times \left\{ 2\left(2A^{-\frac{1}{3}} + 1\right)^{\frac{1}{2}} + \arccos\frac{1}{1 + A^{\frac{1}{3}}} - \frac{4 + \pi}{2} \right\} + W_\lambda^{\rm phot} \tag{21}$$

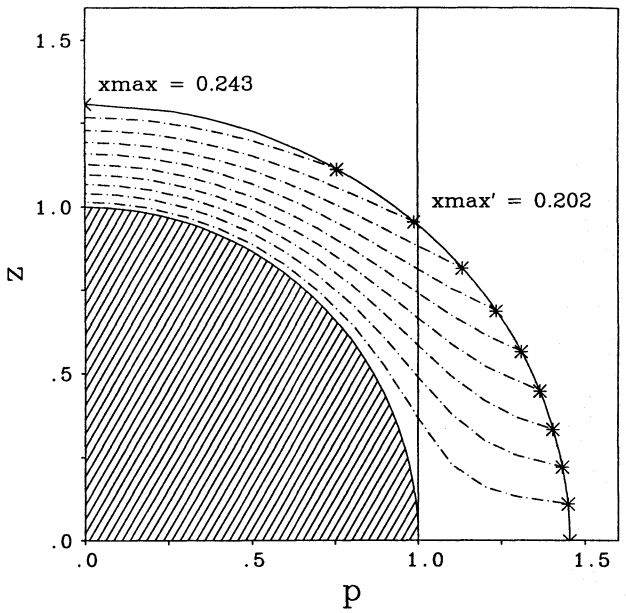


**Fig. 4.** Resonance zones (dashed-dotted) in p-z geometry for which the condition $\tau \geq \tau_0$ is fulfilled, for mass-loss parameter $A/\tau_0 = 0.1$. Each zone belongs to a different frequency $x \geq 0$. The point, where $\tau = \tau_0$ is reached the first time (from the observer's direction), is indicated by an asterisks. The envelope connecting these points is the solid curve. At $p = 0$ the point on the envelope belongs to a frequency $x_{\max}$ (= 0.243 in our example), and at $p = 1$ the corresponding value is $x'_{\max}$ (= 0.202). At $z = 0$ the frequency is $x = 0$. We call this envelope $p_{\max}(x, A/\tau_0)$ the curve of *maximum impact parameter*. (The dependency on $A/\tau_0$ will be suppressed in the following.) $\beta = 1$ and $v_{\min} = 0.01 v_\infty$ are adopted in this example.
Note: the intersection of the above envelope with the z-axis defines $r_0^{\mathrm{r}}$, whereas its intersection with the p-axis defines $r_0^{\mathrm{t}}$ (cf. Eq. 19)

**Table 1.** $W'_\lambda$ as function of $A$ in comparison to the optically thick approximation. Model parameters: *LTE*, $P_x \equiv 1$, $T_{\mathrm{e}} = T_{\mathrm{rad}}$, $v_\infty = 2{,}000$ km/s, $v_{\min} = 5$ km/s, $\beta = 1$. For discussion see text

| log($A$) | SA | SA ($\tau \geq 1$) | Eq.(32) ($\tau_0 = 1.$) | Eq.(32) ($\tau_0 = 0.228$) |
|---|---|---|---|---|
| -0.25 | 143 | 50 | 49 | 146 |
| 0.00 | 212 | 76 | 76 | 217 |
| 0.25 | 313 | 115 | 115 | 319 |
| 0.50 | 674 | 259 | 257 | 670 |
| 1.00 | 1431 | 567 | 545 | 1378 |

and is essentially independent of $v_{\min}$ ! The high accuracy of this approximation is shown in Fig. 3. Recalling that for $A \gtrsim 10^{-4}$ the SA is correct, we have therfore explained why the exact solution results in an effective slope $\mathrm{d}\log(W'_\lambda)/\mathrm{d}\log(A) \approx 0.75$ for $-4 \lesssim \log A \lesssim -0.5$.

### 2.2.2. The optically thick limit

In this section, we want to discuss the case of a wind that is mostly optically thick in $\mathrm{H}_\alpha$ . Although this does not occur in O-star winds, there are a number of reasons for also considering this case, apart from its intrinsic theoretical interest:

- As we have seen above, there is *always* a certain contribution from the optically thick core.
- While Panagia (1988) and Scuderi et al. (1992) discussed the optically thick limit, they used a different velocity structure. It is interesting to compare their results with the ones resulting from the physically more realistic $\beta$-velocity law.
- For B-type Super-/Hypergiants with large $\dot{M}$ and small $v_\infty$ (examplary P Cygni) and WR-stars with large $\dot{M}$ and small $R_*$ (here of course with respect to the He-lines) the value of $A$ can become larger than unity hence favouring a dominating contribution from optically thick processes, so that further investigations are extremely useful.

In the optically thick limit ($\exp(-\tau) \rightarrow 0$), the equivalent width of $\mathrm{H}_\alpha$ is given by (cf. Eqs. 7,8,9)

$$W_\lambda = \frac{v_\infty \lambda_0}{c} \left\{ 4 \int_0^{x'_{\max}} \mathrm{d}x \int_1^{p_{\max}(x)} \frac{S}{I_c}(z_0) p \mathrm{d}p + \right.$$
$$\left. + 2 \int_0^{x_{\max}} \mathrm{d}x \int_0^{p_x} \left( \frac{S}{I_c}(z_0) - 1 \right) p \mathrm{d}p \right\} + W^{\mathrm{red}}_{\lambda,\mathrm{phot}}. \qquad (22)$$

$x_{\max}$, $x'_{\max}$ and $p_{\max}(x)$ are defined in Fig. 4, $p_x = \mathrm{Min}(p_{\max}, 1)$ and $z_0$ is the location of the resonance zone as function of $(x, p)$ between $p = 0$ and $p_{\max}$ or $p_x$, respectively.

With the approximation $S \equiv I_c$, the solution of this problem

$$W_\lambda = 4 \frac{v_\infty \lambda_0}{c} \int_0^{x'_{\max}} \mathrm{d}x \int_1^{p_{\max}(x)} p \mathrm{d}p + W^{\mathrm{red}}_{\lambda,\mathrm{phot}} =$$
$$= 2 \frac{v_\infty \lambda_0}{c} \int_0^{x'_{\max}} \left( p^2_{\max}(x) - 1 \right) \mathrm{d}x + W^{\mathrm{red}}_{\lambda,\mathrm{phot}} \qquad (23)$$

reduces to the calculation of $x'_{\max}$ and $p_{\max}(x)$. In order to keep the problem analytically feasible, we will restrict ourselves again to the case $\beta = 1$ and $b = 1$, where the latter assumption is of no importance as for sufficiently large $A$ the optically thick core is always large enough to ensure the solution to be independent on $v_{\min}$.

Under these conditions, we can calculate $p_{\max}(x)$. Combining Eq. (1) with the resonance condition Eq. (6), we obtain

$$h_0^3 + x^2 (h_0 + 1)^2 (1 - h_0) = A/\tau_0 \qquad (24)$$
$$h_0 = r_0 - 1\,, \qquad (25)$$

which yields the radius where a certain value of $\tau_0$ is reached *on the considered resonance zone*. Assuming that we know the solution of this cubic equation $r_0(x)$ and hence $v(r_0(x))$, $p_{\max}(x)$ follows from

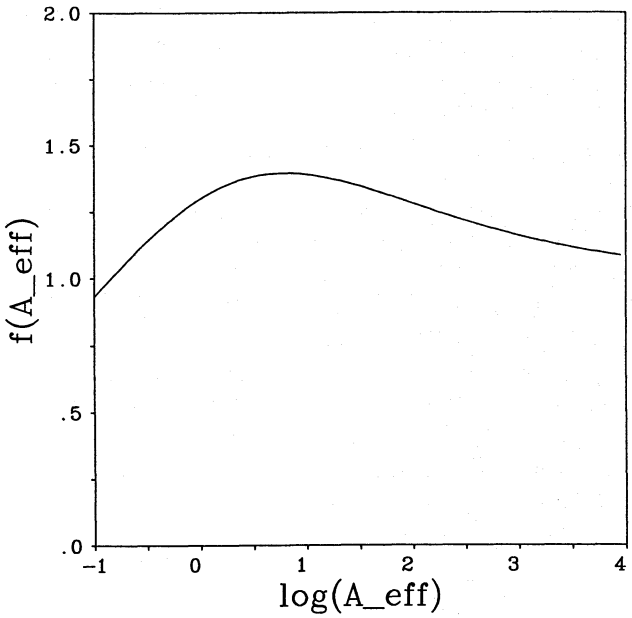


**Fig. 5.** $f(A_{\rm eff})$ (cf. Eq. 35) for $\log A_{\rm eff} = -1...4$

$$p^2_{\rm max}(x) = r_0^2(x)\left(1 - \left(\frac{x}{v(r_0(x))}\right)^2\right) \tag{26}$$

$$p^2_{\rm max}(0) = r_0^{\rm t\,2} \tag{27}$$

$$p^2_{\rm max}(x_{\rm max}) = 0 \tag{28}$$

$$x_{\rm max} = v(r_0^{\rm r}) \tag{29}$$

where $r_0^{\rm r}$, $r_0^{\rm t}$ are defined in analogy to Eq. (19) with $A$ replaced by $A/\tau_0$. As demonstrated by Table 2, an excellent approximation of Eq. (26) is

$$p^2_{\rm max}(x) \approx r_0^{\rm t\,2}\left(1 - \left(\frac{x}{x_{\rm max}}\right)^2\right), \tag{30}$$

which avoids the solution of the cubic equation (24). (Note that Eq. (30) is exact for $A/\tau_0 = 1$). The value of $x'_{\rm max}$ (to calculate $W_\lambda$ in Eq. (23) we need $p_{\rm max}$ only in the range from 0 to $x'_{\rm max}$) is then given by

$$p(x'_{\rm max}) = 1 \quad \rightarrow \quad x'_{\rm max} = x_{\rm max}\left(1 - \frac{1}{r_0^{\rm t\,2}}\right)^{\frac{1}{2}} \quad \rightarrow$$

$$x'_{\rm max} = \frac{\left(r_0^{\rm t\,2} - 1\right)^{\frac{1}{2}}}{r_0^{\rm t} r_0^{\rm r}}(A/\tau_0)^{\frac{1}{2}} \tag{31}$$

Combining now Eq. (23) and (31) we obtain for the contribution of the optically thick core

$$W_\lambda = \frac{4}{3}\frac{v_\infty \lambda_0}{c}\frac{\left(r_0^{\rm t\,2} - 1\right)^{\frac{3}{2}}}{r_0^{\rm t} r_0^{\rm r}}(A/\tau_0)^{\frac{1}{2}} + W^{\rm red}_{\lambda,\rm phot} \tag{32}$$

The accuracy of this approximation is investigated in Table 1, where we compare (for the same model as above) the resulting equivalent width $W''_\lambda = W_\lambda + |W^{\rm red}_{\lambda,\rm phot}|$ in dependence of $A$. Column 3 gives the values from the "exact" SA-calculation however taking only into account the contribution from optical depths $\tau \geq 1$, and column 4 the results from Eq. (32) with $\tau_0 = 1$. The results are essentially identical, and only for values $A \gtrsim 10$ the difference becomes significant as the approximation for $p^2_{\rm max}$ begins to become less accurate. However, comparing with the *total* SA equivalent width given in column 2, it is obvious that the contribution of the region with $\tau \geq 1$ is roughly an (almost constant!) factor of 3 too small.

The reason for this discrepancy is the fact that for spherical geometry, an opacity proportional to $\rho^2$ and $v(r) \approx v_\infty$ the "effective" optical depth for contributing to the observed flux is significantly smaller than unity, namely

$$\tau_{\rm eff} = 0.228. \tag{33}$$

This was found by Panagia & Felli (1975), Wright & Barlow (1975) and Lamers & Waters (1984) when treating the problem of thermal radio emission in stellar winds. Indeed, if using $\tau_0 = \tau_{\rm eff}$ in Eq. (32) we achieve almost perfect agreement with the SA solution, as can be seen from the last column in Table 1.

Finally, we investigate the slope $\mathrm{d}\log(W''_\lambda)/\mathrm{d}\log(A)$ for large values of $A \gtrsim 1$. With the definitions for $r_0^{\rm r}$, $r_0^{\rm t}$ and denoting $A_{\rm eff} = A/\tau_{\rm eff}$ Eq. (32) can be rewritten as

$$W''_\lambda(A) = \frac{4}{3}\frac{v_\infty \lambda_0}{c} f(A_{\rm eff}) A_{\rm eff}^{\frac{2}{3}} \tag{34}$$

$$f(A_{\rm eff}) = \frac{\left(2 + A_{\rm eff}^{\frac{1}{3}}\right)^{\frac{3}{2}} A_{\rm eff}^{\frac{1}{3}}}{\left(1 + A_{\rm eff}^{\frac{1}{3}}\right)\left(1 + A_{\rm eff}^{\frac{1}{2}}\right)} \tag{35}$$

where the function $f(A_{\rm eff})$ is an only mildly varying function in the range $A_{\rm eff} = 0.1...\infty$ (cf. Fig. 5) with

$$\begin{aligned} f(1) &= \tfrac{3^{\frac{3}{2}}}{4} = 1.30 \\ f(A_{\rm eff})|_{\rm max} &= 1.39 \quad \text{for} \quad A_{\rm eff} = 6.23 \\ f(A_{\rm eff} \rightarrow \infty) &\rightarrow 1 \\ < f > &= 1.32 \quad \text{for} \quad A_{\rm eff} \in [1, 100] \end{aligned} \tag{36}$$

In the optically thick limit, the equivalent width of $\mathrm{H}_\alpha$ is therefore proportional to

$$W''_\lambda \sim v_\infty A^{\frac{2}{3}}. \tag{37}$$

### 2.2.3. Resulting scaling relations – comparison to previous results

Summarizing the results of the two preceeding paragraphs, we find the following scaling relations for the equivalent width of $\mathrm{H}_\alpha$ (assuming a $\beta = 1$ velocity field as the average representative for typical O-star winds with $\beta = 0.7...1.3$). We have for $10^{-4} \lesssim A \lesssim 10^{-1}$:

$$\log(W'_\lambda) \approx 3/4\log(A) + \log(v_\infty) + \log(\bar{b}_3) + 2.09 \tag{38}$$

**Table 2.** Exact (Eq. 24,26) and approximated values (Eq. 30) for $p^2_{max}$ as function of $x$ in the range from $x = x'_{max}...0$ for $A/\tau_0 = 0.1,\ 1.0,\ 10$ (calculated with $b = 0.99$)

| $A/\tau_0 = 0.1$ $r_0^r = 1.31,\ r_0^t = 1.45$ | | | $A/\tau_0 = 1.0$ $r_0^r = 1.99,\ r_0^t = 1.99$ | | | $A/\tau_0 = 10.$ $r_0^r = 4.17,\ r_0^t = 3.14$ | | |
|---|---|---|---|---|---|---|---|---|
| $x$ | $p^2_{max}$(ex) | $p^2_{max}$(appr) | $x$ | $p^2_{max}$(ex) | $p^2_{max}$(appr) | $x$ | $p^2_{max}$(ex) | $p^2_{max}$(appr) |
| .176 | 1.211 | 1.000 | .436 | 1.000 | 1.000 | .723 | 1.121 | 1.000 |
| .159 | 1.403 | 1.212 | .392 | 1.562 | 1.562 | .651 | 2.910 | 2.689 |
| .141 | 1.565 | 1.401 | .348 | 2.066 | 2.066 | .578 | 4.438 | 4.199 |
| .124 | 1.701 | 1.568 | .305 | 2.510 | 2.510 | .506 | 5.750 | 5.533 |
| .106 | 1.815 | 1.713 | .261 | 2.894 | 2.894 | .434 | 6.866 | 6.688 |
| .088 | 1.909 | 1.836 | .218 | 3.220 | 3.220 | .361 | 7.798 | 7.666 |
| .071 | 1.984 | 1.936 | .174 | 3.486 | 3.486 | .289 | 8.555 | 8.465 |
| .053 | 2.042 | 2.014 | .131 | 3.694 | 3.694 | .217 | 9.139 | 9.088 |
| .035 | 2.082 | 2.070 | .087 | 3.842 | 3.843 | .145 | 9.556 | 9.532 |
| .018 | 2.107 | 2.103 | .044 | 3.930 | 3.930 | .072 | 9.805 | 9.799 |
| .000 | 2.115 | 2.115 | .000 | 3.960 | 3.960 | .000 | 9.887 | 9.887 |

and for $A \gtrsim 1$:

$$\log(W''_\lambda) \approx 2/3 \log(A) + \log(v_\infty) + 2.014\,, \tag{39}$$

where $v_\infty$ again is calculated in units of 1,000 km/s and $S/I_c$ approximated by unity in the optically thick case. The equivalent width for $A$ in the intermediate range $0.1 < A < 1$ has to be evaluated with the complete expression Eq. (21), taking into account that this gives only $\approx 80$ % of the total value. Hence, for fixed $v_\infty$, the slope of $\mathrm{d}\log(W''^{(\prime)}_\lambda)/\mathrm{d}\log(A)$ *should lie in the range between 3/4...2/3*. With respect to a variation in $v_\infty$, the above equations imply that the corrected equivalent width should either scale with

$$\log(W'_\lambda) \approx \frac{3}{4}\log\left(\frac{\dot{M}^2}{{R_*}^3 {v_\infty}^{5/3}}\right) + \mathrm{const}(T_\mathrm{e}, b_3, Y) \tag{40}$$

for $10^{-4} \lesssim A \lesssim 10^{-1}$ or with

$$\log(W''_\lambda) \approx \frac{2}{3}\log\left(\frac{\dot{M}^2}{{R_*}^3 {v_\infty}^{3/2}}\right) + \mathrm{const}(T_\mathrm{e}, Y) \tag{41}$$

for $A \gtrsim 1$. The precision of these predictions can be checked by comparison with our final results which include the influence of different $\beta$'s, consistent departure coefficients and the He II blend as discussed in Sects. 2.3 to 2.5.

Inverting the above scaling laws, the mass-loss rate derived by $H_\alpha$ is dependent on the following combination of stellar and wind parameters

$$\dot{M}(\mathrm{thin}) \sim {W'_\lambda}^{\frac{2}{3}} {R_*}^{\frac{3}{2}} {v_\infty}^{\frac{5}{6}} \tag{42}$$

$$\dot{M}(\mathrm{thick}) \sim {W''_\lambda}^{\frac{3}{4}} {R_*}^{\frac{3}{2}} {v_\infty}^{\frac{3}{4}}\,, \tag{43}$$

which has to be contrasted to the results by Leitherer (1988; optically thin limit) and Panagia (1988)/Scuderi et al. (1992) (optically thin *and* thick limit)

$$\dot{M}(\mathrm{thin}) \sim {W'_\lambda}^{\frac{1}{2}} {R_*}^{\frac{3}{2}} v_\infty$$

$$\dot{M}(\mathrm{thick}) \sim W'_\lambda {R_*}^{\frac{3}{2}} {v_\infty}^{\frac{1}{2}}.$$

The obvious differences are due to the neglect of the increase in radius of the optically thick core in the optically thin limit and because of the different shape of the velocity field in Panagia's derivation.

Finally, it should be stressed that the influence of the assumed minimum velocity $v_{min}$ is clearly not so important as it would be if the purely optically thin approximation were used.

### 2.3. *Approximate solution of the complete problem and comparison with unified model atmospheres*

As the observable $H_\alpha$ feature actually consists of two components, $H_\alpha$ itself and the $\mathrm{HeII}_{4\leftrightarrow 6}$ blend ($\lambda$ 6560.25 corresponding to $\Delta v = 120$ km/s), one has to investigate how far this blend is of importance for a *quantitative* mass-loss determination.

In view of the similar ionization energies ($E_{4,6}$ (HeII) = 27450.1, 12219.9 cm$^{-1}$ compared to $E_{2,3}$ (H) = 27419.7, 12186.5 cm$^{-1}$) and $gf$-values ($gf_{He} = 5.7376$, $gf_H = 5.1256$) of the two transitions, the ratio of the resulting line opacities is roughly given by

$$\chi_{He}/\chi_H \approx Y b_4(\mathrm{HeII})/b_2(\mathrm{H}) \tag{44}$$

(cf. Eq. 3), which is (solar composition provided) of order 0.1 in the sonic region, but may reach ($b_4$(HeII) $\rightarrow$ O(10), see below) values of order unity in the outer wind part. Hence, in contrast to previous assumptions (cf. Leitherer 1988; Drew 1990), the He-blend can influence both the shape and the equivalent width of the combined profile significantly, especially in denser winds when the effective radius becomes large. This was firstly demonstrated by A. Gabler et al. (1990), who showed that for $\dot{M}$ in the range of $1...10 \cdot 10^{-6} M_\odot$/yr the typical error in the

**Table 3.** Model grid of unified atmospheres for O-type stars used to derive the radial stratification of Hydrogen/Helium departure coefficients and to check our approximate treatment of $H_\alpha$ line formation. $Y = 0.1$, $\dot{M}$ in $10^{-6}M_\odot$/yr, $v_\infty$ in km/s, $A$ (cf. Eq. 3) calculated with $T_e = 0.75T_{\rm eff}$ and $b_{2,3} \equiv 1$. The last column gives the total equivalent width of the $H_\alpha$ complex in Å

| $T_{\rm eff}$ | log $g$ | $R_*$ | $\dot{M}$ | $v_\infty$ | log $A$ | $W_\lambda$ |
|---|---|---|---|---|---|---|
| 41000. | 3.50 | 14.0 | 1.460 | 1055. | -2.17 | 0.71 |
| 41000. | 3.50 | 14.0 | 1.740 | 1720. | -2.65 | -0.27 |
| 41000. | 3.70 | 14.0 | .149 | 1716. | -4.78 | -2.80 |
| 41000. | 3.70 | 14.0 | .622 | 1740. | -3.56 | -2.39 |
| 41000. | 3.70 | 14.0 | 1.010 | 2900. | -3.80 | -2.36 |
| 41000. | 3.70 | 14.0 | 1.664 | 2070. | -2.93 | -0.92 |
| 41000. | 3.70 | 14.0 | 2.590 | 1745. | -2.33 | 1.48 |
| 42000. | 3.60 | 24.6 | 3.010 | 2650. | -3.51 | -1.88 |
| 42500. | 3.70 | 14.0 | 1.350 | 2100. | -3.19 | -1.51 |
| 42500. | 3.70 | 14.0 | 1.717 | 2100. | -2.98 | -0.96 |
| 42500. | 3.70 | 14.0 | 2.050 | 2105. | -2.83 | -0.41 |
| 42500. | 3.80 | 14.0 | 1.702 | 2066. | -2.97 | -1.03 |
| 43500. | 3.60 | 22.9 | 2.901 | 2650. | -3.50 | -1.71 |
| 43500. | 3.80 | 13.4 | 1.550 | 2160. | -3.08 | -1.38 |
| 43500. | 3.80 | 13.4 | 1.000 | 2160. | -3.46 | -2.19 |
| 44000. | 3.80 | 10.0 | .093 | 1270. | -4.47 | -2.88 |
| 44000. | 3.80 | 10.0 | .554 | 1276. | -2.92 | -1.75 |
| 44000. | 3.80 | 10.0 | 2.700 | 1265. | -1.54 | 8.00 |
| 45000. | 4.00 | 12.3 | .204 | 2043. | -4.71 | -3.10 |
| 47500. | 3.70 | 17.9 | 11.140 | 2250. | -1.93 | 6.70 |
| 47500. | 3.70 | 17.9 | 13.150 | 2250. | -1.78 | 11.97 |
| 47500. | 3.90 | 17.9 | 11.110 | 2260. | -1.93 | 7.73 |
| 47500. | 4.00 | 8.2 | 1.015 | 2600. | -3.18 | -1.56 |
| 47500. | 4.00 | 8.2 | 1.990 | 2640. | -2.61 | .88 |
| 47500. | 4.00 | 8.2 | 2.920 | 2640. | -2.28 | 3.49 |
| 48000. | 4.00 | 10.7 | .304 | 2160. | -4.35 | -2.91 |
| 50000. | 3.90 | 19.0 | 11.220 | 1900. | -1.85 | 6.40 |
| 50000. | 3.90 | 19.0 | 13.120 | 1910. | -1.72 | 8.35 |
| 50000. | 4.20 | 14.4 | .550 | 3200. | -4.79 | -3.26 |
| 55000. | 4.07 | 22.0 | 9.410 | 3205. | -3.01 | -0.40 |

equivalent width induced by neglecting this blend is of the order 1 to 2 Å *below* the correct value , i.e., a significant fraction of the total equivalent width. (Note, that L&L accounted for this blend, however only in an approximate way.)

### 2.3.1. Radial stratification of departure coefficients

In order to obtain a simple expression for the departure coefficients without solving each time the complete *NLTE* wind problem, we proceed in the following way: From the analysis of the stratification of occupation numbers for a model grid of *unified atmospheres* of O-type stars (cf. Table 3), it turned out that the $b_i$'s can be simply parametrized as function of velocity. Thus for hydrogen (i = 2,3,4,5) we have

$$0. \le v < 0.01 \;:\; b_2(r) = 1. + \left(\frac{b_2^{\rm in} - 1.}{0.01}\right) v(r) \qquad (45)$$

$$0. \le v < 0.01 \;:\; b_i(r) = .9 + \left(\frac{b_i^{\rm in} - .9}{0.01}\right) v(r),\ {\rm i} \ne 2$$

$$0.01 \le v < 0.1 \;:\; b_i(r) = b_i^{\rm in} + \left(\frac{b_i^{\rm min} - b_i^{\rm in}}{0.09}\right) (v(r) - 0.01)$$

$$0.1 \le v < 1.0 \;:\; b_i(r) = b_i^{\rm min} + \left(\frac{b_i^{\infty} - b_i^{\rm min}}{0.9}\right) (v(r) - 0.1)$$

and for helium (i = 4,6,8,10)

$$0. \le v < 0.1 \;:\; b_4(r) = 1. + \left(\frac{b_4^{\rm in} - 1.}{0.1}\right) v(r) \qquad (46)$$

$$0. \le v < 0.1 \;:\; b_i(r) = .9 + \left(\frac{b_i^{\rm in} - .9}{0.1}\right) v(r),\ {\rm i} \ne 4$$

$$0.1 \le v < 0.55 \;:\; b_i(r) = b_i^{\rm in} + \frac{1}{3}\left(\frac{b_i^{\rm in} - b_i^{\infty}}{0.45}\right) (0.1 - v(r))$$

$$0.55 \le v < 1.0 \;:\; b_i(r) = b_i^{\infty} + \frac{2}{3}\left(\frac{b_i^{\rm in} - b_i^{\infty}}{0.45}\right) (1.0 - v(r)).$$

$b_i^{\rm in}$ and $b_i^{\infty}$ are here the departure coefficients at $v = 0.01$ for Hydrogen ($v = 0.1$ for HeII, respectively) and at the outer boundary, which have to be specified for all contributing levels (see Tables 4 and 5). Note, that the boundary values of the HeII departure coefficients depend on the quantity $D = \dot{M}/(R_* v_\infty)^{1.5} \sim A^{\frac{1}{2}}$. The special appearance of the value $b_i^{\rm min} \ne b_i^{\infty}$ for the *i=2 level of H* (cf. Tab. 4) accounts for the fact that the corresponding departure coefficient exhibits a certain minimum at a typical velocity $v \approx 0.1$.

It must be stressed, that both Eqs. (45,46) in combination with the values given in Tables 4 and 5 where derived by a *recalibration* of the original departure coefficients (valid for the specific temperature stratification of the unified atmospheres) *to a constant electron temperature of* $T_e = 0.75T_{\rm eff}$, which is an average representative value in the line forming region of the models. The above approximation represents the typical run of the "exact" departure coefficients with an accuracy of 20 % and in so far incorporates the major effects arising from "unified atmospheres", which comprise a correct treatment of line formation in the *transsonic* region and a consistent continuum (cf. also de Koter et al. 1993 and Schaerer & Schmutz 1994), contrasted to the results of a pure photospheric or pure wind calculation. Figures 6 and 7 give an impression of the accuracy of our parametrization by comparing the approximated to the exact departure coefficients. The reader may note that the departure coefficients influence the determination of the mass-loss rate only by a power of 0.5, so that any errors and uncertainties have an only small effect.

### 2.3.2. Comparison with unified atmosphere profiles

With the above stratification of the departure coefficients, we are now able to calculate the emergent profile of the $H_\alpha$ complex. This is done by solving the formal integral for the two overlapping components in the observer's frame, taking into account the finite and different thermal velocities of the hydrogen

**Table 4.** Boundary values for Hydrogen departure coefficients $b_i$ (i = 2,3,4,5) to be used for the parametrization Eq. (45) and $T_e = 0.75T_{\rm eff}$

| i | $b_i^{\rm in}$ $v = 0.01$ | $b_i^{\rm min}$ $v = 0.1$ | $b_i^{\infty}$ $v = 1.0$ |
|---|---|---|---|
| 2 | 1.5 | 1.2 | 1.3 |
| 3 | 1.2 | 1.1 | 1.1 |
| 4 | 1.1 | 1.0 | 1.0 |
| 5 | 1.0 | 0.9 | 0.9 |

**Table 5.** Boundary values for HeII departure coefficients $b_i$ (i = 4,6,8,10) in dependence of $D = \dot{M}/(R_* v_\infty)^{1.5}$ ($\dot{M}$ in $10^{-6}$ $M_\odot$/yr, $R_*$ in $R_\odot$ and $v_\infty$ in km/s) to be used for the parametrization Eq. (46) and $T_e = 0.75T_{\rm eff}$

| $b_i^{\rm in}$ | $\log D \le -7.3$ | $-7.3 < \log D \le -6.3$ | $\log D > -6.3$ |
|---|---|---|---|
| i = 4 | 3.0 | $-9.05 - 1.65\log D$ | 1.35 |
| 6 | 3.5 | $-12.56 - 2.2\log D$ | 1.3 |
| 8 | 3.5 | $-12.56 - 2.2\log D$ | 1.3 |
| 10 | 2.2 | $-6.56 - 1.2\log D$ | 1.0 |
| $b_i^{\infty}$ | $\log D \le -6.9$ | $-6.9 < \log D \le -5.8$ | $\log D > -5.8$ |
| i = 4 | 20.6 | $-76.0 - 14\log D$ | 5.2 |
| 6 | 25.4 | $-71.2 - 14\log D$ | 10. |
| 8 | 25.4 | $-71.2 - 14\log D$ | 10. |
| 10 | 20.2 | $-62.6 - 12\log D$ | 7.0 |

and helium ions. (This turns out to be of considerable importance especially for thin winds with a small effective radius.) For this calculation, we need the following input quantities (cf. Eqs. 3-5):

- the stellar radius $R_*$,
- the parameters describing the velocity field, namely $v_\infty$, $v_{\rm min}$ and $\beta$,
- the rotational speed $v \sin i$,
- the photospheric profile and the corresponding radiation temperature at the neighbouring continuum $T_{\rm rad}$,
- the helium abundance $Y$,
- the boundary values of the departure coefficients for the i = 2,3 (H) and i=4,6 (HeII) level, cf. Tables 4 and 5 (calibrated to an electron temperature $T_e = 0.75T_{\rm eff}$!)
- *and the mass-loss rate* $\dot{M}$.

In the application to observed stellar line profiles, the values of $R_*$, $v \sin i$, $Y$ and the photospheric profile (dependent on $T_{\rm eff}$ and $\log g$) result from a *NLTE* analysis of the relevant star by means of hydrostatic, plane-parallel model atmospheres, modified to include the effects of winds on $H_\gamma$ for the $\log g$ determination (cf. Sect. 3.1.2). The terminal velocity is determined from UV P-Cygni profiles (see Sect. 3.1.4), and $\dot{M}$ and $\beta$ are fit-parameters to be determined from the $H_\alpha$ profile itself.

The only quantities left to be specified are the values for $v_{\rm min}$ and $T_{\rm rad}$, for which we will use

$$v_{\rm min} = 1\,{\rm km/s}$$

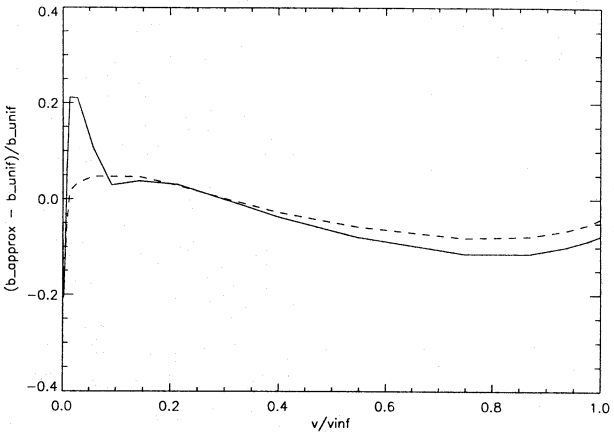


**Fig. 6.** Relative error (compared with the results of unified model atmospheres) of approximated departure coefficients for the i=2 (fully-drawn) and i=3 (dashed) level of hydrogen and an atmospheric model with parameters $T_{\rm eff} = 43,500K$, $\log g = 3.8$, $R_* = 13.4R_\odot$, $\dot{M} = 1.55 \cdot 10^{-6} M_\odot/{\rm yr}$ and $v_\infty = 2160$ km/s

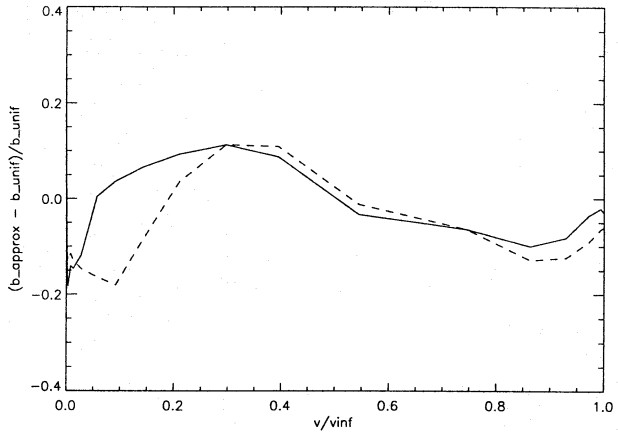


**Fig. 7.** As Fig. 6, but for the HeII(i=4,6) levels

$$T_{\rm rad} = 0.77\,T_{\rm eff},$$

where the latter represents an average value resulting from our grid of unified atmospheres (Table 3).

The choice of the rather low minimum velocity (in comparison to the speed of sound) was triggered by the following arguments: Although the profiles are almost independent of this parameter for values of $\log A \gtrsim -4$, the "exact solution" depends on $v_{\rm min}$ for the smallest wind densities. This behaviour follows from the fact that the "exact" solution takes into account the finite width of the profile. If the "effective" radius lies now in or even below the sonic region, the results *must* depend on the density stratification there and on the choice of the lower boundary, in particular for those cases, where the accumulated optical depth inside the corresponding resonance zones is not too large (cf. Sellmaier et al. 1993).)

By comparing our approximate treatment to the unified atmosphere profiles, it then turned out that the best agreement both

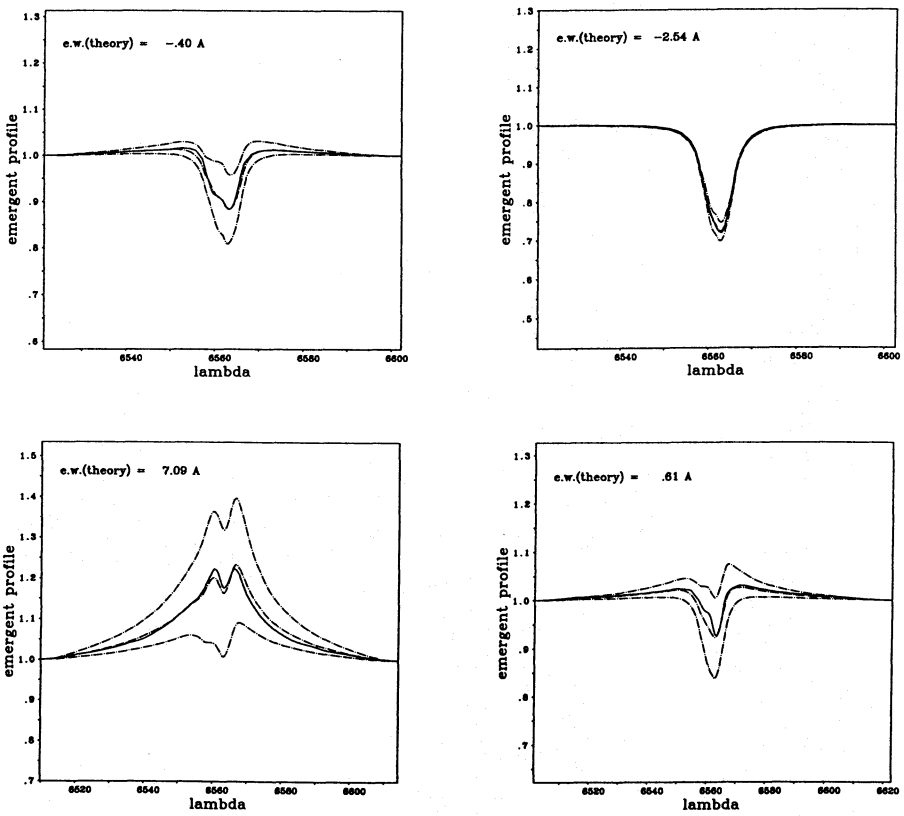


**Fig. 8.** Comparison of approximate (dashed-dotted) to unified atmosphere $H_\alpha$ profiles (solid) for four exemplary models of Table 6. Also shown are the profiles for a mass-loss rate being 30 % larger and smaller. $V \sin i$ arbitrarily set to 100 km/s. Upper left: $T_{\rm eff} = 41.0$ kK, $\log g = 3.5$, $\dot{M} = 1.74 \cdot 10^{-6} M_\odot$/yr; upper right: $T_{\rm eff} = 41.0$ kK, $\log g = 3.7$, $\dot{M} = 0.62 \cdot 10^{-6} M_\odot$/yr; lower left: $T_{\rm eff} = 47.5$ kK, $\log g = 3.7$, $\dot{M} = 11.1 \cdot 10^{-6} M_\odot$/yr; lower right: $T_{\rm eff} = 47.5$ kK, $\log g = 4.0$, $\dot{M} = 1.99 \cdot 10^{-6} M_\odot$/yr. The He blend is included in all calculations

**Table 6.** $H_\alpha$ equivalent width (in Å) of our approximate treatment in comparison to the results of unified model atmospheres for the models of Table 4 with $T_{\rm eff} = 41{,}000$ K and 47,500 K ($Y = 0.1$, $T_{\rm eff}$ in kK, $\dot{M}$ in $10^{-6} M_\odot$/yr

| $T_{\rm eff}$ | $\log g$ | $R_*$ | $\dot{M}$ | e.w.(unif.) | e.w.(appr.) | $\beta$ |
|---|---|---|---|---|---|---|
| 41.0 | 3.5 | 14.0 | 1.460 | 0.71 | 0.73 | .73 |
| 41.0 | 3.5 | 14.0 | 1.740 | -0.27 | -0.40 | .77 |
| 41.0 | 3.7 | 14.0 | .149 | -2.80 | -2.91 | 1.0 |
| 41.0 | 3.7 | 14.0 | .622 | -2.39 | -2.54 | .75 |
| 41.0 | 3.7 | 14.0 | 1.010 | -2.36 | -2.43 | .80 |
| 41.0 | 3.7 | 14.0 | 1.664 | -0.92 | -1.07 | .80 |
| 41.0 | 3.7 | 14.0 | 2.590 | 1.48 | 1.55 | .80 |
| 47.5 | 3.7 | 17.9 | 11.140 | 6.70 | 7.09 | .75 |
| 47.5 | 3.7 | 17.9 | 13.150 | 11.87 | 10.05 | .75 |
| 47.5 | 3.9 | 17.9 | 11.110 | 7.73 | 7.35 | .80 |
| 47.5 | 4.0 | 8.2 | 1.015 | -1.56 | -1.77 | .85 |
| 47.5 | 4.0 | 8.2 | 1.990 | 0.88 | 0.61 | .82 |
| 47.5 | 4.0 | 8.2 | 2.920 | 3.49 | 3.42 | .80 |

in the resulting equivalent width and profile shape is obtained for the above value of $v_{\rm min} = 1$ km/s.

In Table 6 and Fig. 8 we compare equivalent widths and line profiles calculated with the "exact" unified model atmospheres and the approximate approach. The good agreement is striking. In Fig. 8 we also indicate profiles arising from a mass-loss rate being 30 % larger and smaller than the actual one, which immediately show that in most cases (when the refilling of the photospheric profile becomes significant, i.e., $W'_\lambda \gtrsim 0.2$ Å) $\dot{M}$ can be derived with a high precision.

To obtain the line profiles and equivalent widths of our approximate approach in Fig. 8 and Table 6 we had to adjust the value of $\beta$ for the velocity field. This was done iteratively by comparing with the line profile of the unified model until the best fit was achieved. The corresponding $\beta$-values are also given in Table 6. For all models, except the ones with the weakest wind, fit values between 0.75 and 0.85 were obtained, in every case in accordance with the hydrodynamical structure of the unified model to which the approximate profiles were fitted. The case with $\beta = 1$ is a model where the wind contributes to $H_\alpha$ only through its subsonic part. The somewhat larger value of $\beta$ corresponds to the smaller wind acceleration in these layers.

We conclude that the method of deriving $\dot{M}$ and $\beta$ from $H_\alpha$-profiles by our approximate method does indeed work.

### 2.4. *The influence of different parameters on the equivalent width of $H_\alpha$*

In this section, we use our approximate approach to investigate the dependence of the $H_\alpha$ equivalent width on velocity field ($\beta$ and $v_\infty$) and temperature ($T_{\rm eff}$). We will also study the influence of the HeII blend.

From Sect. 2.2 it is obvious that the strength of the stellar wind contribution is basically a function of

$$Q = \frac{\dot{M}/(10^{-6} M_\odot/{\rm yr})}{\left(R_*/(R_\odot)\right)^{3/2}}. \qquad (47)$$

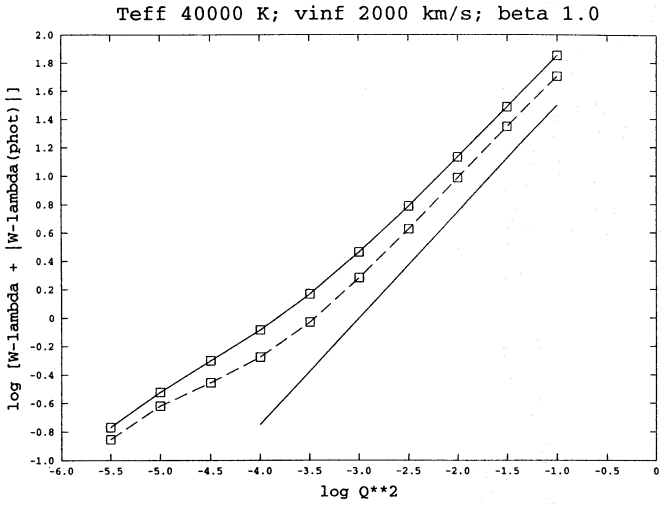


**Fig. 9.** Influence of the HeII blend on the equivalent width of $H_\alpha$. Dashed: Hydrogen line only ("exact" treatment); fully drawn: $H_\alpha$ complex including He blend. For comparison, the lower line shows a slope of 0.75 to be expected from the scaling relation for the optically thin case (Sect. 2.2.1). $T_{\rm eff}$ = 40,000 K, $v_\infty$ = 2,000 km/s and $\beta$ = 1 were adopted. Note that the photospheric equivalent width is -2.96 Å for pure hydrogen and -3.96 Å when HeII is included

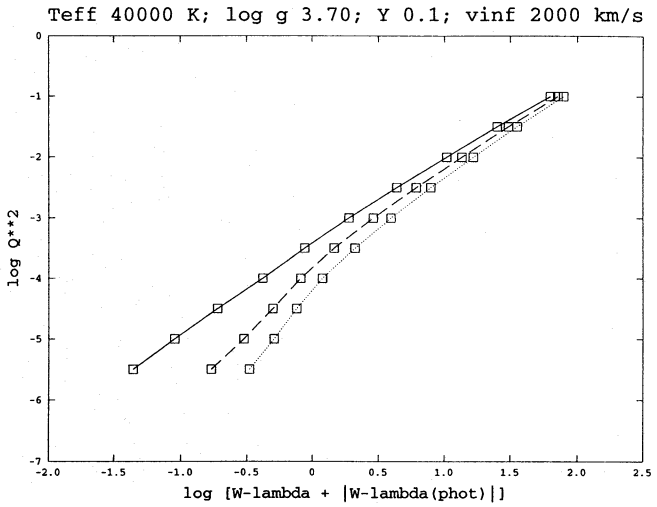


**Fig. 10.** Influence of $\beta$ on the equivalent width of $H_\alpha$ . Fully drawn: $\beta$ = 0.7; dashed: $\beta$ = 1.0; dotted: $\beta$ = 1.3. $T_{\rm eff}$ = 40,000 K, $v_\infty$ = 2,000 km/s were adopted, and the HeII blend is included

We will therefore present "curves of growth" showing the relation between equivalent width $W'_\lambda = W^{\rm obs}_\lambda + |W^{\rm phot}_\lambda|$ and $Q$ for the individual cases. Throughout this section, $\log g$ = 3.7 will be adopted for the photospheric input profiles (this has almost no influence on the *wind contribution* $W'_\lambda$) and a normal helium abundance $Y$ = 0.1 will be assumed.

### 2.4.1. Influence of the HeII blend

Figure 9 illustrates the influence of the HeII blend on the total equivalent width of $H_\alpha$ . Neglecting the blend leads to an almost parallel shift of the curve of growth resulting in an overestimate of $\dot{M}$ by a factor of 1.3 to 1.7. We note that for $-3.5 \lesssim \log Q^2 \lesssim -1$ the slope of the relation closely follows the analytical prediction of the optically thin case *even when the HeII blend is included.*

### 2.4.2. Influence of $\beta$

Figure 10 shows the influence of the steepness of the velocity law on the resulting curve of growth. We selected $\beta$ = 0.7, 1.0 and 1.3, with $\beta$ = 0.7 and 1.3 as limiting values found from the observations. Contrary to Fig. 9, here and in the following paragraphs we display the curve of growth as functional relation $\log(Q^2) = f(\log(W'_\lambda))$. In this way, the influence on $\dot{M}$ when determined from the measured equivalent width can be seen immediately!

As was already discussed in Sect. 2.2, for large values of $A$ (or $Q$) the curves converge since the optically thick core becomes so extended that almost only wind layers with $v \approx v_\infty$ contribute and $\beta$ is no longer of importance.

On the other hand, for typical O-star values ($\log W'_\lambda < 1.0$), the influence of $\beta$ is decisive and turns out to be the most crucial parameter in determining the mass-loss rates. Typical errors in $\dot{M}$ by a factor of 1.5 larger and smaller are possible if the actual velocity law has an exponent of $\beta$ = 0.7 or 1.3 instead of an assumed exponent of $\beta$ =1. For the lowest wind densities this error can even reach a factor of 2.8 for the steepest gradient. Fortunately, the influence of this parameter on the profile *shape* is in most cases so large that it can be determined in parallel with $\dot{M}$ if a detailed profile fit is performed. For the smallest wind densities, however, when the contribution of the wind is marginal, one has to rely on theoretical predictions. Examples are given in Sect. 3.2, and we want to recapitulate here only the well known result that the larger the exponent (i.e., the flatter the velocity law in the inner wind part), the narrower but also higher is the central part of the resulting emission component.

### 2.4.3. Influence of effective temperature

Figure 11 shows the curves of growth for models with different $T_{\rm eff}$. Evidently, all curves are almost parallel to each other. Exploiting the fact that the major part of the equivalent width stems from optically thin emission, the influence of the electron/radiation temperature on $W'_\lambda$ is caused mostly by changes of $\bar{b}_3$ $A(b_3 \equiv 1)$, as discussed at the beginning of Sect. 2.2.1.

Hence, taking into account the almost identical dependence of $A$(H) (and $A$(He)) on $T_{\rm e}$ for $b_i \equiv 1$, our models should yield the same value of $W'_\lambda$ for *any* combination of parameters leading to identical values of $\bar{b}_i$ $A(b_i \equiv 1)$. In addition, the dependence of $b_6$(He) on $Q$ is small and the influence of the HeII blend on the pure hydrogen case results only in a parallel-shift of the curve of growth for the entire $Q$-range of interest (cf. Fig. 9).

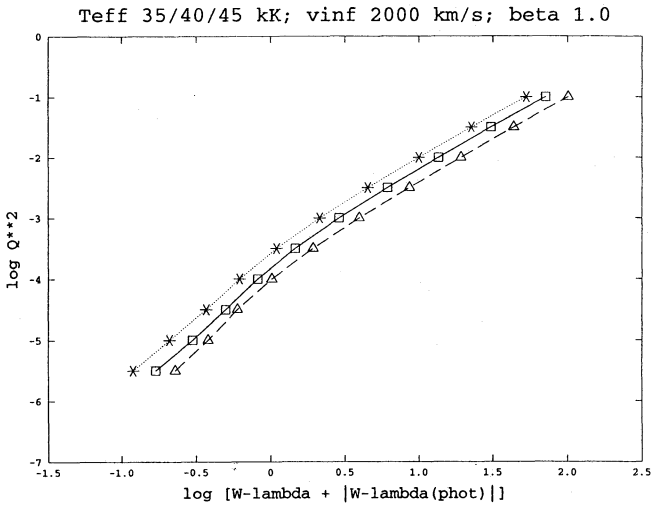


**Fig. 11.** Influence of $T_{\rm eff}$ on the equivalent width of $H_\alpha$ . Triangles: $T_{\rm eff}$ = 35 kK; rectangles: $T_{\rm eff}$ = 40 kK; asterisks: $T_{\rm eff}$ = 45 kK. $\beta$ = 1, $v_\infty$ = 2,000 km/s were adopted, and the HeII blend is included. The photospheric equivalent widths are -3.13, -3.29 and -3.24 Åfor the three values of $T_{\rm eff}$

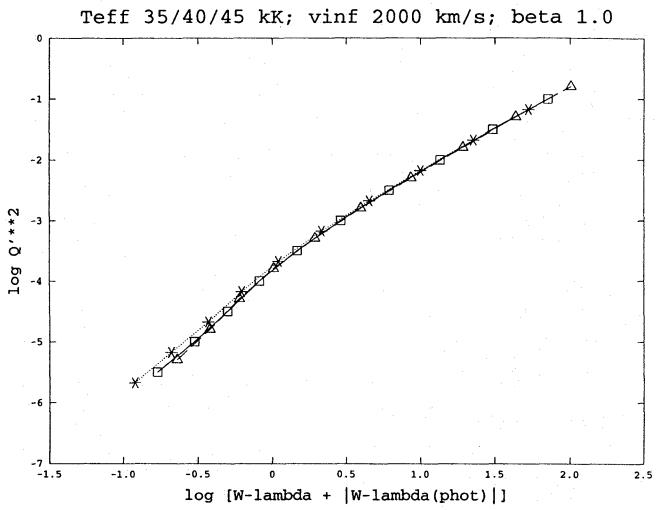


**Fig. 12.** As Fig. 11, but now with an ordinate scaled to $\log Q'^2$ according to Eq. (50) with $T_{\rm ref}$ = 40 kK

Thus, we should be able to scale (for constant $v_\infty$, $\beta$ and Y) the different curves in Fig. 11 to some reference temperature, if we introduce a modified $Q'^2$ by

$$Q^2 \quad \Rightarrow \quad Q'^2 = Q^2 \cdot ct\,, \tag{48}$$

where the "temperature correction factor" $ct$ to a given reference temperature $T_{\rm ref}$ follows from

$$ct(T_{\rm ref}, T_{\rm eff}) = \frac{\Delta\exp(T_{\rm eff})}{\Delta\exp(T_{\rm ref})}\frac{T_{\rm ref}^{3/2}}{T_{\rm eff}^{3/2}} \tag{49}$$

$$\Delta\exp(T) = \exp\left(\frac{E_2 - E_3}{T_{\rm rad}(T)} + \frac{E_3}{T_{\rm e}(T)}\right) - \exp\left(\frac{E_3}{T_{\rm e}(T)}\right).$$

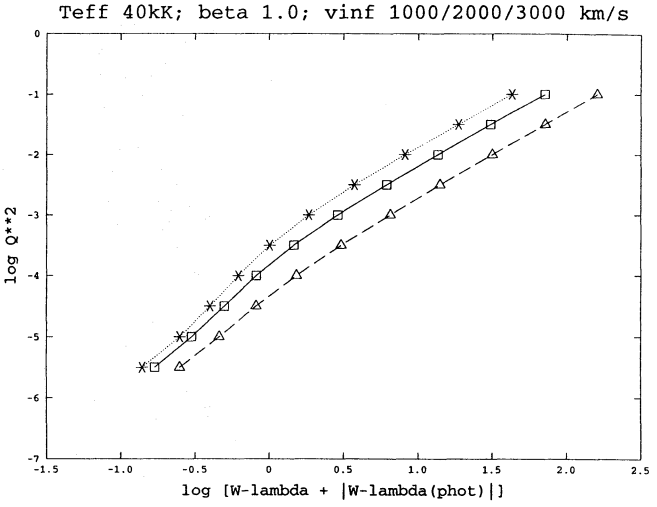


**Fig. 13.** Influence of $v_\infty$ on the equivalent width on the $H_\alpha$ complex. Triangles: $v_\infty$ = 1,000 km/s; rectangles: $v_\infty$ = 2,000 km/s; asterisks: $v_\infty$ = 3,000 km/s. $T_{\rm eff}$ = 40,000 K, $\beta$ = 1 were adopted, and the HeII blend is included

$E_{2,3}$ are the energies of the involved levels. For a reference temperature $T_{\rm ref}$ = 40,000 K and $T_{\rm e} = 0.75T_{\rm eff}$, $T_{\rm rad} = 0.77T_{\rm eff}$, this results in

$$ct(T_{\rm ref} = 40kK, T_{\rm eff}) = 4.2989\frac{\exp\left(\frac{5.184}{T_{\rm eff}}\right) - \exp\left(\frac{2.337}{T_{\rm eff}}\right)}{T_{\rm eff}^{3/2}} \tag{50}$$

($T_{\rm eff}$ in $10^4$ K). Hence, the temperature correction for our above models with $T_{\rm eff}$ = 35, 40 and 45 kK is given by $\log ct$ = 0.206, 0.0 and -0.175, respectively. Applying these correction factors to the $Q^2$ values of Fig. 11 results in Fig. 12, where the *different* relations are now shifted to an almost *unique* curve of growth *independent of* $T_{\rm eff}$ *and the underlying photospheric profile*, if $W'_\lambda$ is plotted as function of $Q'^2$ instead of $Q^2$. The remaining differences (for small values of $Q'^2$) are related to the functional dependency of $b_6$ on $Q$, which especially in this part of the curve of growth is varying faster than for higher wind densities.

### 2.4.4. Influence of $v_\infty$

The last substantial parameter which influences the equivalent width of $H_\alpha$ is the terminal velocity $v_\infty$. Figure 13 shows the corresponding curves of growth. With respect to Eq. (40) and the fact that the departure coefficients are parametrized in terms of $v(r)/v_\infty$, these curves should become almost independent of $v_\infty$ if the ordinate is scaled to $Q^2/v_\infty^{5/3}$. This is done in Fig. 14, where indeed now all three curves define an almost unique relation. The small differences in the lower and intermediate range are primarily due to the different locations of the coupled resonance zones of the H and He line as function of *absolute* velocity. (Note that the line separation of both lines corresponds to 120 km/s.)

The above scaling relation $\log W'_\lambda \sim -5/3 \log v_\infty$ was already derived in Sect. 2.2, however only for the case $\beta$ = 1. A

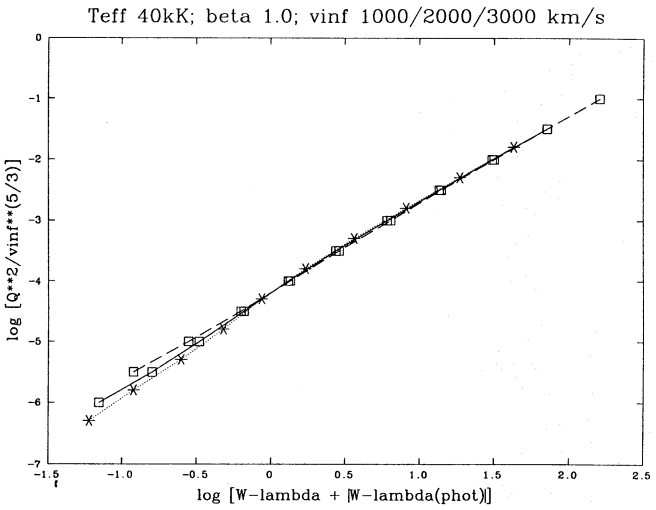


**Fig. 14.** Same as Fig. 13, but now ordinate scaled to $Q^2/v_\infty^{5/3}$ (see text)

priori, for different $\beta$'s other scaling laws are to be expected. However, the differences turn out to be moderate (cf. Fig. 15) and are non-negligible only in the case of very small values of $W'_\lambda$.

### *2.5. A generalized curve of growth for $H_\alpha$*

As demonstrated in Sect. 2.4 we can construct now a generalized curve of growth for $H_\alpha$ by introducing

$$\widetilde{Q}^2 = Q'^2 \,/\, v_\infty^{\frac{5}{3}} \tag{51}$$

The relation $\log\widetilde{Q}^2 = f(\log W'_\lambda)$ should then depend only on the velocity exponent $\beta$ as parameter. This is indeed the case as can be seen from Fig. 15, which uses the grid of approximate calculations presented in Table 7 and the unified model atmosphere results of Table 3

For $W'_\lambda \gtrsim 1$ Å the unified model results follow precisely the generalized curve of growth for $\beta \approx 0.7$ to 0.8. For $W'_\lambda \leq 1$ Å the unified results imply $\beta \approx 1.0$, which was already found and discusses in Sect. 2.3.2.

The generalized curve of growth allows an immediate first estimate of the mass-loss rate provided that $T_{\rm eff}$ and $\log g$ are determined by the analysis of the photospheric lines, that the radius is known from the distance and that $v_\infty$ could be measured from the UV wind lines. One then has simply to measure the equivalent width $W_\lambda$ which then together with $W_\lambda^{\rm phot}(T_{\rm eff}, \log g)$ yields $W'_\lambda$ and finally $\dot{M}$ via $\log\widetilde{Q}^2$

$$\log\left(\frac{\dot{M}}{\mathrm{M}_\odot/\mathrm{yr}}\right) = -6 + \frac{1}{2}\left(\log\widetilde{Q}^2 + \frac{5}{3}\log\left(\frac{v_\infty}{1000\,\mathrm{km/s}}\right) + \log ct(T_{\rm eff}, T_{\rm ref})\right) + \frac{3}{2}\log\left(\frac{R_*}{R_\odot}\right) \tag{52}$$

(The temperature correction factor $ct(T_{\rm eff}, T_{\rm ref})$ is given in the last column of Table 7.) If in a first approximation $\beta = 1$ is used, the accuracy of $\log\dot{M}$ should be better than 0.15 dex for $W'_\lambda \gtrsim 1$ Å. Using the information contained in the shape of the line profile in a next step, it should then be possible to determine $\beta$ and, therefore, to obtain a more precise value of $\log\dot{M}$.

Finally, we note that the generalized curve of growth does also depend on the He abundance (i.e., $Y \neq 0.1$ in general), since the influence of the He blend is non-linear because of the different departure coefficients for H and He. As a first approximation, however, it is only necessary to account for the corresponding factor in Eq. (3) and to introduce an additional correction for $\widetilde{Q}^2$.

## 3. H-alpha mass-loss rates from galactic and Magellanic Clouds O-stars

Having discussed in considerable detail the line formation process of $H_\alpha$ and its dependence on atmospheric parameters, we will use this knowledge to derive mass-loss rates for a sample of Galactic and Magellanic Cloud O-stars. Note that in addition to the use of an improved theoretical treatment of the $H_\alpha$ line formation, the present approach differs from previous work in a number of other aspects. Perhaps the most important of these is that mass-loss rates are derived from line profile fits as opposed to using only equivalent width data. Furthermore, the stellar parameters needed to specify the underlying photospheric $H_\alpha$ line profile were derived for each object from a NLTE model atmosphere analysis rather than simply assigning such parameters on the basis of spectral type and luminosity class. These latter considerations will be especially important for cases where the net emission of the line is small. In addition we consider only those stars for which an estimate of $v_\infty$ is available from the UV, we make no assumptions concerning this quantity based upon spectral type (although for a few stars this criterion is not satisfied). Thus while the present sample of stars is not as extensive as that considered by Leither (1988, 1988a), for example, we expect that the data quality and method of analysis presented here lead to much superior results.

### *3.1. The O-star sample*

It follows that the sample of stars was restricted to those objects for which the required information is present, i.e., that the star was observed in all strategic optical lines to derive the photospheric parameters ($\rightarrow T_{\rm eff}$, $\log g$, $Y$, $v \sin i$), that the distance is well known from association or galaxy membership ($\rightarrow R_*$), and the star was also observed in the UV to derive $v_\infty$.

The core sample of galactic O-stars are those analyzed by Herrero et al. (1992) and Herrero (1994) for which IUE observations exist. These are supplemented by additional O3 stars in the Carina nebula plus some further well-observed stars such as $\zeta$ Pup and $\alpha$ Cam. The Magellanic Cloud star sample comprises of mainly those O-stars which were observed by the Hubble Space Telescope as part of a program aimed at investigating the physics of stellar winds of O-stars in different parent galaxies (see Kudritzki et al. 1992a). In total the sample consists of 24 Galactic, 6 LMC and 8 SMC O-stars, as listed in Table 8.

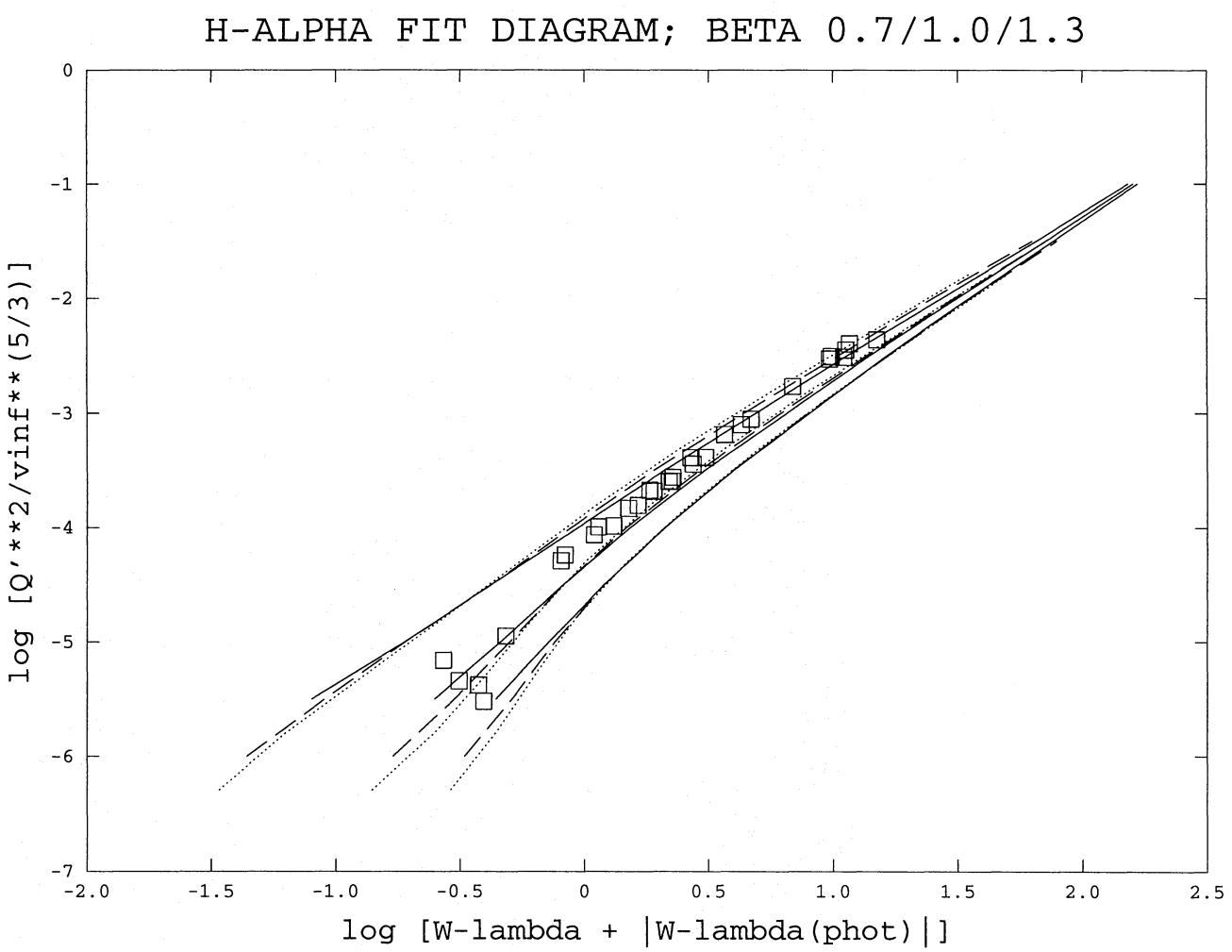


**Fig. 15.** $H_\alpha$ fit diagram for $Y = 0.1$, three values of $\beta = 0.7, 1.0, 1.3$ (upper to lower family of curves) and three values of $v_\infty$ = 1,000, 2,000, 3,000 km/s (fully drawn, dashed, dotted). The ordinate gives the logarithm of $\widetilde{Q}^2$ (Eq. 51) with $v_\infty$ in 1,000 km/s. For the procedure to use this diagram, see text. Overplotted as rectangles are the unified model atmosphere results from Table 3

**Table 7. a** Equivalent width $W_\lambda$ of $H_\alpha$ (including He blend) as function of $Q'^2$ (cf. Eq. 48), $v_\infty$ and $\beta$ for the standard parametrization of the departure coefficients and $Y = 0.1$. Photospheric model with $T_{\rm eff}$ = 40,000 K, log $g$ = 3.70 ($\rightarrow W_\lambda^{\rm phot} = -3.29$ Å).
**b** Temperature correction factor $ct(T_{\rm eff}, T_{\rm ref}) = [ct(T_{\rm ref}, T_{\rm eff})]^{-1}$ (Eq. 50) to derive the actual value of $Q^2$ from $Q'^2$

| | $W_\lambda$(Å) $v_\infty$ = 1,000 km/s | | | $W_\lambda$(Å) $v_\infty$ = 2,000 km/s | | | $W_\lambda$(Å) $v_\infty$ = 3,000 km/s | | | $T_{\rm ref}$ = 40,000 K | |
|---|---|---|---|---|---|---|---|---|---|---|---|
| log$Q'^2$ | $\beta$ = 0.7 | $\beta$ = 1.0 | $\beta$ = 1.3 | $\beta$ = 0.7 | $\beta$ = 1.0 | $\beta$ = 1.3 | $\beta$ = 0.7 | $\beta$ = 1.0 | $\beta$ = 1.3 | $T_{\rm eff}$ (kK) | log$ct$ |
| -5.5 | -3.21 | -3.04 | -2.85 | -3.25 | -3.12 | -2.96 | -3.26 | -3.15 | -3.00 | 35.0 | -.206 |
| -5.0 | -3.10 | -2.83 | -2.57 | -3.20 | -2.99 | -2.78 | -3.23 | -3.04 | -2.85 | 37.5 | -.099 |
| -4.5 | -2.87 | -2.47 | -2.09 | -3.10 | -2.79 | -2.53 | -3.16 | -2.89 | -2.66 | 40.0 | .000 |
| -4.0 | -2.35 | -1.76 | -1.18 | -2.87 | -2.47 | -2.09 | -3.02 | -2.67 | -2.37 | 42.5 | .091 |
| -3.5 | -1.19 | -0.24 | 0.69 | -2.41 | -1.82 | -1.18 | -2.74 | -2.28 | -1.80 | 45.0 | .175 |
| -3.0 | 1.60 | 3.23 | 4.75 | -1.39 | -0.39 | 0.66 | -2.16 | -1.43 | -0.62 | 47.5 | .253 |
| -2.5 | 8.06 | 10.74 | 13.17 | 1.08 | 2.85 | 4.62 | -0.81 | 0.46 | 1.85 | 50.0 | .327 |
| -2.0 | 24.27 | 28.41 | 32.08 | 7.14 | 10.32 | 13.34 | 2.51 | 4.88 | 7.32 | 52.5 | .396 |
| -1.5 | 62.42 | 68.26 | 73.49 | 21.97 | 27.44 | 32.41 | 10.91 | 15.40 | 19.69 | 55.0 | .461 |
| -1.0 | 149.33 | 156.71 | 163.55 | 59.69 | 68.19 | 75.80 | 31.76 | 39.62 | 46.79 | 57.5 | .523 |

**Table 8.** Galactic and MC O-star sample and used/deduced atmospheric parameters. $T_{\rm eff}$ in kK, $R_*$ in $R_\odot$, $v \sin i$, $v_\infty$ in km/s, $M_*$ in $M_\odot$, $L$ in $L_\odot$, $\dot{M}$ in $10^{-6}{\rm M}_\odot$/yr. Bold face numbers for $\beta$ denote derived values, others are assumed ones. $r_4^{\rm in}$ and $r_6^\infty$ give the ratio of He(i=4,6) departure coefficients to values of standard parametrization (Table 5) if different from unity

| star | classif. | $T_{\rm eff}$ | $\log g^{1)}$ | $\log g^{2)}$ | $R_*$ | $Y$ | $v \sin i$ | $v_\infty$ | $\log L$ | $M_*$ | $\dot{M}$ | $\beta$ | $r_4^{\rm in}/r_6^\infty$ |
|---|---|---|---|---|---|---|---|---|---|---|---|---|---|
| | | | | | | Galaxy | | | | | | | |
| HD 93128 | O3 V ((f)) | 52.0 | 4.00 | 4.00 | 10. | 0.10 | 100 | 3100[4)] | 5.82 | 36.5 | $\leq 1.2$ | 0.80 | |
| HD 93250 | O3 V ((f)) | 50.5 | 3.95 | 4.00 | 18. | 0.10 | 100 | 3250 | 6.28 | 118. | 4.9 | 0.80 | |
| HD 93129A | O3 I f* | 50.5 | 3.80 | 3.95 | 20. | 0.10 | 130 | 3200 | 6.37 | 130. | 22.0 | **0.85** | 1.15/[6)] |
| HD 303308 | O3 V ((f)) | 48.0 | 4.05 | 4.10 | 12. | 0.10 | 100 | 3100 | 5.84 | 66. | 2.1 | 0.80 | |
| $\zeta$ Pup | O4 I (f) | 42.0 | 3.50 | 3.60 | 19. | 0.12 | 220 | 2250 | 6.00 | 52.5 | 5.9 | **1.15** | 1.6/[7)] |
| HD 15558 | O5 III (f) | 48.0 | 3.80 | 3.85 | 21.8 | 0.08 | 120 | 2800 | 6.36 | 122.7 | 7.3 | 0.75 | |
| HD 15629 | O5 V ((f)) | 47.0 | 3.90 | 3.90 | 14.2 | 0.08 | 90 | 3000 | 5.95 | 58.5 | 0.75 | 1.00 | |
| HD 193682 | O5 III (f) | 45.0 | 3.60 | 3.65 | 12.2 | 0.43 | 200 | 2800[4)] | 5.74 | 24.3 | 1.3 | 0.80 | |
| HD 14947 | O5 I f$^+$ | 43.5 | 3.45 | 3.50 | 16.1 | 0.18 | 140 | 2350 | 5.93 | 30. | 7.5 | **1.00** | 1.5/.6 |
| $\lambda$ Cep | O6 I(n) fp | 38.0 | 3.60 | 3.65 | 19. | 0.10 | 100 | 2250 | 5.83 | 59. | 5.3 | **0.90** | 1.4/[7)] |
| HD 190864 | O6.5 III (f) | 41.0 | 3.55 | 3.55 | 14.1 | 0.20 | 105 | 2500 | 5.71 | 25.7 | 1.5 | 0.80 | 1.3/ |
| HD 217086 | O7 V n | 40.0 | 3.60 | 3.75 | 10.3 | 0.20 | 375[3)] | 2550 | 5.39 | 21.8 | $\leq$0.2 | 1.00 | |
| HD 192639 | O7 Ib (f) | 38.5 | 3.40 | 3.45 | 19.5 | 0.25 | 125 | 2150 | 5.88 | 39. | 6.0 | **0.95** | 1.5/.65 |
| HD 193514 | O7 Ib (f) | 38.0 | 3.40 | 3.45 | 19.8 | 0.14 | 105 | 2200 | 5.87 | 40.3 | 4.2 | 0.75 | 1.4/.3 |
| HD 203064 | O7.5 III:n ((f)) | 37.5 | 3.50 | 3.65 | 14.1 | 0.14 | 315[3)] | 2550 | 5.55 | 32.4 | 1.2 | 0.80 | |
| $\xi$ Per | O7.5 III (n)((f)) | 36.0 | 3.30 | 3.40 | 25.5 | 0.22 | 250[3)] | 2450 | 6.0 | 59.6 | 3.2 | 0.75 | |
| HD 13268 | ON8 V | 35.0 | 3.30 | 3.50 | 11.7 | 0.25 | 320[3)] | 2150 | 5.27 | 15.8 | $\leq$0.05 | 1.00 | |
| HD 191423 | O9 III : n* | 34.0 | 3.40 | 3.70 | 13. | 0.25 | 450[3)] | 1150[5)] | 5.31 | 31. | 0.20 | 0.80 | |
| HD 207198 | O9 Ib-II | 34.0 | 3.30 | 3.30 | 15.1 | 0.14 | 80 | 2150 | 5.44 | 16.6 | 1.6 | 0.75 | 1.95/.4 |
| HD 210809 | O9 Iab | 33.0 | 3.10 | 3.15 | 21.7 | 0.14 | 100 | 2100 | 5.7 | 24.3 | 4.0 | **0.93** | 1.7/.55 |
| $\zeta$ Oph | O9 III | 32.5 | 3.70 | 3.85 | 12.9 | 0.19 | 400[3)] | 1550: | 5.22 | 43. | $\leq$0.03 | 1.00 | |
| HD 209975 | O9.5 Ib | 32.5 | 3.20 | 3.20 | 17.2 | 0.10 | 100 | 2050 | 5.47 | 17. | 0.9 | 0.80 | |
| HD 18409 | O9.7 Ib | 31.5 | 3.10 | 3.15 | 16.1 | 0.14 | 160[3)] | 1750[4)] | 5.36 | 13.4 | 0.5 | 0.80 | |
| $\alpha$ Cam | O9.5 Ia | 30.0 | 2.95 | 3.00 | 29. | 0.20 | 80 | 1550 | 5.79 | 30.7 | 5.2 | **1.10** | 1.5/.2[7)] |
| | | | | | | LMC | | | | | | | |
| Sk $-67°$ 211 | O3 III (f*) | 60.0 | 4.10 | 4.15 | 17.8 | 0.10 | 100 | 3750 | 6.57 | 163. | 10. | 0.75 | |
| Sk $-68°$ 137 | O3 III (f*) | 60.0 | 4.05 | 4.10 | 12.4 | 0.10 | 100 | 3400 | 6.26 | 70.6 | 8. | 0.75 | |
| Melnick 42 | O3 If/WN | 50.5 | 3.80 | 3.90 | 26. | 0.10 | 240 | 3000 | 6.60 | 196. | 35. | **0.55** | |
| Sk $-67°$ 166 | O4 I f$^+$ | 47.5 | 3.60 | 3.65 | 19.5 | 0.10 | 80 | 1900 | 6.24 | 62. | 13.0 | **0.67** | 1.15/.5 |
| Sk $-67°$ 167 | O4 Inf$^+$ | 47.5 | 3.60 | 3.65 | 17.9 | 0.10 | 120 | 2150 | 6.17 | 52.8 | 14.0 | **0.75** | 1.15/.1 |
| Sk $-66°$ 100 | O6 II (f) | 43.5 | 3.70 | 3.75 | 13.2 | 0.13 | 80 | 2150 | 5.75 | 35.8 | 1.9 | 0.75 | 1.5/ |
| | | | | | | SMC | | | | | | | |
| NGC 346#3 | O3 III f* | 55.0 | 3.90 | 3.90 | 12.3 | 0.10 | 100 | 2900 | 6.10 | 44. | 2.3 | 0.80 | |
| AV 388 | O4 V | 48.0 | 3.70 | 3.70 | 10.7 | 0.10 | 120 | 2100 | 5.74 | 21. | $\sim$0.17 | 1.00 | |
| AV 243 | O6 V | 45.0 | 3.70 | 3.70 | 12.3 | 0.10 | 80 | 2050 | 5.75 | 27.7 | $\leq$0.1 | 1.00 | |
| NGC 346#1 | O4 III (n)(f) | 42.0 | 3.60 | 3.65 | 23.3 | 0.10 | 200 | 2650(:) | 6.18 | 88.5 | 4.8 | 0.80 | |
| NGC 346#4 | O5-6 V | 42.0 | 3.80 | 3.85 | 14.2 | 0.10 | 250 | 1550: | 5.75 | 52. | $\leq$0.1 | 1.00 | |
| NGC 346#6 | O4 V ((f)) | 40.0 | 3.70 | 3.70 | 12.2 | 0.10 | 100 | 2250 | 5.54 | 27.2 | $\leq$0.3 | 1.00 | |
| AV 232 | O7 Iaf$^+$ | 37.5 | 3.20 | 3.30 | 29.3 | 0.20 | 80 | 1400 | 6.19 | 62.5 | 5.5 | **1.40** | 1.5/.35[7)] |
| AV 238 | O9 III | 35.0 | 3.50 | 3.50 | 15.5 | 0.10 | 60[3)] | 1200: | 5.51 | 27.7 | $\sim$0.13 | 1.00 | |

[1)] fit-value for photospheric plus stellar wind profile in $H_\gamma$ (see text).
[2)] "true" value including "unified model atmosphere" and centrifugal correction (see text).
[3)] other value applied for $H_\alpha$ profile fit (see text).
[4)] $v_\infty$ estimated from spectal type.
[5)] $v_\infty$ from $0.85 v_*$ (Howarth & Prinja 1989), rather uncertain (see text).
[6)] modified value for $r_4^\infty = 1.8$.
[7)] modified value for $b_3$(H)(see text).
:, (:) uncertain $v_\infty$-determination, see text

#### 3.1.1. Observations and data reduction

The $H_\alpha$ observations of the galactic stars taken from Herrero et al. (1992) and Herrero (1994) were carried out with the 2.5 m Isaac Newton Telescope at the Observatory of El Roque de los Muchachos in La Palma in July and October 1989, and in August 1992. The Intermediate Dispersion Spectrograph (IDS) was used with the 1800 V grating with the 235 mm camera, which resulted in a resolution of 0.8 Å FWHM while the measured S/N of the resulting data was typically around 300. The blue observations used for the derivation of the photospheric parameters were obtained on the same dates with an additional run in September 1991. These data are described in the references given above, briefly however the spectral resolution was 0.6 Å FWHM, the S/N ranging from 150 to 200. Additional red spectrograms of HD207198, HD209975 and $\alpha$ Cam were obtained with a similar instrumental setup as described above (see Lennon et al. 1993 for details) while data for the Carina stars, HD93128, HD93250, HD93129A and HD303308 were obtained in December 1992 using the ESO New Technology Telescope (NTT) and the EMMI spectrograph. This latter dataset consisted of spectrograms covering the wavelength ranges 3920 – 4380 Å and 6300 – 6800 Å at a resolution of 0.9Å and 1.1Å respectively, the S/N being in excess of 200. Finally, for the galactic star sample, the data for $\zeta$ Pup were taken from Bohannan et al. (1990) where further details of the observational material and data reduction procedures may be found.

Blue spectra for O-stars in the Magellanic Clouds (excluding Mk42) were obtained using the ESO 3.6m telescope and Caspec echelle spectrograph during two observing runs in 1984 and 1985. The resolution of these data is approximately 0.5Å while S/N ratios range from 30 to 70, further details of these data may be found in Walborn et al. (1995). Red spectrograms with similar resolution and S/N for the LMC stars plus 4 SMC stars (NGC346#1, #3, #4 and AV232) were also obtained with the ESO 3.6m telescope and Caspec in November 1990 (excepting AV232 which was observed in October 1991). A blue spectrogram of Mk42 was also obtained at this time. Of the remaining SMC stars, $H_\alpha$ data were obtained for AV388, AV243 and AV238 using EFOSC in echelle mode on the ESO 3.6m telescope in November 1988. Note that the EFOSC data have a resolution of approximately 3.0Å at $H_\alpha$ which is significantly lower that that of the rest of the sample. Finally, NGC346#6 was observed in the red during December 1993 using the EMMI spectrograph on the NTT at a resolution of 1.1Å and a S/N of 40.

The reduction of the visible region data was performed following the standard procedures of bias substraction, flat field division, spectrum extraction, wavelength calibration and continuum rectification. Various packages were used for the reduction including IRAF[2], FIGARO (Shortridge 1987), Midas and locally developed programs.

[2] The IRAF package is distributed by the National Optical Astronomy Observatories, which is operated by the Association of Universities for Research in Astronomy, Inc., under contract with the National Science Foundation

The IUE dataset for the galactic O-stars used in this work is identical to that used by Howarth & Prinja (1989) and has been extensively described there. These data were kindly sent to one of us (SMH) by the authors. The UV spectrum of Mk42 was obtained with the GHRS aboard the HST as described by Heap et al. (1991), where further details may be found. All the other Magellanic Cloud stars were observed with the Faint Object Spectrograph (FOS) aboard HST, and these observations plus the corresponding optical data are discussed more fully in Walborn et al. (1995). Note that spectral types are also taken from this paper.

#### 3.1.2. Determination of $T_{\rm eff}$, $\log g$, $Y$ and $v \sin i$

The hydrogen and helium lines in the spectral range between 4000 and 5000 Å were used to determine $T_{\rm eff}$, $\log g$ and $Y$. This standard technique has been described in detail many times (see, e.g., Kudritzki & Hummer 1990; Herrero et al. 1992; Herrero 1994). Plane-parallel and hydrostatic NLTE models were used for that purpose with the underlying assumption that the effects of winds on the absorption lines in this spectral range are small. Of course, we admit that according to Gabler et al. (1989), Sellmaier et al. (1993) and Schaerer & Schmutz (1994) this assumption requires a careful reinvestigation. Consequently, detailed spectral analyses based on metal line blanketed unified models are presently under way in our group. However, for samples as large as the present one this represents a major effort. Therefore, at the present stage, we continue to work with the standard technique. Nevertheless, we do apply a correction that accounts for the most important effect arising from the application of unified model atmospheres, namely that concerning the determination of the surface gravities. Gabler et al. have shown that stellar winds, if they are strong, do not only affect $H_\alpha$ but also $H_\beta$ and $H_\gamma$ . Sellmaier et al. and Schaerer & Schmutz have added further evidence in this direction. As a result, gravities derived from Stark broadened wings of $H_\gamma$ using hydrostatic NLTE models are systematically to low because of *a)* wind emission filling in the photospheric profile as for $H_\alpha$ and *b)* the density at optical depth unity is smaller in atmospheres with a wind than without one. We account for both effects in an approximate way.

Effect *a)* can be treated very easily by carrying out the same approximate line formation treatment for $H_\gamma$ as for $H_\alpha$ (cf. the correponding departure coefficients in Tables 4 and 5). In this way, the stellar wind contribution to the photospheric profile is quite well accounted for and the profile fitting of $H_\gamma$ is straightforward. Of course, now the determination of $\log g$ from $H_\gamma$ has to be done iteratively together with the determination of $\dot{M}$ from $H_\alpha$ . We start with $H_\gamma$ and a purely hydrostatic model for a first estimate of $\log g$. Then we use the corresponding $H_\alpha$ profile as input for the $\dot{M}$-determination from $H_\alpha$ . With this $\dot{M}$-value we then account for wind emission in $H_\gamma$ and derive a new $\log g$. The iteration of this process leads to the $\log g$-values of the fourth column in Table 8.

The treatment of effect *b)* is more complicated. Figure 16 shows the density stratifications for a hydrostatic and a unified

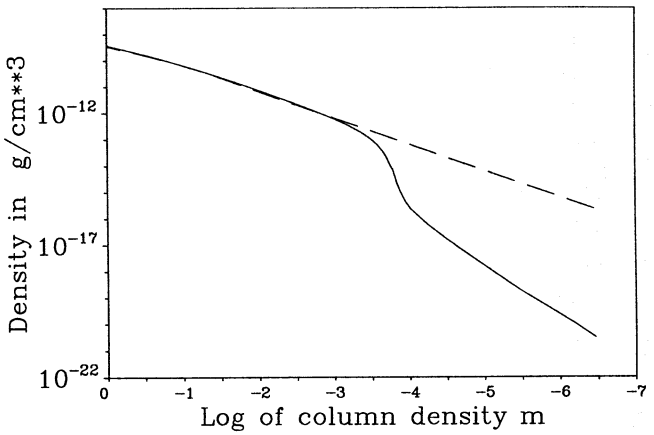


**Fig. 16.** Mass density $\rho$ as function of logarithm of atmospheric column density $m$ for a typical unified model (solid) and a hydrostatic model (dashed) with similar $T_{\rm eff}$ and $\log g$

model with similar $T_{\rm eff}$ and $\log g$ as a function of atmospheric column density (proportional to Thomson optical depth)

$$m = R_* \int_r^\infty \rho {\rm d}r. \qquad (53)$$

The sonic point of the hydrodynamic unified model of Fig. 16 is located at $\log m = -3.9$, where $\log \rho$ shows the steep gradient. In the supersonic region ($\log m < -3.9$) the density in the unified model is much smaller whereas - naturally - it approaches the hydrostatic values in the subsonic region. The location of the sonic point depends, of course, on the mass-loss rate and moves inwards with increasing $\dot{M}$.

The wings of $H_\gamma$ are normally formed in the subsonic region, but depending on $\dot{M}$ the densities here can still be substantially lower than in the simple hydrostatic calculations, so that Stark broadening is less effective. Consequently, one would need a larger $\log g$ than in the purely hydrostatic case to fit the observed $H_\gamma$ profile. In Appendix A we give a simple analytical estimate of this additional $\log g$-correction, which we have applied to all the stars in our sample using the values of $\dot{M}$ and $\beta$ derived from $H_\alpha$ . In addition, we also apply the "centrifugal correction" of $\log g$, as it was introduced by Herrero et al. (1992) to account for centrifugal forces influencing the effective gravity (cf. also Sect. 2.1.1). These two corrections together lead to the "true" $\log g$-values of column five in Table 8.

The projected rotational velocities ($v \sin i$) needed for the centrifugal correction were obtained from profile fits of weak lines unaffected by pressure broadening.

### 3.1.3. Stellar radii

Stellar radii were obtained from dereddened absolute magnitudes and model atmosphere fluxes using the procedure outlined by Kudritzki (1980; see also Herrero et al. 1992). We note that distances and therefore absolute magnitudes are uncertain for several of our galactic objects.

For the LMC and SMC distance moduli of $18.5^{\rm m}$ and $19.1^{\rm m}$, respectively, were adopted, and apparent magnitudes from recent CCD photometry were used preferentially, where available.

### 3.1.4. Terminal velocities

The terminal velocities $v_\infty$ have been determined by fits to the P-Cygni profiles of the UV resonance lines of NV, SiIV, and CIV. To perform the fit we solve the exact equation for the formal integral together with the Sobolev approximation for the source function. As shown by Hamann (1981) and Lamers et al. (1987), this yields very accurate results almost indistinguishable from the exact comoving frame solution for the source function. As in Groenewegen & Lamers (1989) we allow for "microturbulence", however, contrary to them we do not adopt a constant value but let $v_{\rm turb}$ increase from $v_{\rm turb} = 0.02...0.03 v_\infty$ (corresponding to 50...60 km/s) at $r = R_*$ to $v_{\rm turb}^{\rm max}$ at $v = v_\infty$. A description of the method has been given by Haser et al. (1995).

For all objects of Table 8 that show steep blue absorption edges in at least two of the three above resonance lines, $v_\infty$ can be fitted (together with $v_{\rm turb}^{\rm max}$) with an accuracy of $\pm$ 40 km/s. However, accounting for the inherent blue edge variability (see Henrichs 1991; Prinja et al. 1992) and the contamination of the edges by underlying photospheric lines, the $v_\infty$-values of Table 8 should generally regarded as accurate to $\pm$ 5...10 %. In a few cases of weak winds (the galactic O9 III star $\zeta$ Oph and some SMC O-stars), no strong lines with steep blue edges are present and $v_\infty$ might be severely underestimated because of the change in ionization towards the outer wind. These cases are indicated by ":" in Table 8.

For the majority of our sample stars the analysis did not pose any serious problem. In the following we will comment only on those objects where the determination of $v_\infty$ was somewhat more difficult. In the spectra of HD 93129A, HD 15558, and HD 15629 only the CIV lines could be used: The NV profiles are corrupted either by a strong interstellar $Ly_\alpha$ absorption trough, leading to an invisible blue edge (HD 93129A), or the S/N is too poor (HD 15558, HD 15629) and the SiIV profiles are absent or too weak (HD 15558). Furthermore, the blue wings of the absorption troughs of HD 15558 and HD 93129A are very shallow, suggesting that CIV is being depopulated in the outermost parts of the winds. Hence, their derived terminal velocities are somewhat more uncertain by ~200 km/s (HD 15558) or even ~ 400 km/s (HD 93129A). In our subsequent analysis we used the lower limits for $v_\infty$. In fact a few of our targets were observed by the ORFEUS-mission and it turns out that for these stars this lower limit is consistent with the observed OVI $\lambda\lambda$1032/1038 resonance lines (Taresch, private communication). In the case of $\zeta$ Oph only CIV was usable for an (uncertain) fit, with the NV profile consisting almost exclusively of Discrete Absorption Components (DACs).

HD 191423 shows peculiar P-Cygni profiles similar to those of HD 93521 (see Howarth & Reid 1993). A fit with a spherically symmetric flow model is not applicable here (see also below). $v_\infty$ has been estimated then from the maximum edge velocity $v_\infty \approx 0.85 v_*$ (cf. Howarth & Prinja 1989).

The terminal velocity for the SMC and LMC objects are taken from Haser et al. (1994). The observations for three more stars in NGC346 in the SMC have just recently been performed (NCG346#3, #4 and #6) and were analyzed in a similar fashion (Walborn et al. 1995).

For all MC stars (except Mk 42) the instrumental profile of the FOS of FWHM $\approx$ 1 Å (corresponding to 230 km/s at 1300 Å) has been taken into account by convolving the model profile with a Gaussian, where one has to ensure that the steepest wings of the model profile are sufficiently resolved numerically prior to convolution. Due to the extraordinary data quality this does not significantly affect the accuracy of the derived values for $v_\infty$. Only for two stars in the SMC (NGC346#4 and AV 238) are the P-Cygni profiles so weak that only the CIV line could be used for an (uncertain) fit.

NGC346#1 is a multiple system (Heydari-Malayeri & Hutsemékers 1991). The CIV and NV profiles show a considerable residual intensity in the absorption troughs although morphologically resembling saturated lines. If the residual intensity is artificially removed, the derived $v_\infty$ decreases from 2650 km/s to a minimum value of 2250 km/s due to the increased effect of turbulence at the blue edges. Since the flux contribution of the companions is quantitatively unknown, we have retained the value of $v_\infty$ = 2650 km/s, which corresponds to the uncorrected flux level. This uncertainty is indicated by "(:)" in Table 8.

For three stars (HD 93128, HD 193628, HD 18409) no UV spectra are available, so $v_\infty$ was estimated from its spectral type. The error is supposed not to exceed $\approx$ 400 km/s.

#### 3.1.5. Radial velocities $v_{\rm rad}$

It turns out that a significant parameter affecting the results is the correction for the stellar radial velocity $v_{\rm rad}$. One reason for this is that in the present approach the parameters $\beta$ and/or especially $b_{4,6}$ are treated as fit parameters and therefore an erroneous radial velocity correction may be falsely compensated for by an inappropriate choice of these parameters. (Obviously, this problem will not arise in the curve of growth approach.) In fact for reliable results the radial velocity correction has to be known with a precision better than 20 km/s. The $H_\alpha$ line itself cannot be used to determine $v_{\rm rad}$ both for the reason we have just mentioned but also because all the hydrogen Balmer series lines have a He II line blended on the blue side and so the position of the line centroids depend upon the helium abundance. Clearly, lines other than $H_\alpha$ must be used to determine the radial velocity correction (and the helium abundance, see Sect. 3.1.2).

The determination of $v_{\rm rad}$ for O-stars with the required accuracy is complicated by a number of factors. At these temperatures only a small number of useful "photospheric" lines are present in the spectra. Furthermore, the wind itself may produce both an asymmetry and a shift of the observed line center for those remaining lines. (Note that also the so-called *photospheric* lines are actually formed in an expanding medium with outflow velocities not too different from the above mentioned accuracy level, see Kudritzki 1992.) Furthermore, the projected rotational velocities of O-stars may be quite large, increasing the uncertainty associated with the measurement of line centers. The determination of the radial velocity correction in the critical $H_\alpha$ region is particularly problematical as we must rely entirely upon HeI or HeII lines or else resort to the adoption of values derived from blue spectral data (while recognizing that there may be systematic differences between red and blue).

For the hotter stars, those with strong HeII lines and weak or absent HeI, we used one or more members of the HeII Pfund series lines at $\lambda\lambda$6683, 6527 and 6406, while for cooler stars (late O) we use the HeI $\lambda$6678 line. For a number of stars, particularly in the Magellanic Clouds, the S/N was not sufficient to permit the use of the HeII lines (which are Stark broadened) and we adopted the radial velocities as derived from the blue spectrograms although in addition when possible we used nebular lines to correct for offsets between blue and red spectra. In general the uncertainty in the derived value of $v_{\rm rad}$ is of the order $\pm$20km/s although in some cases it is considerably better than this.

### 3.2. *H-alpha mass-loss rates*

With all required parameters now specified, we are able to deduce the stellar $\dot{M}$ by a detailed fit to the $H_\alpha$ profile. We prefer the method of profile fits relative to the curve of growth method derived above for the following reasons:

- The profile fitting method, through its ability to optimize the values of $\beta$ and the boundary values of the departure coeffients (should they deviate from the "standard parametrization", see below) intrinsically allows a more accurate estimate of $\dot{M}$.
- Many of our galactic objects show an enriched He abundance (the so-called He discrepancy, cf. Herrero et al. 1992), which favours a distinct profile fit instead of calculating a variety of curve of growth diagrams to account correctly for this parameter.
- For a large number of our objects (the Carina and MC stars), the innermost part of the profile is heavily contaminated by nebula emission of the surrounding HII region, so that the specification of a measured equivalent width is difficult. In view of the fact that it is not the total equivalent width $W_\lambda$ which is decisive, but rather the value of $W'_\lambda$ (i.e., corrected for the photospheric equivalent width ), this error may become intolarable for stars with a low wind density, where an only small portion of the profile is refilled by wind emission.
- By comparing theoretical profile shapes to the observed ones, it is also possible to extract the "problematic" cases easily, i.e., those ones, which in the framework of our assumptions cannot be modelled and may thus point to presently unsolved problems and/or different physical processes.
- Finally, these line fits can be performed interactively on a workstation with almost no perceptible time delay between input and output. Thus, the analysis of even a large sample of objects is not hampered by the fitting approach.

3.2.1. Fit procedure

The actual fit procedure works as follows (exceptions are discussed in the next section). As a first guess, following Sect. 2.3, we use a value of $\beta = 1.0$ for $W'_\lambda < 0.5$ Å, $\beta = 0.8$ for 0.5 Å$\leq W'_\lambda <$1.3 Å and $\beta = 0.75$ for $W'_\lambda \geq$1.3 Å. Using the $b_i$'s from Tables 4 and 5 we first perform calculations with a guess for $\dot{M}$, this guess being modified iteratively to optimize the fit. In many cases this simple procedure gives a very good fit and a good determination of $\dot{M}$. For a number of objects (actually for almost all *supergiants*), we found that in order to model the blue wing we had to increase the He-opacity in the inner wind part – corresponding to an increase of $b_4^{\rm in}$ – and to reduce the emissivity outside, i.e., $b_6^\infty$ had to be lowered. Fortunately, both quantities can be easily adjusted with sufficient accuracy because of the *asymmetric* reaction of the profile to their changes.

The second step of the fit procedure is to carefully adapt the mass loss rate and $b_6^\infty$ to model the almost $\beta$-independent high-velocity wings (if present). As the shape of the central emission peak (if present) is primarily controlled by the velocity field (high and narrow emission for large, low and broad emission for small $\beta$), $\beta$ is finally adjusted together with $b_4^{\rm in}$ (and partly $\dot{M}$) to fit the total profile. For those cases where the wind emission is smaller than the photospheric absorption, we adjust only $b_4^{\rm in}$ and $\dot{M}$ while leaving $\beta$ at its standard value dependent on $W'_\lambda$.

Table 8 (last three columns) lists the derived mass-loss rates, $\beta$'s and modified $b_i$'s, and Fig. 17 demonstrates the typical fit quality for our stellar sample. In the following, we give some general remarks and then discuss those objects where individual comments are appropriate.

3.2.2. General remarks: departure coefficients, rotational velocities and derived $\beta$-values

When performing the individual profile fits, it was immediately clear that most of the supergiants exhibit a profile which cannot be fitted with our standard parametrization of the HeII departure coefficients. Most striking are those cases with a total equivalent width somewhat larger than zero, where the line shape resembles a P Cygni profile. Here, obviously, the absorption has to be attributed to the He blend, which can be simulated in our approach by increasing the He opacity in the lower wind part, typically by a factor of 1.5 (cf. the last column of Table 8). On the other hand, for a number of those objects we had additionally to lower the He emission in the outer wind part by decreasing the corresponing standard value of $b_6^\infty$ (a typical factor here is 0.3). A possible reason for this discrepancy in comparison to the unified atmosphere results may be the neglect of the effects of (EUV) line blocking (cf. Pauldrach et al. 1994; Schmutz & Schaerer 1994) in our present calculations, which become particularly important in dense winds. This problem will be thoroughly discussed in a forthcoming paper, where recent test calculations actually show that this effect yields a trend in the correct direction, i.e., changing the He occupation numbers, while keeping the hydrogen population almost unaffected.

As pointed out above, our parametrization of the hydrogen departure coefficients provided no difficulties when used for a line fit to *observed* profiles. The only cases where we had to perform a rather moderate change are $\zeta$ Pup, $\lambda$ Cep, $\alpha$ Cam and AV 232. For those objects, which exhibit a strong decline from the emission maximum towards the (He-) absorption minimum, we were forced to lower the hydrogen emission in the inner wind part by decreasing the value of $b_3^{\rm in}$ from 1.2 to 1.1 for $\lambda$ Cep, $\alpha$ Cam, AV232 and to 0.9 for $\zeta$ Pup. This corresponds to a reduction of the source function by a factor 0.88 for the first three objects and 0.65 for the latter one, respectively.

*It is important to note here that the final values of $\dot{M}$ are only weakly affected by these modifications of the departure coefficients, since the line opacity scales with $\dot{M}^2$ but only linearly with the $b_i$'s.*

For those of our objects with a large rotational velocity (denoted by the superscript [3)] in Table 8), we had to modify $v \sin i$ to a smaller value in order to simulate the observed profiles. This may be explained by the fact that the wind emission is formed in a differentially rotating medium with an "effective" rotational speed smaller than the *photospheric* one given in Table 8. Actually, for those fast rotating objects one would have to perform a formal solution taking into account the differential rotation exactly. This will be done in a forthcoming paper, where we will show that – with respect to profile shape – the effects are largest for objects with an equivalent width of roughly zero and a "P Cygni" shape. However, as was mentioned in Sect. 2.1.2, the resulting equivalent width remains almost unaffected even if this process is included, so that our procedure of adapting $v \sin i$ should lead to no significant errors as long as the synthesized profile fits the observed one well.

As pointed out above, those objects with $H_\alpha$ in emission allow one to derive the $\beta$-value in parallel with the mass-loss rate (Table 8, $\beta$- values in bold face). For the galactic supergiants, an average value of $\beta = 1.0$ is found consistent with the UV line analysis. The only object which seems to show some contradictions is $\zeta$ Pup with $\beta = 1.15...1.20$, where UV line fits indicate a smaller value ($\approx 0.8...0.9$, cf. also Groenewegen & Lamers 1989). However, from the shape and strength of the emission peak a value of $< 1.1$ can be excluded.

In contrast, all three LMC objects for which a determination of $\beta$ is possible show a value $\lesssim 0.75$, where Mk42 has the fastest acceleration in our sample with $\beta \approx 0.55$. Finally, the only SMC object with $H_\alpha$ in emission, AV 232, is an extreme supergiant with a rather low terminal velocity and a large $\beta = 1.40$.

3.2.3. Comments on individual objects

**Galactic O-stars**

*HD 93128.* For this star (Fig. 17a), we can only derive an upper limit of $1.2 \cdot 10^{-6} M_\odot$/yr, as the line center is heavily contaminated by nebula emission and lower $\dot{M}$'s have no effect onto the visible wings. The maximum possible value for HD 93128 is $1.5 \cdot 10^{-6} M_\odot$/yr.

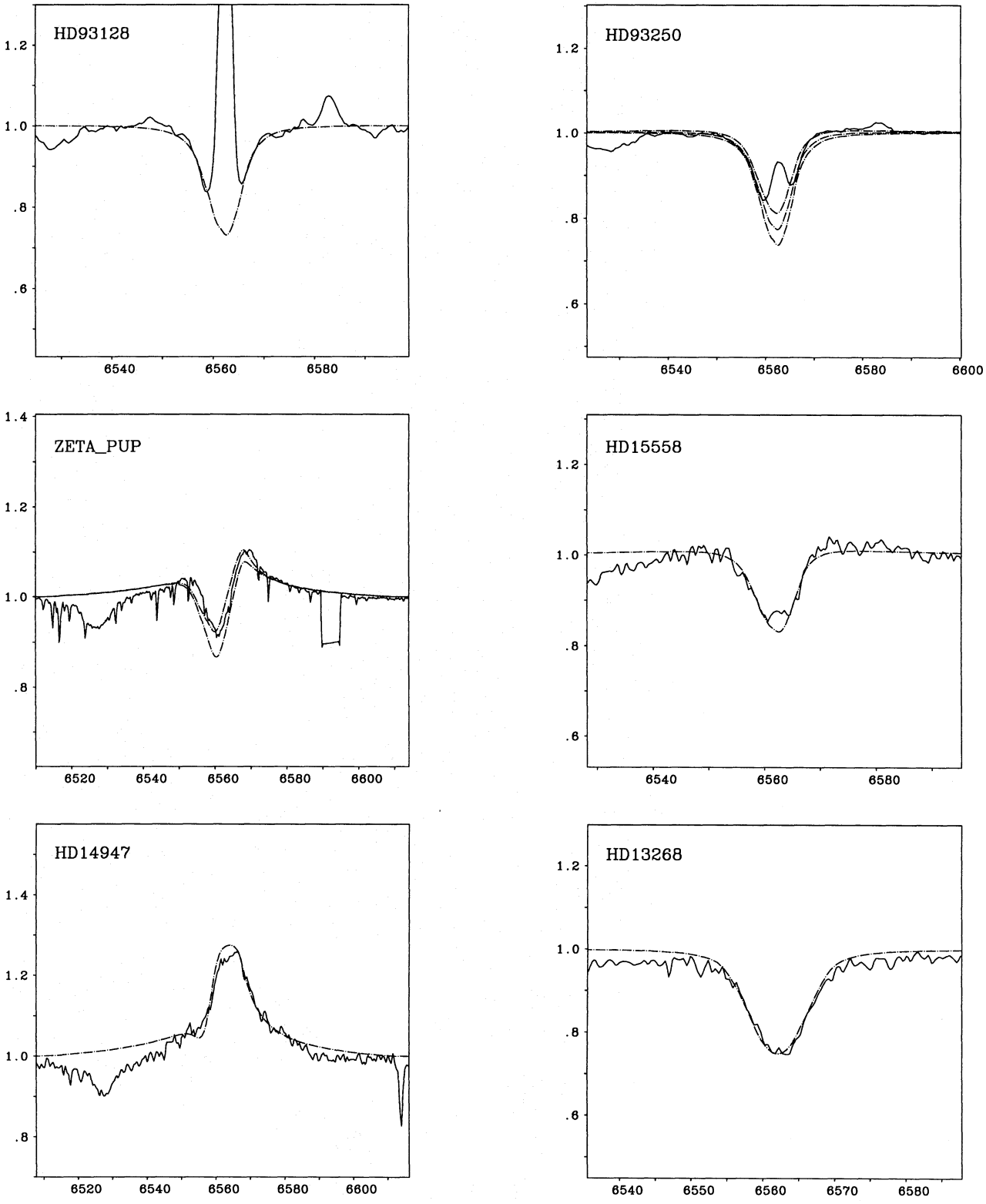


**Fig. 17a–l.** Typical examples for detailed line fits, see text

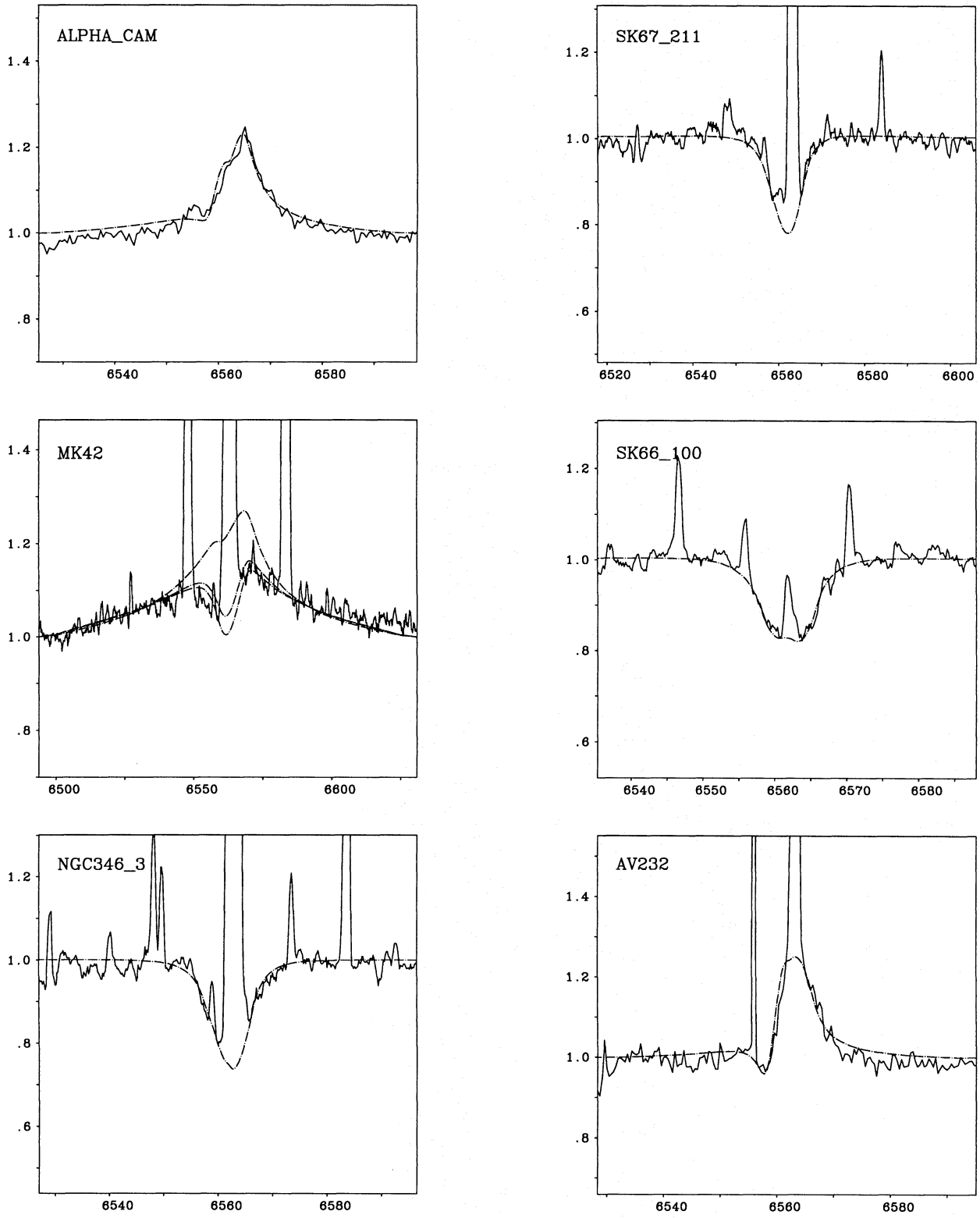


**Fig. 17.** (continued)

*HD 93250.* As for HD 93128, only the wings can be fitted here. Figure 17b shows the sensitivity to different values of $\dot{M}$, where the upper curve corresponds to $\dot{M} = 6.4 \cdot 10^{-6} M_\odot/yr$ and the lower one to $3.4 \cdot 10^{-6} M_\odot/yr$. The best fit is obtained for $\dot{M} = 4.9 \cdot 10^{-6} M_\odot/yr$.

*HD 93129A.* From the shape of the emission peak, $\beta$ can be restricted to 0.85. The best fit results in $\dot{M} = 22 \cdot 10^{-6} M_\odot/yr$. (The lower limit for this star is constrained by $21 \cdot 10^{-6} M_\odot/yr$.)

*HD 303308.* No comment necessary.

*$\zeta$ Pup (HD 66811).* Figure 17c shows the influence of $\beta$ on the emission peak. Whereas even a $\beta = 1.0$ cannot fit the observations, with $\beta = 1.15$ (and the modified departure coefficients, see above) we obtain an almost perfect fit. Also obvious is that the emission in the high velocity wings is unaffected by the actual value of $\beta$, so that the mass-loss rate can be determined in any case.

*HD 15558.* No comment necessary (Fig. 17d).

*HD 15629.* No comment necessary.

*HD 193682.* No comment necessary.

*HD 14947.* $\beta = 1.0$ from shape of emission peak (Fig. 17e).

*$\lambda$ Cep (HD 210839).* With modified departure coefficients (both He and H, see above), we derive $\beta = 0.90$ and $\dot{M} = 5.3 \cdot 10^{-6} M_\odot/yr$.

*HD 190864* illustrates a typical example of the error introduced by the uncertainty in $\beta$. With our standard value (in this case $\beta = 0.80$), the profile can be fitted with $\dot{M} = 1.5 \cdot 10^{-6} M_\odot/yr$, whereas $\beta = 1.0$ – with a worse fit quality – yields $\dot{M} = 1.1 \cdot 10^{-6} M_\odot/yr$. In view of the better fit quality, the spectral type, "normal" terminal velocity and the results from UV line fits ($\beta_{UV} \approx 0.7$; Haser 1995), the lower $\beta$ seems to be more plausible.

*HD 217086.* In view of its almost vanishing wind-emission, we can derive only an upper limit of $\dot{M} \leq 0.2 \cdot 10^{-6} M_\odot/yr$ for this extremely rapid rotator ($v \sin i_{phot} = 375$ km/s), where the profile favours an "effective" rotational velocity of 290 km/s.

*HD 192639* has a P Cygni type like profile, which is difficult to fit with respect to its absorption part and the *blue* emission wing. However, due to the large wind emission also in the high velocity wings, the resulting error in $\dot{M}$ is only small. The inferred $\beta$ is 0.95.

*HD 193514.* No comment necessary.

*HD 203064.* "Effective" rotational speed 190 km/s ($v \sin i_{phot} = 315$ km/s).

*$\xi$ Per (HD 24912).* Compared to the large rotational speed of $\xi$ Per ($v \sin i_{phot} = 250$ km/s), the observed profile appears much too narrow. Reducing the effective value of $v_{rot}$ to 100 km/s, the fit quality becomes much better. $\xi$ Per is known as a notorious variable object with a suspected variability also *in the lowest wind region* (cf. Henrichs et al. 1994). Additionally, both the HeII 4686 line (cf. Herrero et al. 1992, Fig. 4) and the $H_\alpha$ complex show small emission peaks at the blue and red edge of the profile pointing to a disk like structure, so that the mass-loss rate derived here should be considered only to be an order of magnitude result.

*HD 13268.* As for HD 217086, also for this rapid rotator ($v \sin i_{phot} = 320$ km/s, "effective" value 250 km/s) only an upper limit of $\dot{M} \leq 0.05 \cdot 10^{-6} M_\odot/yr$ can be given (Fig. 17f).

*HD 191423.* The largest uncertainty for this star ($v \sin i_{phot} = 450$ km/s!, "effective" value 300 km/s) is due to its ill determined terminal velocity, which was here assumed as $v_\infty = 1150$ km/s (see Sect. 3.1.4). Due to the considerable wind emission, the resulting mass-loss rate can be regarded as significant and not only as an upper limit. Note, that also this profile points to a disk like structure because of the blue and red emission "bumps", which can be also expected from the large ratio $v_{rot}/v_\infty$ in terms of the wind compressed disk model (cf. Bjorkman & Cassinelli 1993).

*HD 207198.* No comment necessary.

*HD 210809.* Same comment as for HD 192639, $\beta = 0.93$.

*$\zeta$ Oph (HD 149757)* ($v \sin i_{phot} = 400$ km/s!, "effective value 300 km/s) is an extremely variable object and supposed non-radial pulsator (Vogt & Penrod 1983; Reid et al. 1993). From our $H_\alpha$ analysis, its mass loss rate can be restricted to $\dot{M} \leq 0.03 \cdot 10^{-6} M_\odot/yr$.

*HD 209975.* No comment necessary.

*HD 18409* poses the same dilemma as $\xi$ Per. To obtain a reasonable fit, the rotational speed ($v \sin i_{phot} = 160$ km/s) had to be lowered to an "effective" value of 80 km/s.

*$\alpha$ Cam (HD 30614)* This profile can be simulated by adapting both the H and HeII departure coefficients (see above) with $\beta = 1.1$ (Fig. 17g). One should note, however, that observations of this line by Ebbetts (1982; study of long term variability of O-star emission lines) showed a variability in the profile shape (also with respect to the position of the peak) up to a velocity of 600 km/s. Consequently, the apparent red shift of the emission peak ($\approx 100$ km/s with respect to rest wavelength) may be caused by a

highly structured wind which is also indicated by the extremely broad (and black) UV SiIV absorption troughs of this star (cf. Puls et al. 1995).

**LMC O-stars**

Most of the LMC/SMC $H_\alpha$ profiles are contaminated by weak night sky emission and water vapour absorption. We account for this, when performing the profile fit.

*Sk -67° 211.* We obtain $\dot{M} = 10 \cdot 10^{-6} M_\odot/yr$ with limits of $9.5..13 \cdot 10^{-6} M_\odot/yr$ (Fig. 17h).

*Sk -68° 137.* The red emission favours a value of $\dot{M} = 8 \cdot 10^{-6} M_\odot/yr$ with a lower limit of $7 \cdot 10^{-6} M_\odot/yr$.

*Melnick 42* can be fitted very well with $\beta = 0.55$ and $\dot{M} = 35 \cdot 10^{-6} M_\odot/yr$. The influence of different values of $\beta$ on the inner part of the profile is shown in Fig. 17i, where the upper curve corresponds to $\beta = 0.75$ and the lower one to the lowest possible value of $\beta = 0.5$ ("point star model", cf. Castor et al. 1975).

*Sk -67° 166.* The emission peak can be simulated with $\beta = 0.67$, and the mass-loss rate results to $\dot{M} = 13.0 \cdot 10^{-6} M_\odot/yr$ with only small errors.

*Sk -67° 167.* Spectroscopic twin of Sk -67° 166 (also in the UV), deduced values $\beta = 0.75$ and $\dot{M} = 14.0 \cdot 10^{-6} M_\odot/yr$. The reader may note that this star, although of lower luminosity, shows a slightly larger mass-loss rate than its counterpart above, which results from the different combinations of $R_*$ and $v_\infty$.

*Sk -66° 100* (with modified HeII departure coefficients) can be almost perfectly fitted with $1.9 \cdot 10^{-6} M_\odot/yr$ and a lower limit of $1.5 \cdot 10^{-6} M_\odot/yr$ (cf. Fig 17j).

**SMC O-stars**

*NGC 346#3.* No comment necessary (Fig. 17k).

*AV 388* was observed with EFOSC and the spectrum corrected for the nebula emission (cf. Sect. 3.1.1). For this star and all the following ones observed with EFOSC we convolved the theoretical profile with the instrumental profile of 3 Å(FWHM?) before comparing to the observed one. However, our simulation gives a dissatisfying fit quality, caused by the low quality spectrum. From the obtained equivalent width , the mass-loss rate can be roughly restricted to $\sim 0.2 \cdot 10^{-6} M_\odot/yr$.

*AV 243* (EFOSC) gives an upper limit of $\dot{M} \leq 0.1 \cdot 10^{-6} M_\odot/yr$, however with a better fit quality than above.

*NGC 346#1.* No comment necessary.

*NGC 346#4.* Only upper limit of $0.1 \cdot 10^{-6} M_\odot/yr$. Note that this value scales with the very uncertain $v_\infty$.

*NGC 346#6.* Only upper limit of $0.3 \cdot 10^{-6} M_\odot/yr$.

*AV 232 (Sk 80)* shows, among all stars of our sample, the weakest velocity gradient with $\beta = 1.40$ (Fig 17l). With a high fit quality, $\dot{M}$ results in $5.5 \cdot 10^{-6} M_\odot/yr$. Note, that for this star we had to reduce the hydrogen emissivity in the lower wind part.

*AV 238* (EFOSC) provides an estimate of $\dot{M} \sim 0.13 \cdot 10^{-6} M_\odot/yr$. This value scales however with the uncertain $v_\infty$.

### *3.3. Comparison with other investigations*

In Table 9 we compare our present results with the values used and derived by other authors for those stars which are in common. The majority of our galactic sample was also investigated by Leitherer (1988), where a subgroup of these stars has been reanalyzed by L&L. Only one of our galactic objects (HD 193514) is in common with the investigations by Scuderi et al. (1992). Finally, four of our LMC and three of our SMC stars have been also considered by Leitherer (1988a) but we note that there are serious discrepancies in his equivalent widths for the stars AV 243, AV 388, Sk -67°211 and Sk -68°137. For the first two stars Leitherer's values are approximately a factor of 2 smaller (in absorption) than the present values while for the last two stars he has a net emission in the $H_\alpha$ equivalent width compared with the net absorption found here. These differences are probably due to the lower S/N (approximately 20) and resolution (2.5 Å) of Leitherer's data coupled with an inadequate treatment of nebular emission. There is reasonably good agreement however for those stars which have a strong stellar emission component at $H_\alpha$ , namely the supergiants AV 232, Sk -67°166 and Sk -67°167.

In order to facilitate the comparison, Table 10 gives the quantities $\log\widetilde{Q}^2$ (cf. Eq. 51, $\dot{M}$ from the *equivalent width* of $H_\alpha$ ) and $\log(Q/v_\infty)$ ($\dot{M}$ from radio fluxes) which are independent of the stellar parameters used and reflect only the influence of the quantity which can be *actually* "measured".

With respect to the results by Leitherer and L&L, both investigations do not differ too much (L&L on the average find slightly larger $Q$ values), which is not astonishing since they used an almost identical procedure. Compared to our values, however, the differences are significant. Globally, we find larger values in the upper $Q$ range and lower ones in the lower range. This is clearly demonstrated in Fig. 18.

From this figure, it is obvious that the borderline between these two regimes (where both methods – i.e., ours and the one presented by Leitherer – give comparable results) lies roughly at $\log\widetilde{Q}^2 \approx -4.25$.

The reason for this systematic discrepancy is readily understood in terms of the results presented in Sect. 2, in particular the generalized curves of growth of Fig. 15. If we compare such a curve with the simple optically thin approximation of Eq. (13),

**Table 9. a** Comparison of present results with assumed and deduced O-star parameters from other investigations. $T_{\rm eff}$ in kK, $R_*$ in $R_\odot$, $v_\infty$ in km/s, $M_*$ in $M_\odot$, $L$ in $L_\odot$, $\dot{M}$ in $10^{-6}{\rm M}_\odot/{\rm yr}$. (L&R = Leitherer & Robert 1991)

| star | classif. | $T_{\rm eff}$ | log $g$ | $R_*$ | $v_\infty$ | log$L$ | $M_*$ | $\dot{M}$ | author |
|---|---|---|---|---|---|---|---|---|---|
| | | | | | Galaxy | | | | |
| HD 93129A | O3 I f* | 50.5 | 3.95 | 20. | 3250. | 6.37 | 130. | 22.0 | present paper |
| | | 47.5 | 3.75 | 25. | 3900. | 6.46 | 130. | 25.7 | Leitherer(1988) |
| | | 50.5 | 3.93 | 20. | 3050. | 6.35 | 125. | 13.2 | L&L, $H_\alpha$ |
| $\zeta$ Pup | O4 I(f) | 42.0 | 3.60 | 19. | 2250. | 6.00 | 52.5 | 5.9 | present paper |
| | | 44.8 | 3.75 | 17. | 2650. | 6.02 | 60. | 6.6 | Leitherer(1988) |
| | | | | | 2500. | | | 5.0 | L&R(1991) |
| | | 42.4 | 3.80 | 16. | 2200. | 5.90 | 59. | 3.55 | L&L, $H_\alpha$ |
| | | | | | | | | 2.4 | L&L, radio |
| HD 15558 | O5 III (f) | 48.0 | 3.85 | 21.8 | 2800. | 6.36 | 123. | 7.3 | present paper |
| | | 43.3 | 3.80 | 19. | 3000. | 6.06 | 85. | 3.9 | Leitherer(1988) |
| | | 42.3 | 3.70 | 19. | 3350. | 6.02 | 68. | 2.45 | L&L, $H_\alpha$ |
| HD 15629 | O5 V ((f)) | 47.0 | 3.90 | 14.2 | 3000. | 5.95 | 58.5 | 0.75 | present paper |
| | | 45.0 | 3.90 | 14. | 3250. | 5.86 | 60. | 1.86 | Leitherer(1988) |
| | | 44.3 | 3.90 | 13. | 2900. | 5.74 | 51. | 1.70 | L&L, $H_\alpha$ |
| HD 193682 | O5 III (f) | 45.0 | 3.65 | 12.2 | 2800. | 5.74 | 24. | 1.3 | present paper |
| | | 45.6 | 3.95 | 13. | 3100. | 5.82 | 55. | 2.63 | Leitherer(1988) |
| HD 14947 | O5 I f+ | 43.5 | 3.50 | 16.1 | 2350. | 5.93 | 30. | 7.5 | present paper |
| | | 40.6 | 3.75 | 18. | 2700. | 5.90 | 70. | 6.92 | Leitherer(1988) |
| | | 40.3 | 3.70. | 17. | 2300. | 5.86 | 52. | 4.79 | L&L, $H_\alpha$ |
| $\lambda$ Cep | O6 I(n)fp | 38.0 | 3.65 | 19. | 2250. | 5.83 | 59. | 5.3 | present paper |
| | | 39.5 | 3.65 | 19. | 2500. | 5.9 | 60. | 4.07 | Leitherer(1988) |
| | | 38.2 | 3.60 | 19. | 2100. | 5.86 | 52. | 3.5 | L&L, $H_\alpha$ |
| | | | | | | | | 2.1 | L&L, radio |
| HD 190864 | O6.5 III (f) | 41.0 | 3.55 | 14.1 | 2500. | 5.71 | 25.7 | 1.5 | present paper |
| | | 37.8 | 3.75 | 15. | 2950. | 5.62 | 45. | 1.41 | Leitherer(1988) |
| | | 39.2 | 3.75 | 14. | 2450. | 5.62 | 41 | 1.32 | L&L, $H_\alpha$ |
| HD 217086 | O7 V n | 40.0 | 3.75 | 10.3 | 2550. | 5.39 | 22. | $\leq$0.2 | present paper |
| | | 37.6 | 3.83 | 11. | 2300. | 5.34 | 30. | 0.62 | Leitherer(1988) |
| HD 192639 | O7 Ib (f) | 38.5 | 3.45 | 19.5 | 2150. | 5.88 | 39. | 6.0 | present paper |
| | | 35.9 | 3.53 | 20. | 2950. | 5.78 | 50. | 3.9 | Leitherer(1988) |
| HD 193514 | O7 Ib (f) | 38.0 | 3.45 | 19.8 | 2200. | 5.87 | 40. | 4.2 | present paper |
| | | 35.9 | 3.53 | 20. | 2950. | 5.78 | 50. | 2.82 | Leitherer(1988) |
| | | 35.7 | | 20. | 2950. | 5.77 | | 3.6 | Scuderi et al. (1992) |
| $\xi$ Per | O7.5 III (n)((f)) | 36.0 | 3.40 | 25.5 | 2450. | 6.0 | 60. | 3.2 | present paper |
| | | 36.0 | 3.80 | 12. | 2500. | 5.34 | 35. | 0.87 | Leitherer(1988) |
| | | 37.1 | 3.77 | 12. | 2400. | 5.38 | 31. | 1.29 | L&L, $H_\alpha$ |
| HD 13268 | ON8 V | 35.0 | 3.50 | 11.7 | 2150. | 5.27 | 16. | $\leq$0.05 | present paper |
| | | 38.5 | 3.90 | 11. | 2300. | 5.38 | 35. | 0.72 | Leitherer(1988) |
| HD 191423 | O9 III : n* | 34.0 | 3.70 | 13. | 1150. | 5.31 | 31. | 0.20 | present paper |
| | | 30.0 | 3.60 | 13. | 2550. | 5.10 | 25. | 0.22 | Leitherer(1988) |
| HD 207198 | O9 Ib-II | 34.0 | 3.30 | 15.1 | 2150. | 5.44 | 16.6 | 1.6 | present paper |
| | | 33.0 | 3.55 | 15. | 2650. | 5.38 | 30. | 0.74 | Leitherer(1988) |
| $\zeta$ Oph | O9 III | 32.5 | 3.85 | 12.9 | 1550. | 5.22 | 43. | $\leq$0.03 | present paper |
| | | 35.9 | 4.0 | 8. | 1500. | 5.00 | 24. | 0.039 | L&L, radio |
| HD 209975 | O9.5 Ib | 32.5 | 3.20 | 17.2 | 2050. | 5.47 | 17. | 0.9 | present paper |
| | | 28.7 | 3.30 | 18. | 2300. | 5.30 | 25. | 0.42 | Leitherer(1988) |
| $\alpha$ Cam | O9.5 Ia | 30.0 | 3.00 | 29. | 1550. | 5.79 | 30.7 | 5.2 | present paper |
| | | 28.7 | 3.15 | 30. | 1750. | 5.74 | 45. | 2.19 | Leitherer(1988) |
| | | 30.9 | 3.20 | 27. | 1550. | 5.78 | 43. | 3.39 | L&L, $H_\alpha$ |
| | | | | | | | | 3.9 | L&L, radio |

**Table 9. b** As **a**, but for Magellanic Clouds stars

| star | classif. | $T_{\rm eff}$ | $\log g$ | $R_*$ | $v_\infty$ | $\log L$ | $M_*$ | $\dot{M}$ | author |
|---|---|---|---|---|---|---|---|---|---|
| | | | | | LMC | | | | |
| Sk −67° 211 | O3 III (f*) | 60.0 | 4.15 | 17.8 | 3750. | 6.57 | 163. | 10. | present paper |
| | | 50.0 | 3.8 | 17. | 3100. | 6.22 | 70. | 5.75 | Leitherer(1988a) |
| Sk −68° 137 | O3 III (f*) | 60.0 | 4.10 | 12.4 | 3400. | 6.26 | 70.6 | 8. | present paper |
| | | 50.0 | 3.8 | 16.2 | 3100. | 6.18 | 65. | 4.6 | Leitherer(1988a) |
| Sk −67° 166 | O4 I f$^+$ | 47.5 | 3.65 | 19.5 | 1900. | 6.24 | 62. | 13.0 | present paper |
| | | 44.1 | 3.8 | 19. | 2100. | 6.10 | 75. | 4.2 | Leitherer(1988a) |
| Sk −67° 167 | O4 Inf$^+$ | 47.5 | 3.65 | 17.9 | 2150. | 6.17 | 52.8 | 14.0 | present |
| | | 44.1 | 3.7 | 20. | 2100 | 6.14 | 80. | 4.5 | Leitherer(1988a) |
| | | | | | SMC | | | | |
| AV 388 | O4 V | 48.0 | 3.70 | 10.7 | 2100. | 5.74 | 21. | ∼0.17 | present paper |
| | | 48.0 | 4.1 | 11.2 | 2600. | 5.78 | 60 | 1.07 | Leitherer(1988a) |
| AV 243 | O6 V | 45.0 | 3.70 | 12.3 | 2050. | 5.75 | 23. | ≤0.1 | present paper |
| | | 39.5 | 3.7 | 13.2 | 2400. | 5.58 | 35 | 0.51 | Leitherer(1988a) |
| AV 232 | O7 Iaf$^+$ | 37.5 | 3.30 | 29.3 | 1400. | 6.19 | 62.5 | 5.5 | present paper |
| | | 37.5 | 3.30 | 26.3 | 1600. | 6.10 | 55. | 6.2 | Leitherer(1988a) |

**Table 10.** $\log\widetilde{Q}^2$ and $\log(Q/v_\infty)$ derived from the results by Leitherer (1988, 1988a) and L&L in comparison with our values (see text). Reference temperature $T_{\rm ref}$ = 40,000 K (cf. Eq. 50, $\dot{M}$ in $10^{-6}$M$_\odot$/yr, $v_\infty$ in 1000 km/s and $R_*$ in $R_\odot$

| star | classif. | $\log\widetilde{Q}^2$ | | | $\log(Q/v_\infty)$ | |
|---|---|---|---|---|---|---|
| | | present paper | Leitherer (1988(a)) | L&L(H$_\alpha$) | present paper | L&L(radio) |
| | | | | Galaxy | | |
| HD 93129A | O3 I f* | -2.41 | -2.61 | -2.81 | | |
| ζ Pup | O4 I (f) | -2.95 | -2.93 | -3.17 | -1.50 | -1.77 |
| HD 15558 | O5 III (f) | -3.30 | -3.57 | -4.02 | | |
| HD 15629 | O5 V ((f)) | -4.74 | -3.93 | -3.80 | | |
| HD 193682 | O5 III (f) | -3.95 | -3.52 | | | |
| HD 14947 | O5 I f$^+$ | -2.61 | -2.83 | -2.94 | -1.33 | <-0.97 |
| λ Cep | O6 I(n)fp | -2.90 | -3.26 | -3.22 | -1.55 | -1.92 |
| HD 190864 | O6.5 III (f) | -3.80 | -3.93 | -3.82 | | |
| HD 217086 | O7 V n | ≤-5.11 | -4.04 | | | |
| HD 192639 | O7 Ib (f) | -2.81 | -3.34 | | | |
| HD 193514 | O7 Ib (f) | -3.14 | -3.62 | | | |
| ξ Per | O7.5 III (n)((f)) | -3.70 | -3.86 | -3.53 | | |
| HD 13268 | O7 | ≤-6.15 | -3.95 | | | |
| HD 191423 | O9 III : n* | -4.59 | -4.88 | | | |
| HD 207198 | O9 Ib-II | -3.43 | -4.20 | | | |
| ζ Oph | O9 III | ≤-6.37 | | | ≤-3.38 | -2.93 |
| HD 209975 | O9.5 Ib | -3.99 | -4.59 | | | |
| α Cam | O9.5 Ia | -2.82 | -3.63 | -3.14 | -1.67 | -1.74 |
| | | | | LMC | | |
| Sk −67° 211 | O3 III (f*) | -3.29 | -3.31 | | | |
| Sk −68° 137 | O3 III (f*) | -2.94 | -3.44 | | | |
| Sk −67° 166 | O4 I f$^+$ | -2.36 | -3.27 | | | |
| Sk −67° 167 | O4 Inf$^+$ | -2.27 | -3.28 | | | |
| | | | | SMC | | |
| AV 388 | O4 V | -5.43 | -4.05 | | | |
| AV 243 | O6 III | ≤-5.96 | -4.56 | | | |
| AV 232 | O7 Iaf$^+$ | -3.06 | -2.92 | | | |

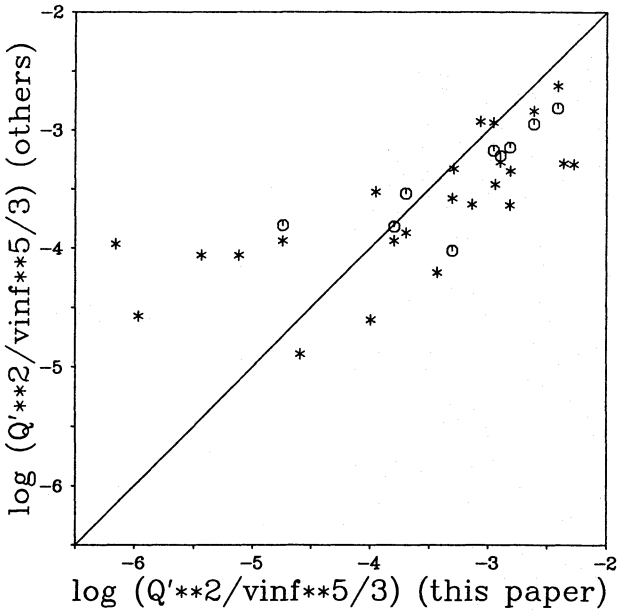


**Fig. 18.** Comparison of our values for $\log\widetilde{Q}^2$ (cf. Table 10) with the results by Leitherer (1988, 1988a; asterisks) and L&L (circles)

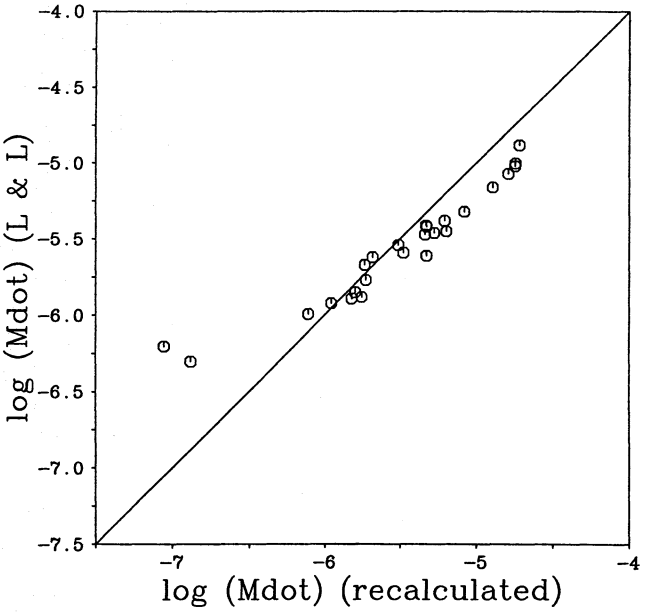


**Fig. 20.** Comparison of $H_\alpha$ mass-loss rates from L&L and our curve of growth method, using their stellar parameters and equivalent widths (column 2 and 3 of Table 11)

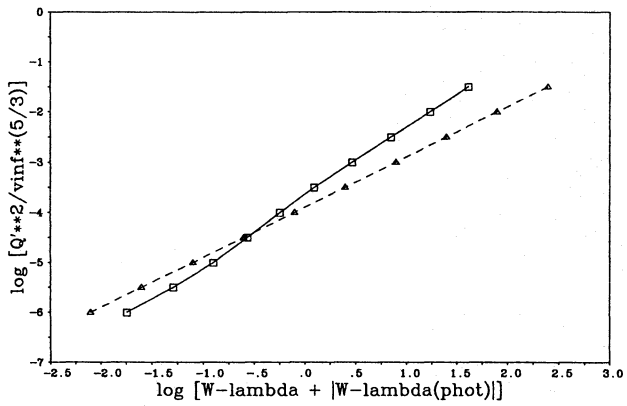


**Fig. 19.** $H_\alpha$ curve of growth as in Fig. 15. Solid: $\beta = 0.7$ and $v_\infty =$ 2000 km/s. Dashed: The L&L approach of Eq. (13) for $\beta = 0.7$, $v_\infty =$ 2000 km/s and $v_{\min}/v_\infty = 0.01$, as it has been applied in their paper

as it was used by L&L, we find that the latter tends to overestimate $\dot{M}$ for low values of the net equivalent width (see Fig. 19, but also A. Gabler et al. (1990) and their Fig. 3). For large values of $\log W'_\lambda$, the mass-loss rate is underestimated.

The physical reasons behind this are firstly that the Sobolev approximation fails for very low values of $\dot{M}$, as the wind contribution to $H_\alpha$ then comes from regions around the sonic point. Secondly, for large values of $\dot{M}$ the optically thin approximation *applied throughout the wind* fails and leads to a different scaling of wind emission with mass-loss rate, since a large part of the wind envelope is optically thick.

Another important test of the $H_\alpha$ -method is the comparison with mass-loss rates derived from radio fluxes. This test was carried out already by Leitherer (1988) and L&L, but needs to be repeated here because of the systematic differences between their and our $H_\alpha$ -method. Unfortunately, contrary to the L&L sample, only for a very few of our targets (four objects) have radio fluxes been published. Thus, to carry out this important test we proceed as follows. We use the measured $H_\alpha$ equivalent widths and stellar parameters from L&L for all those objects that have published radio fluxes. With these data we derive $H_\alpha$ mass-loss rates by means of our curve of growth method and then compare with mass-loss rates obtained from radio fluxes. The details are given in Table 11, where for the results of column 3 we adopted our "standard values" of $\beta$ (cf. Sect. 3.2.1). The values of column 4 are calculated with those $\beta$-values which could be actually measured by our profile fits (superscript [2], cf. Table 8), whereas for the supergiants in the L&L sample which are not present in ours we adopted $\beta = 1$ as an average value in accordance with our findings from Sect. 3.2.2 (superscript [3]).

Figure 20 compares the $\dot{M}$-values obtained with our method with the L&L-values based on their equivalent widths and stellar parameters. The same trend as in Fig. 18 is found. Figure 21 then compares radio with $H_\alpha$ mass-loss rates. If we exclude for the moment HD 15570, then the L&L and our values show a similar degree of consistency. For the mean value of $\langle \log\dot{M}(H_\alpha) - \log\dot{M}(\text{radio})\rangle$ we obtain $0.07 \pm 0.21$ for our values, contrasted to $0.02 \pm 0.23$ when the mass-loss rates given by L&L are used.

For HD 15570 our $\dot{M}$-value is significantly larger than the radio mass-loss rate. Note, however, that for this star only the 3.6 cm flux could be measured (for 2 cm and 6 cm only upper limits are given) and it was classified as a "probable" but *not* definite thermal emitter; note further, that this star is an O4 If$^+$ supergiant, which from our experience most probable has a very flat velocity field, which would lower the mass-loss rate addi-

**Table 11.** Comparison of mass-loss rates from different methods for the sample of L&L. Stellar parameters from L&L (their Table 1), mass-loss in units $M_\odot/yr$ (see text)

| HD/ star | log$\dot{M}$ L&L ($H_\alpha$) | log$\dot{M}$ $H_\alpha$ [1)] | log$\dot{M}$ $H_\alpha$ | log$\dot{M}$ L&L (radio) |
|---|---|---|---|---|
| 14947 | -5.32 | -5.07 | -5.14[2)] | <-4.76 |
| 15558 | -5.61 | -5.32 | | |
| 15570 | -5.02 | -4.74 | -4.81[3)] | -5.33 |
| 15629 | -5.77 | -5.72 | | |
| $\xi$ Per | -5.89 | -5.81 | | |
| $\alpha$ Cam | -5.47 | -5.34 | -5.50[2)] | -5.41 |
| $\delta$ Ori | -5.92 | -5.95 | | -5.97 |
| $\lambda$ Ori | -6.20 | -7.05 | | <-6.04 |
| $\iota$ Ori | -5.99 | -6.11 | | -6.50 |
| $\epsilon$ Ori | -5.59 | -5.48 | | -5.39 |
| $\zeta$ Ori | -5.41 | -5.33 | -5.44[3)] | -5.60 |
| 46150 | <-5.88 | <-8.00 | | |
| 46223 | -5.85 | -5.80 | | |
| 15 Mon | -6.30 | -6.88 | | |
| 57061 | -5.54 | -5.51 | | -5.20 |
| $\zeta$ Pup | -5.45 | -5.20 | -5.30[2)] | -5.62 |
| 93129A | -4.88 | -4.72 | -4.75[2)] | |
| $\mu$ Nor | -5.67 | -5.73 | | <-5.36 |
| 151804 | -5.00 | -4.74 | -4.80[3)] | -5.00 |
| 152408 | -5.07 | -4.79 | -4.83[3)] | -4.87 |
| 152424 | -5.42 | -5.37 | -5.44[3)] | -5.26 |
| 9 Sgr | -5.62 | -5.68 | | |
| 9 Sge | -5.38 | -5.21 | -5.29[3)] | |
| 190429A | -5.16 | -4.89 | -4.96[3)] | |
| 190864 | -5.88 | -5.75 | | |
| $\lambda$ Cep | -5.28 | -5.26 | -5.35[2)] | -5.68 |

[1] from L&L's equivalent width with "standard values" for $\beta$.
[2] from L&L's equivalent width with derived $\beta$-values (cf. Table 8).
[3] from L&L's equivalent width with $\beta = 1$ adopted

tionally if compared to the assumed $\beta = 0.75/1.0$ parameter. (For $\beta = 1.3$ we would obtain $\log\dot{M} \approx -4.95$ more consistent with the radio rate)

Summarizing the results of this section, we have shown that the assumption of an optically thin emission troughout the wind and the neglect of the finite profile width in Leitherer's method are mostly responsible for the differences in our results and those by L&L. In conclusion, we feel that our method of detailed modelling of the profile is superior to all other approaches since, especially for emission lines, the most decisive parameter – $\beta$ – can be derived simultaneously and any correction for nebula emission lines can be carried out more easily.

## 4. Observed and theoretical wind momentum

In the following section, we want to investigate to what extent the observed stellar wind quantities are consistent with the predictions of radiative driven wind theory. In particular, we will reexamine the "momentum" problem pointed out by L&L for winds with a high density.

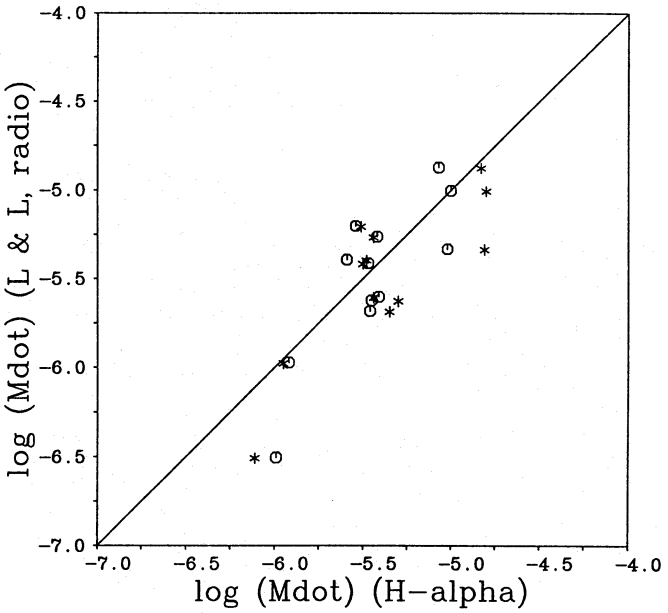


**Fig. 21.** Comparison of $H_\alpha$ vs. radio mass-loss rates. Circles: $H_\alpha$ mass loss rates from L&L; asterisks: $H_\alpha$ mass-loss rates from our curve of growth method (column 4 (or 3) of Table 11)

### *4.1. The "wind momentum-luminosity relation" – Theoretical prediction vs. observations*

In order to examine how far the observed winds follow the *principal* predictions of radiative driven wind theory, one has to consider which crucial quantities can be checked with as little as possible contamination by uncertain parameters. With respect to an *individual* investigation of mass-loss rates and terminal velocities, this is a difficult task due to the *strong* dependence of both quantities on stellar mass which may be considered as erroneous, depending whether one prefers the "spectroscopic" or "evolutionary" masses (cf. Herrero et al. 1992 and L&L for the controversial discussion in this field). In this paper, we will therefore consider a different quantity, which we will prove to be only marginally dependent on the stellar mass and in this way provides an ideal tool to investigate the consistency of reality and theory.

First, we recall the individual scaling laws for radiation driven winds. If the radiative line force is given in terms of the usual "force-multiplier" parameters $k$, $\alpha$, $\delta$ (Abbott 1982; Pauldrach et al. 1986), then, according to the complete analytical description by Kudritzki et al. (1989, especially their Eq. (47) or (61)), the mass-loss rate obeys the following scaling law

$$\dot{M}_{\rm theory} \sim k^{\frac{1}{\alpha'}} L^{\frac{1}{\alpha'}} \left(M(1-\Gamma)/D'\right)^{1-\frac{1}{\alpha'}} \left(\frac{g_{\rm eff}}{R_*}\right)^{\frac{\delta}{2\alpha'}}, \qquad (54)$$

with $\alpha' = \alpha - \delta$, $\Gamma = L_{\rm E}/L$ ($L_{\rm E}$ the Eddington luminosity), $D' = (1+I_{\rm He}Y)/(1+4Y)$ and $g_{\rm eff}$ the gravitational acceleration, corrected by $(1-\Gamma)$.

For the terminal velocity, we have

$$v_\infty^{\rm theory} = \left(\frac{\alpha}{1-\alpha}\right)^{\frac{1}{2}} I(\alpha,\beta,\delta)^{\frac{1}{2}} v_{\rm esc}$$
$$\approx 2.24\,\frac{\alpha}{1-\alpha}\,v_{\rm esc} \qquad (55)$$

with $v_{\rm esc} = (g_{\rm eff} R_*)^{\frac{1}{2}}$ the photospheric escape velocity and $I(\alpha,\beta,\delta)$ as defined by Eq. (46) in Kudritzki et al. (1989), where the latter approximation ($I \approx 5\alpha/(1-\alpha)$) holds roughly for values of $\delta \lesssim 0.1$ (cf. Kudritzki et al. 1989, Figs. 4 and 6, Table 1 and Friend & Abbott 1986) and a typical velocity law with $\beta = 0.7...1.3$.

Hence, for typical values of $\alpha = 0.5...0.7$ and $\delta = 0.02...0.1$ the mass-loss rate should depend strongly on the "effective mass" via $(M(1-\Gamma)/D')^{-1.5...-0.5}$, whereas $v_\infty$ should scale with $(M(1-\Gamma))^{0.5}$. For the wind momentum rate, however, we find a much weaker dependence on the effective mass,

$$(\dot{M} v_\infty)_{\rm theory} \sim k^{\frac{1}{\alpha'}} L^{\frac{1}{\alpha'}} (M(1-\Gamma))^{\frac{3}{2}-\frac{1}{\alpha'}} \times$$
$$\times\, R_*^{-\frac{1}{2}} \left(\frac{g_{\rm eff}}{R_*}\right)^{\frac{\delta}{2\alpha'}} D'^{\frac{1}{\alpha'}-1} \qquad (56)$$

since the combined exponent $(3/2 - 1/\alpha')$ is much closer to zero than the individual ones. Hence, from radiation driven wind theory we expect the following relation to hold

$$\log(\dot{M} v_\infty R_*^{\frac{1}{2}} D') = x \log(kLD') + f(M,\Gamma,R_*,\alpha,\delta)$$
$$x = 1/\alpha', \qquad (57)$$

where $f$ is an only mildly varying function of stellar and force-multiplier parameters, namely

$$f = \Delta \log(M(1-\Gamma)) + (\delta/2\alpha') \log(g_{\rm eff}/R_*) + h(\alpha,\delta)$$
$$\Delta = \frac{3}{2} - \frac{1}{\alpha'}. \qquad (58)$$

$h$ is a function of $\alpha$ and $\delta$ only and the correction for $g_{\rm eff}/R_*$ in the latter expression for $f$ is small because of $\delta/2\alpha' \ll 1$.

From Eq. (57) (and with $D'$ = const ) we would expect a strict correlation of $\log(\dot{M} v_\infty R_*^{0.5})$ with $\log L$, where the slope of this relation is predicted to yield an average value of $1/\alpha'$, at least if the flux-weighted number of driving lines (which is just the physical interpretation of $k$) is not too different for different spectral types.

Indeed, this so-called "wind momentum-luminosity relation" was *empirically* found by Kudritzki et al. (1995), who demonstrated the observational evidence of this correlation using a large sample of galactic O/B/A LC I-III stars, i.e., for stars *covering an extremely large range in spectral and luminosity type*. The significance of this relation for providing a tool for extragalactic distance measurements was emphasized in the above paper, while a thorough discussion (especially with respect to metallicity and wind density) will be given in a forthcoming publication.

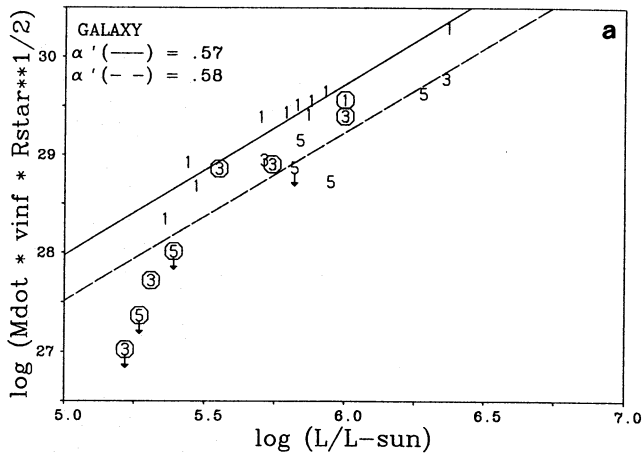


**Fig. 22. a** The observed wind momentum-luminosity-relation for galactic O-stars (Table 8). (Wind momentum rate $\dot{M} v_\infty$ in cgs-units, $R_*$ in units of $R_\odot$.) Each object is plotted by a number giving its luminosity class. Two regression curves for luminosity class I (solid) and higher luminosity classes (dashed) are given. Note that for the latter the objects with $\log L/L_\odot < 5.3$ are excluded. Rapid rotators with $v \sin i \geq 200$ km/s are marked with a circle, and objects with only an upper limit for $\dot{M}$ are indicated by an arrow

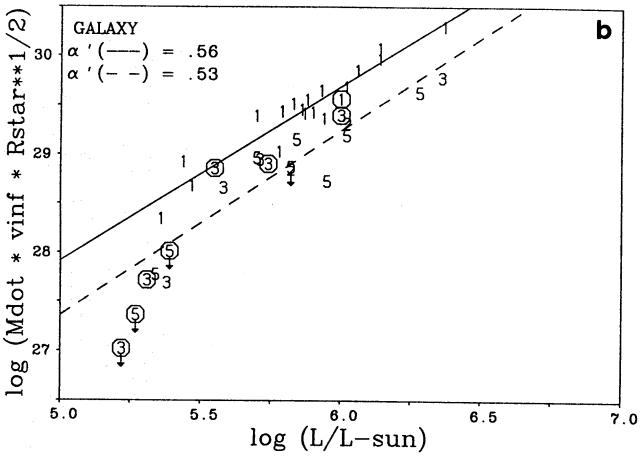


**Fig. 22. b** As **a** but including additionally the complementary objects of Table 11

In Fig. 22 we have plotted the observed wind momentum-luminosity relation for galactic O-stars (neglecting the $D'$-term which is only of minor influence). Figure 22a contains our sample only (Table 8), whereas in Fig. 22b we have enlarged the data base with those objects of Table 11 which do not overlap with our sample. Both figures show the same trend. Supergiants follow a very tight relation with a slope corresponding to $\alpha' = 0.56$. The objects of luminosity classes II, III and V show a somewhat less tight relation with 0.5 dex smaller "momentum" and an almost parallel slope ($\alpha' = 0.53$) until luminosities $\log L/L_\odot = 5.3$. Below this value the relation turns off and seems to become much steeper. We note that for these stars the

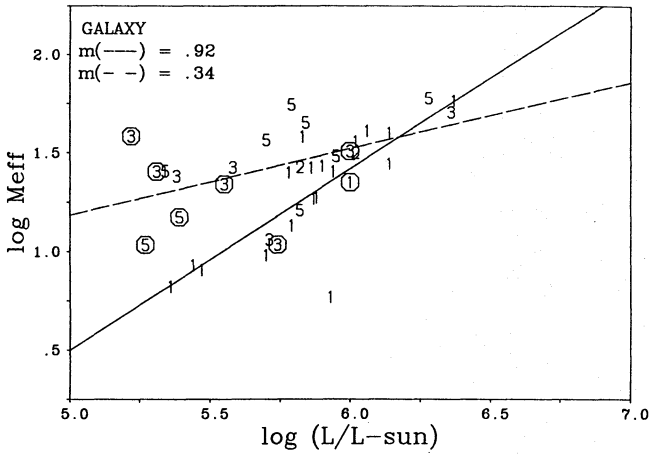


**Fig. 23.** Logarithm of "effective mass" $M(1-\Gamma)$ as function of luminosity for the objects of Fig. 22b. The regression curves with slope $m$ are plotted as guide lines

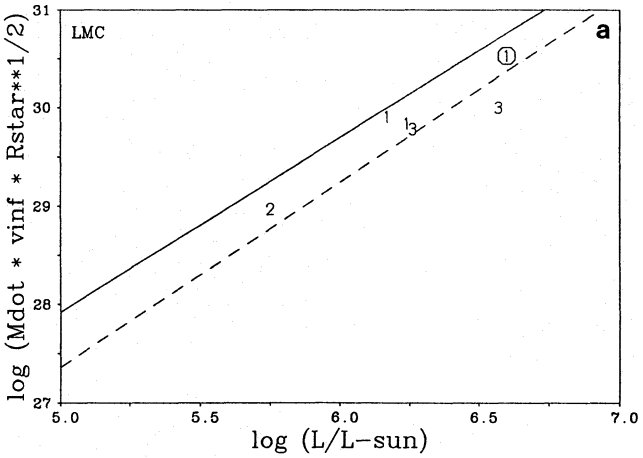


**Fig. 24. a** The observed wind momentum-luminosity-relation for LMC O-stars (Table 8). For orientation, the regression curves for galactic O-stars (Fig. 22b) are also shown

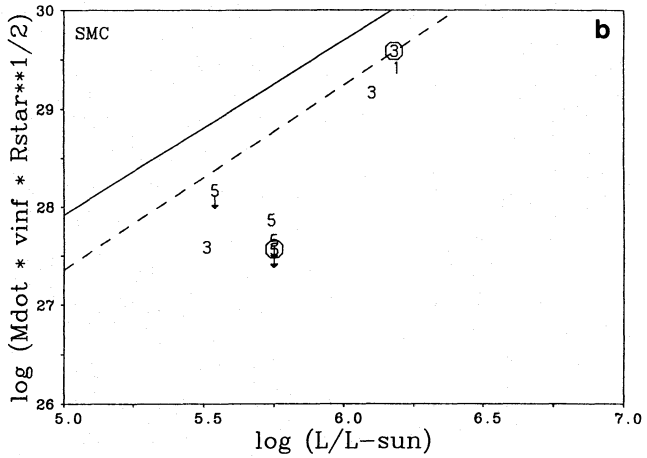


**Fig. 24. b** As **a** but for SMC O-stars

winds have an extremely low density and optical thickness and that, therefore, their wind properties are affected by additional important effects part of which have already been identified (see, for instance, Springmann & Pauldrach 1992). Note also that most of these stars are rapid rotators ($v \sin i \geq 200$ km/s), as is the only luminosity class III object which lies *well* above the mean relation (HD 203064 with $v \sin i = 315$ km/s).

The shift between supergiants and other luminosity classes for $\log L/L_\odot \geq 5.3$ could have two explanations. Either the number of flux weighted driving lines (proportional to $k$) or the "effective" masses are smaller. In the latter case (since $\Delta = -0.31$ for a mean $\alpha' = 0.55$), this requires $M(1-\Gamma)$-values roughly a factor of twenty smaller. From Fig. 23 we conclude that the difference in the effective mass is not sufficient and that an additional influence of $k$ is required. However, we note also that the average mass correction for lower luminosities is much larger than for higher luminosities, so that at least a certain part of the differences in the wind momentum-luminosity-relation for lower luminosities and higher luminosity classes may be compensated.

Figure 24 show the wind momentum-luminosity relations for the LMC and SMC O-stars of Table 8. Since the number of Magellanic Cloud objects studied so far is small, the comparison with the Galaxy is still marginal. We infer a small shift of approximately 0.20 dex and a parallel slope for the LMC supergiants. This can be explained by the dependence of the number of driving lines or force-multiplier parameter $k$ on metal abundance $\epsilon$ (Castor et al. 1975; Abbott 1982; Kudritzki et al. 1987) yielding

$$k(\epsilon) = k(\epsilon_\odot)\left(\frac{\epsilon}{\epsilon_\odot}\right)^{1-\alpha} \quad \rightarrow \quad \dot{M}(\epsilon) \sim \left(\frac{\epsilon}{\epsilon_\odot}\right)^{\frac{1-\alpha}{\alpha'}}. \qquad (59)$$

With $\alpha' = 0.56$ (and $\delta = 0.07$) this would give an abundance difference of 0.3 dex between the Galaxy and the LMC in good agreement with the first results of the quantitative abundance analysis of the HST spectra presently under way in our group (see Kudritzki et al. 1992a).

For the SMC, the difference to the Galaxy is more striking. Adopting $\alpha' = 0.52$ (as most of our objects belong to luminosity classes III and V) and again $\delta = 0.07$, we find an average momentum shift of 0.66 dex corresponding to $\Delta\log\epsilon = -.83$ again in good agreement with our ongoing abundance work. However, the data points between $\log L/L_\odot = 5.5$ and 5.8 might also indicate a steeper slope (and therefore a smaller $\alpha'$) or a similar turnover of the relation as for galactic giants and main sequence stars. In the latter case it would be reasonable to expect this to occur at higher luminosities in the SMC because of smaller metallicity and consequently smaller wind density at a given luminosity.

That the value of $\alpha'$ is perhaps an increasing function of metallicity may be due to the possibility that the line-strength distribution function (cf. Kudritzki et al. 1988) is not perfectly linear in the $\log N(k_L < k_L^{max})$ vs. $\log k_L$ relation (with $N$ the number of lines and $k_L$ the corresponding line strength), but has

a steeper (negative) slope towards the high line-strength end of this relation. This trend can indeed be observed in the line strength distribution function given by Puls (1987, Fig. 4) and is also present in our latest simulations using the updated atomic data. (A detailed discussion and the reason for this behaviour will be given in a forthcoming paper.) Thus, for lower metallicities with a smaller range of contributing line-strengthes, this steeper slope (proportional to $(\alpha - 1)$) would have a larger influence on the average $\alpha$, which then would tend to lower values.

In any case, to investigate the question which of the above two possibilities is actually present, we will need a significantly larger sample of stars.

### 4.2. *A comparison with detailed radiation driven wind computations*

To compare with the predictions of radiation driven wind theory we have calculated wind models for every object of Table 8. We have adopted solar metal abundances for all galactic objects. For the LMC and the SMC we have adopted 0.6 solar and 0.2 solar (Haser et al. 1994a; Haser 1995). For the additional galactic objects of Table 11 that were included in Fig. 22b we used the calculations for Table 8 plus an already existing grid of computations to interpolate force multiplier parameters $k$, $\alpha$, $\delta$ as function of temperature and average wind density to the corresponding stellar parameters and calculated wind properties with the analytical approach by Kudritzki et al. (1989).

The underlying physics of the computations are described in detail by Pauldrach et al. (1994). These computations are clearly superior to older ones performed in our group (Pauldrach et al. 1990), the most important difference being a significantly larger number of lines included with much better atomic physics, and much better and more extended atomic models in the detailed NLTE approach.

In our discussion of the reliability of the theory we will concentrate on the wind momentum rate only. A discussion of $\dot{M}$ and $v_\infty$ individually instead would be complicated by the fact that both systematic errors in wind theory and in the stellar parameters derived by spectroscopy would have to be disentangled, whereas the momentum should depend mainly on luminosity only (cf. the discussion in Sect. 4.1).

We will proceed in two steps. First we will investigate possible defects of the theory as function of luminosity and temperature. Secondly, we will re-investigate the differential behaviour of theory and observation as function of wind performance number $\eta = \dot{M} v_\infty c/L$ to check whether the important result by L&L that the theory fails as function of $\eta$ is still valid.

#### 4.2.1. Wind momentum and luminosity

Figure 25 shows the theoretical wind momentum rate as function of luminosity for all galactic objects of Fig. 22b. The comparison with the regression curves of the observed momentum reveals that, while the slope agrees with the observations, there is an obvious discrepancy for the supergiants as the theoretically predicted momentum is about 0.25 dex too small. This is

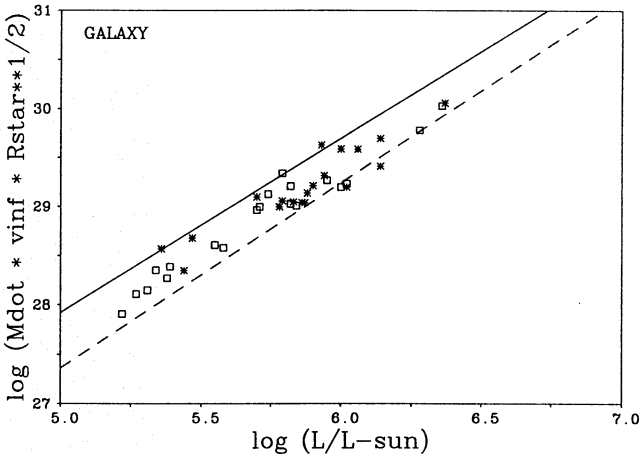


**Fig. 25.** Theoretical wind momentum as function of luminosity for all galactic objects of Fig. 22b. Asteriks: Luminosity class I, squares: II,III, V. The two regression curves from the observed data of Fig. 22b are also shown

somewhat better quantified in Fig. 26a, which gives the difference between observed and calculated logarithmic momentum for supergiants. We do *not* see any clear trend of the discrepancy with either luminosity or effective temperature.

For luminosity classes II, III and V there appears to be better statistical agreement between theory and observation, if we exclude objects with $\log L/L_\odot < 5.3$ for the reasons indicated in Sect. 4.1. Additionally, we see also from Fig. 26b that there is no *obvious* systematic difference as function of temperature, if we divide our objects in two classes with $T_{\rm eff}$ below and above 40,000 K. We obtain $-0.08 \pm 0.32$ and $-0.23 \pm 0.22$ for the average (l.c. II to V) difference in logarithmic momentum, respectively. On the other hand, for luminosity class I objects the statistics yield $+0.29 \pm 0.24$ and $+0.17 \pm 0.17$, correspondingly.

We conclude that the theory very likely has systematic uncertainties of the order 0.25 dex, if the wind momentum is studied as function of luminosity, temperature and luminosity classes.

#### 4.2.2. Wind momentum and performance number

After the important analysis by L&L it is imperative to check whether another systematic discrepancy between theory and observation is hidden in the data presented in Figs. 25 and 26. L&L detected a dependence on $\eta = \dot{M} v_\infty c/L$, the wind performance number which compares the stellar wind momentum flux with the photon momentum flux. Figure 27 essentially repeats their results and demonstrates that there is a clear trend with $\eta$, if the L&L method is used to determine mass-loss rates from $H_\alpha$ and the "older" wind theory (essentially Pauldrach et al. 1990, but see L&L) is applied.

The first question is what happens to Fig. 27 if the improved wind theory (Pauldrach et al. 1994, see also Sect. 4.2.1) is applied and again the differences to observations using the L&L method are plotted. This is done in Fig. 28 and we see that, if we ignore the one object in the lower left (HD 15558, see also

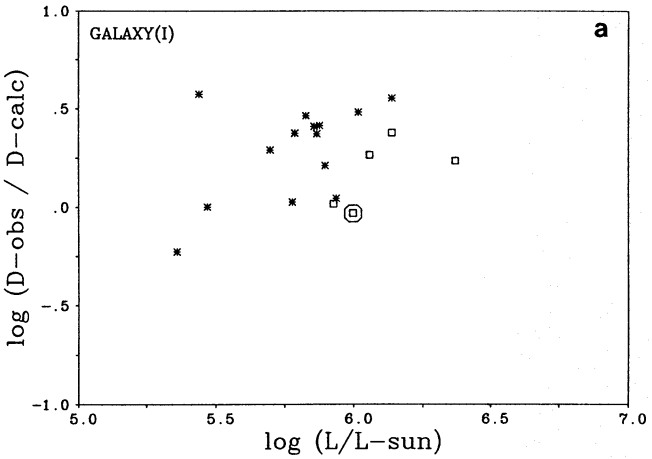


**Fig. 26. a** Difference between observed and calculated logarithmic momentum rate ($D = \dot{M}v_\infty$) of galactic O-supergiants as function of luminosity. Asteriks and squares correspond to effective temperatures below and above 40,000 K, respectively

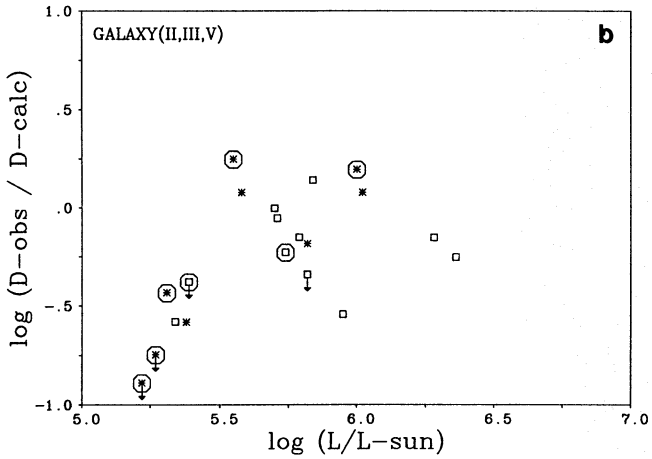


**Fig. 26. b** As **a**, but for luminosity classes II, III, V

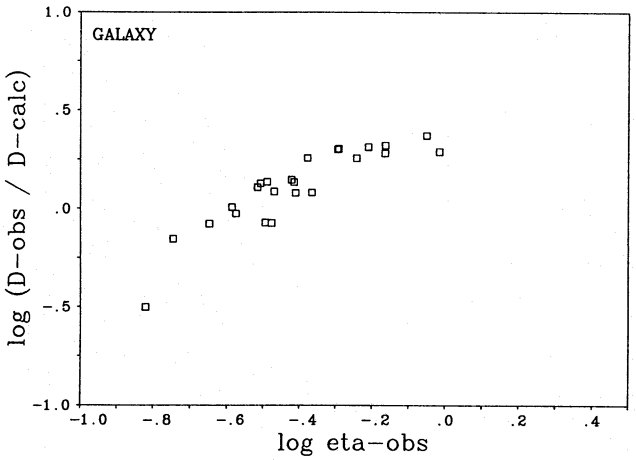


**Fig. 27.** Difference between observed logarithmic wind momentum rate determined using the method by L&L and predictions by the older theoretical approach (Pauldrach et al. 1990, force multiplier parameters as in L&L) as function of logarithmic wind performance number. Note that the result obtained in this plot is essentially identical with that by L&L, the only difference being that we have used our stellar parameters and $v_\infty$ (Table 8) for their objects overlapping with our sample

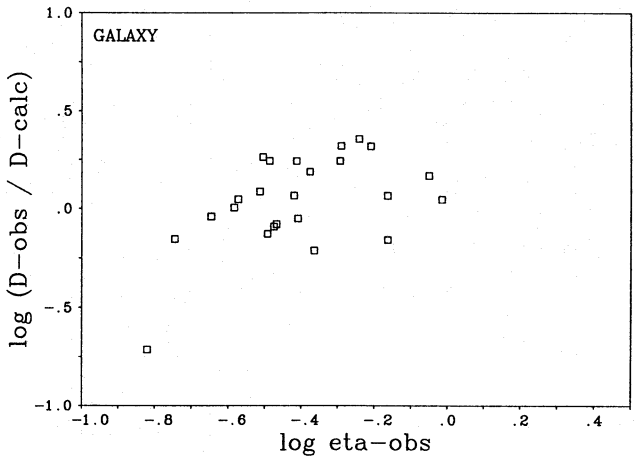


**Fig. 28.** As Fig. 27 but now with new stellar wind calculations using the recent improvements of radiation driven wind theory as described by Pauldrach et al. (1994)

the discussion in Sect. 3.7), then the effect has almost disappeared and that observations and theory agree independent of $\eta$ to an average of $+0.08 \pm 0.17$ in the logarithmic momentum difference.

*If we would, therefore, stay with the determination of mass-loss rates from $H_\alpha$ using the simple optically thin pure emission approach by L&L, then the straightforward conclusion would be that the improved wind theory is in excellent agreement with observation.*

Unfortunately, we cannot maintain this conclusion as soon as we use the results of our improved $H_\alpha$ -diagnostics. The reason is that the simplified L&L approach leads to an underestimate at high $\dot{M}$ and yields overestimates at small $\dot{M}$, as we have explained in the previous sections. In consequence, mass-loss rates will be higher at large $\eta$ and smaller at small $\eta$, if the improved diagnostics are applied. This result, deplorable for the theory, is shown in Fig. 29, which again reveals a clear trend with $\eta$ which however is now not identical for effective temperatures below and above 40,000 K. This trend remains significant, even if de do not include the objects with $\log L/L_\odot < 5.3$ that were already excluded in Sects. 4.1 and 4.2.1.

*Thus, the improved $H_\alpha$ -diagnostics reveal another systematic defect of the present theory that would have been hidden if the simplified method had been applied.*

### 4.2.3. Wind momentum in the Magellanic Clouds

Figure 30 compare the empirical wind momentum-luminosity-relations for SMC and LMC with model calculations for the individual objects. While the results for the LMC do not seem to indicate a severe discrepancy, we find some clearly discrepant cases at $\log L/L_\odot \approx 5.75$ in the SMC.

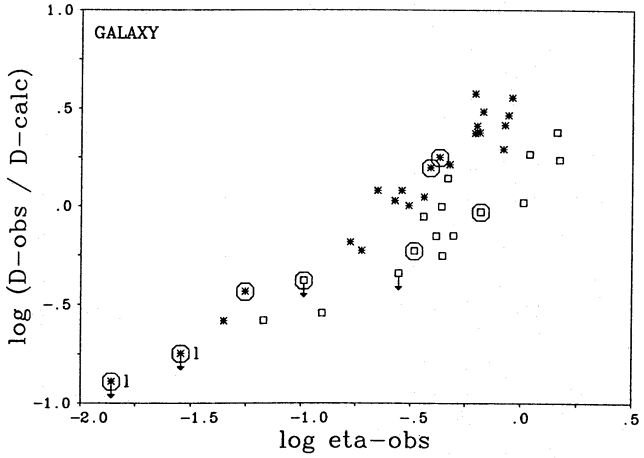


**Fig. 29.** Difference of observed logarithmic momentum rate determined by the improved method developed in this paper and predictions of the improved theory as described by Pauldrach et al. (1994). Targets and observed values are identical to those of Fig. 22b. Asteriks: $T_{\rm eff} < 40,000$ K; squares: $T_{\rm eff} \geq 40,000$ K. Objects with $\log L/L_{\odot} < 5.3$ are identified by an additional "l"

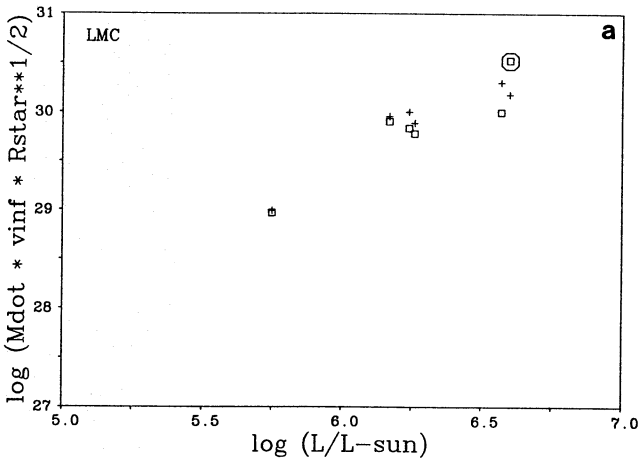


**Fig. 30. a** Observed wind momentum rate in the LMC (squares) as function of luminosity compared to model computations (crosses)

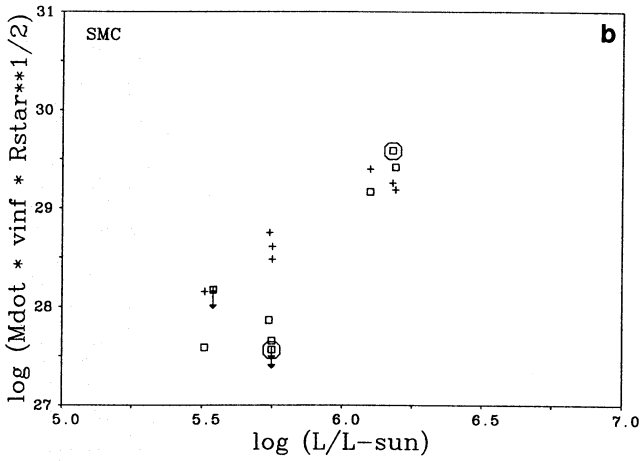


**Fig. 30. b** As **a**, but for the SMC

The situation becomes much clearer as soon as we compare again the differences between observation and theory as function of observed $\eta$ (Fig. 31). The trend in the LMC is comparable (although not very obvious) to the Galaxy, which in view of the only small difference in abundance is not surprising. In the SMC there is certainly a trend with $\eta$, where the two different regimes seem to be divided now at $T_{\rm eff} \approx 45,000$ K.

The fact that we see the similar systematic failure of wind theory in the SMC and LMC assures that this is not an artefact caused by uncertain distances for the galactic O-stars. The problem is real, unfortunately.

## 5. Discussion

Together with the most important diagnostic results of this study we like to discuss two issues that we regard as important, namely the reliability of the $H_\alpha$ -method and the status of radiation driven wind theory.

We think that the method introduced in this paper is superior to previous ones using $H_\alpha$, as it avoids systematic errors arising from the use of the Sobolev approximation or the assumption of purely optically thin emission and as it is still fast and effective compared with the complex calculations of unified atmospheres. On the other hand, we should not forget other possible sources for systematic errors. In our view, the most important ones are clumpiness (and variability) of the winds and deviations from spherical symmetry because of rotation. While a discussion of the present status of time dependent radiation-hydrodynamical calculations led us to the conclusion to neglect clumpiness, we still feel that this is an area that will require very careful observational and theoretical investigations in the future. The same is true with rotation. We feel that it is certainly time to reconsider the diagnostics of rapidly rotating O-stars in terms of two-dimensional disk-like structures following and extending the ideas by Bjorkman & Cassinelli (1993). So far, we have neglected these kinds of processes.

Another effect on the diagnostics that was also ignored by us is the influence of line blocking on the $H_\alpha$ occupation numbers. While the work by Schaerer & Schmutz (1994) and comparable calculations ongoing in our group indicate that the effects are small, a detailed and thorough investigation is certainly required.

Despite these uncertainties, we agree with Klein & Castor (1978), Leitherer (1988) and Lamers & Leitherer (1994), who have pioneered the systematic $H_\alpha$ -studies, that the investigation of $H_\alpha$ -profiles is the best way to determine mass-loss rates of a large sample of O-stars.

Two outstanding results of this study are the existence of the wind momentum-luminosity relation and the derivation of the wind velocity gradient. As for the latter, we have found that the velocity field exponent $\beta$ is larger than usually adopted, which is important for any kind of further line profile and continuum

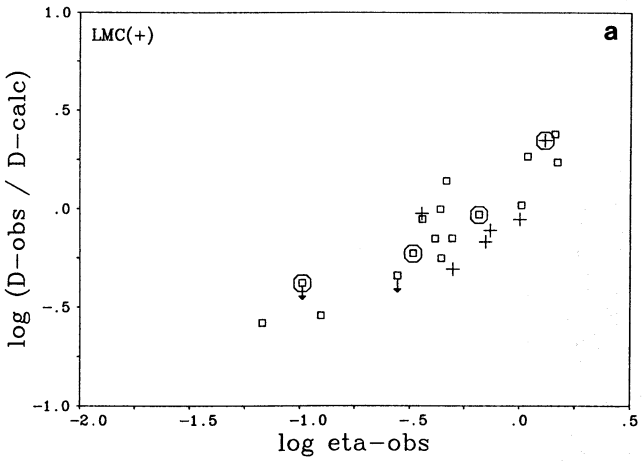


**Fig. 31. a** Difference of logarithmic wind momentum rate between observation and theory as function of observed wind performance number. Squares: Objects in the Galaxy with $T_{\rm eff} \geq 40,000$ K; crosses: LMC objects (all well above 40,000 K)

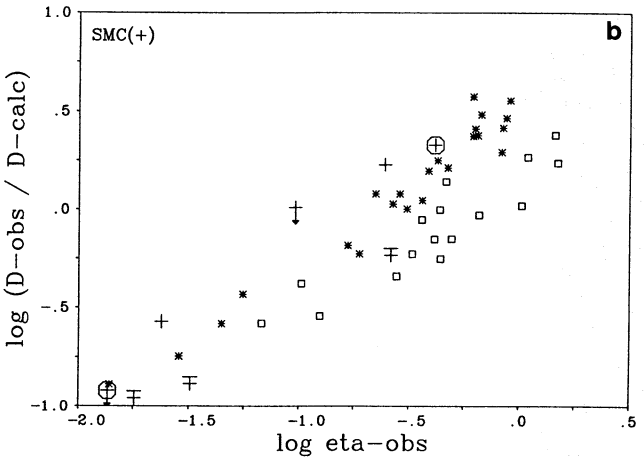


**Fig. 31. b** As **a**, but squares: galactic objects with $T_{\rm eff} \geq 40,000$ K; asterisks: galactic objects with $T_{\rm eff} < 40,000$ K; crosses: SMC (objects with $T_{\rm eff} \geq 45,000$ K indicated by a bar. (For convenience, the indication of rapid rotators and upper limits of $\dot{M}$ for *galactic* objects is suppressed)

diagnostics. Unfortunately, our radiation driven wind models are not able to reproduce this value.

The tight wind momentum-luminosity-relation that we have found, in particular for supergiants, is another important result. In this connection we readily acknowledge that the investigation of this relation in terms of radiation driven wind scaling relations was triggered by the work of Lamers & Leitherer (1994). The fact that this relation can – at least qualitatively – be understood in terms of radiation driven winds is certainly a triumph of the theory. The fact that there are quantitative discrepancies is a challenge for the future.

Astronomically, the wind momentum-luminosity-relation has great potential for further astrophysical applications such as extragalactic distance determinations. The possibility to investigate the metallicity dependence of this relation by means of massive stars in the Magellanic Clouds will enable us to widen the applicability of the method enormously.

A shock for a stellar wind theoretist is our final result that, indeed, the theory shows a systematic defect as function of wind performance number $\eta$. Again, we need to express an acknowledgement to Lamers & Leitherer (1994), who were the first to investigate this idea. The fact that, after five years of continuous work to improve line lists, atomic physics and models and to include additional effects like shock induced EUV radiation etc. we find such a clear systematic discrepancy is disappointing. On the other hand, there is a clear indication of where the reason for this systematic failure might lie.

We are convinced that the reason is the inadequate treatment of line overlap or "multi-line effects". Puls (1987) has already investigated this problem approximately for a wind of rather low $\eta$ and found a reduction of wind momentum due to enhanced backscattering and blocking of photons between the sonic and critical points. We speculate that this effect might be enhanced towards even smaller $\eta$-values thus indicating that our procedure to account for pure photospheric blocking only might be intrinsically erroneous. For large $\eta$-values the effects of multiple photon momentum transfer combined with shifts in the ionization stratification as proposed by Lucy & Abbott (1993) and recently reanalyzed semi-analytically by Springmann (1994) might explain the failure of the theory in the other direction. In any case, there remains much work to be done in this field.

*Acknowledgements.* We gratefully acknowledge the following grants to A. Herrero (DAAD,"acciones integradas Hispano Alemas" 1990-1992; Alexander von Humboldt Stiftung), A.W.A. Pauldrach, S.M. Haser and A. Feldmeier (DFG, Pa 477/1-2 in the "Gerhard-Hess-Programm"), D.J. Lennon and R. Gabler (BMFT 50 OR 93040) and S.A. Voels (DARA 50 OS 9002-ZA). We wish to thank Ian D. Howarth and Raman K. Prinja for kindly providing us with their sample of 203 IUE spectra of galactic O-stars. We are also indebted to Claus Leitherer for providing us with his $H_\alpha$ profiles for those stars in common with our dataset for comparison.

## Appendix A: the different structure of unified and hydrostatic model atmospheres and an estimate of its influence on the $\log g$ determination

Figure 16 demonstrates the influence of stellar winds on the atmospheric density structure. If this difference is still significant at the $H_\gamma$ continuum optical depth $\tau_c \approx 2/3$, then the use of a hydrostatic model to calculate the Stark broadened wings of $H_\gamma$ will yield an *underestimate* of the stellar gravity. In this appendix we provide a simple first order estimate of the effect.

For approximating the density structure down to layers of the formation of the $H_\gamma$ wings it is sufficient to adopt a constant kinetic temperature. For the hydrostatic case we then have

$$\rho_{\rm stat}(g,m) = \frac{1}{v_{\rm sound}^2} \int_0^m (g - g_{\rm rad}) {\rm d}m, \qquad \text{(A1)}$$

where $v_{\rm sound}$ is the isothermal sound speed, $g_{\rm rad}$ the radiative acceleration and $m$ the column mass as defined in Eq. (53).

For estimating the density in the unified model we adopt the $\beta$-law (Eqs. 16,17) down to a velocity $v_0$ which via the equation of continuity yields

$$\rho_{\rm unif} = \bar{\rho}\frac{1}{r^2(1-b/r)^\beta},\ r \geq 1,\ v \geq v_0 \tag{A2}$$

$$\bar{\rho} = \frac{\dot{M}}{4\pi R_*^2 v_\infty}. \tag{A3}$$

For velocities smaller than $v_0$ we then adopt a hydrostatic structure

$$\rho_{\rm unif}(g,m) = \frac{1}{v_{\rm sound}^2}\int_{m_0}^{m}(g-g_{\rm rad})\mathrm{d}m + \rho_0 \tag{A4}$$

$$\rho_0 = \rho_{\rm unif}(r=1) = \bar{\rho}\frac{v_\infty}{v_0}$$

$$m_0 = \bar{\rho}\,R_*\,h_1(b,\beta) \tag{A5}$$

$$h_1 = \begin{cases} -\frac{1}{b}\ln(1-b), & \beta = 1 \\ \frac{1}{b}\frac{1}{1-\beta}\left[1-\left(\frac{v_0}{v_\infty}\right)^{\frac{1-\beta}{\beta}}\right], & \beta \neq 1 \end{cases}$$

$m_0$ is the column mass at $r = 1$, $v = v_0$ obtained from (A2). Comparing with numerical results of unified models we found that (A2) and (A4) are good approximations of the density stratification.

To estimate the densities at $\tau_c = 2/3$ we need to determine $m_c$ defined by

$$\frac{2}{3} = \int_0^{m_c}\frac{n_e\sigma_E + \kappa_{\rm true}}{\rho}\mathrm{d}m = a_1 m_c + a_2\int_0^{m_c}\rho\mathrm{d}m \tag{A6}$$

where $\kappa_{\rm true}$ is the free-free and bound-free continuum absorption coefficient at $H_\gamma$ . $a_1$ is given by

$$a_1 = \frac{\sigma_E}{m_p}\frac{1+I_{He}Y}{1+4Y}. \tag{A7}$$

If we approximate $\kappa_{\rm true}$ by its LTE-value and consider only hydrogen and helium opacity, we can express $a_2$ by

$$a_2 = \frac{f(T,Y)}{m_p^2}\frac{1+I_{He}Y}{(1+4Y)^2}, \tag{A8}$$

where the function $f$ contains the temperature and Saha-Boltzmann-factor weighted contributions of hydrogen and helium free-free and bound-free cross-sections and can be easily calculated.

To perform the integrals in (A2) and (A4) we need an estimate of $g_{\rm rad}$ in the subsonic regions. The obvious approximation is

$$g_{\rm rad} \approx g_{\rm Th} = a_1\frac{\sigma_B T_{\rm eff}^4}{c} \tag{A9}$$

with $g_{\rm Th}$ the acceleration by Thomson scattering. We note that around $\tau_c = 2/3$ this is generally a severe underestimate of $g_{\rm rad}$ because of the significant free-free and bound-free acceleration. However, for estimating the relative difference between the density of a unified and a hydrostatic model Eq. (A9) is still sufficient. We then obtain for the densities at $\tau_c = 2/3$

$$\rho_{2/3}^{\rm stat} = \frac{g-g_{\rm Th}}{v_{\rm sound}^2}m_c^{\rm stat} \tag{A10}$$

$$\rho_{2/3}^{\rm unif} = \frac{g-g_{\rm Th}}{v_{\rm sound}^2}(m_c^{\rm unif}-m_0)+\rho_0. \tag{A11}$$

For (A11) we have assumed that $\dot{M}$ is still small enough to ensure $m_c^{\rm unif} > m_0$. For the column mass $m_c$ at $\tau_c = 2/3$ we obtain the quadratic equations

$$\frac{2}{3} = a_1 m_c^{\rm stat} + \frac{1}{2}\frac{a_2}{v_{\rm sound}^2}(g-g_{\rm Th})(m_c^{\rm stat})^2 \tag{A12}$$

$$\frac{2}{3} = \tau_0 + (a_1+a_2\rho_0)(m_c^{\rm unif}-m_0) + \frac{1}{2}\frac{a_2}{v_{\rm sound}^2}(g-g_{\rm Th})(m_c^{\rm unif}-m_0)^2 \tag{A13}$$

$$\tau_0 = a_1 m_0 + a_2\bar{\rho}^2 R_* h_2(b,\beta) \tag{A14}$$

$$h_2 = \begin{cases} \frac{1}{b^3}\left[\frac{1}{1-b}+2\ln(1-b)-(1-b)\right], & \beta = 1 \\ \frac{1}{b^3}\left[1+\frac{(b-1)(1+b+b^2-2b\beta-3b^2\beta+2(b\beta)^2}{(1-b)^{2\beta}}\right] \times & \\ \times\left[(1-\beta)(3-2\beta)(1-2\beta)\right]^{-1}, & \beta \neq 1 \end{cases} \tag{A15}$$

The difference between $\rho_{2/3}^{\rm stat}$ and $\rho_{2/3}^{\rm unif}$ for given gravity, mass-loss rate and terminal velocity can be easily calculated from Eqs. (A10) to (A15). A comparison with calculated unified and hydrostatic models shows that this gives the right order of magnitude.

To estimate the influence of the density effect on the determination of spectroscopic gravities from $H_\gamma$ , we assume that we need different gravities $g_{\rm unif}$ and $g_{\rm stat}$ to fit the density $\rho_{2/3}^{\rm obs}$ from $H_\gamma$ . Thus, by requiring

$$\rho_{2/3}^{\rm unif}(g_{\rm unif}) = \rho_{2/3}^{\rm stat}(g_{\rm stat}) = \rho_{2/3}^{\rm obs}$$

we obtain from Eqs. (A10, A11)

$$(g_{\rm unif}-g_{\rm Th}) = (g_{\rm stat}-g_{\rm Th})\frac{m_c^{\rm stat}}{m_c^{\rm unif}-m_0} - \frac{\rho_0 v_{\rm sound}^2}{m_c^{\rm unif}-m_0}. \tag{A16}$$

These corrections together with the centrifugal correction (Herrero et al. 1992) were applied to column 4 in Table 8 to obtain the values of column 5.

## References

Abbott D.C., 1982, ApJ 259, 282
Abbott D.C., Bieging J.H., Churchwell E., 1981, ApJ 250, 645
Bjorkman J.E., Cassinelli J.P., 1993, ApJ 409, 429
Bohannan B., Voels S.A., Hummer D.G., Abbott D.C., 1990, ApJ 365, 729

Butler K., Giddings J.R., 1985, Coll. Comp. Project No. 7 (CCP7), Newsletter 9, London, p. 7
Cassinelli J.P., Cohen D.H., MacFarlane J.J., Sanders W.T., Welsh B.Y., 1994, ApJ 421, 705
Castor J.I., 1970, MNRAS 149, 111
Castor J.I., Abbott D.C., Klein R.I., 1975, ApJ 195, 157
Chlebowski T., Harnden F.R., Sciortino S., 1989, ApJ 341, 427
de Koter A., Schmutz W., Lamers H.J.G.L.M., 1993, A&A 277, 561
Drew J.E., 1990, ApJ 357, 573
Ebbets D., 1982, ApJS 48, 399
Feldmeier A., 1995, A&A, in press
Friend D.B., Abbott D.C., 1986, ApJ 311, 701
Gabler A., Gabler R., Pauldrach A.W.A., Puls J., Kudritzki R.P., 1990, in: Garmany C.D. (ed.) Properties of Hot Luminous Stars, Boulder-Munich Workshop. PASPC 7, San Francisco, p. 218
Gabler R., Gabler A., Kudritzki R.P., Puls J., Pauldrach A.W.A., 1989, A&A 226, 162
Gabler R., Gabler A., Kudritzki R.P., Puls J., Pauldrach A.W.A., 1990, in: Garmany C.D. (ed.) Properties of Hot Luminous Stars, Boulder-Munich Workshop. PASPC 7, San Francisco, p. 64
Giddings J.R., 1980, Ph.D. Thesis, University of London
Groenewegen M.A.T., Lamers H.J.G.L.M., 1989, A&AS 79, 359
Hamann W.-R., 1981, A&A 93, 353
Haser S.M., 1995, PhD thesis, Universität München, in preparation
Haser S.M., Lennon D.J., Kudritzki R.P., Puls J., Walborn N.R., Bianchi L., Hutchings J.B., 1994, Sp. Sci. Rev. 66, 179
Haser S.M., Pauldrach A.W.A., Kudritzki R.P., Lennon D.J., Gabler R., Puls J., 1994a, AG Abstract Series 10, 199
Haser S.M., Lennon D.J., Kudritzki R.P., Puls J., Pauldrach A.W.A., Bianchi L., Hutchings J.B., 1995, A&A, in press
Hayes D.P., 1975, ApJ 197, L55
Heap S.R., Altner B., Ebbets D., Hubeny L., Hutchings J.B., Kudritzki R.P., Voels S.A., Haser S., Pauldrach A., Puls J., Butler K., 1991, ApJ 377, L29
Henrichs H.F., 1991, in: Baade D. (ed.) Rapid Variability of OB-Stars, ESO Conference Proc. 36. ESO, Garching, p. 199
Henrichs H.F., Kaper L., Nichols J.S., 1994, A&A 285, 565
Herrero A., 1994, in: Vanbeveren D., van Rensbergen W., de Loore C. (eds.) Evolution of Massive Stars. Kluwer, Dordrecht, p. 137
Herrero A., Kudritzki R.P., Vilchez J.M., Kunze D., Butler K., Haser S.M., 1992, A&A 261, 209
Heydari-Malayeri M., Hutsemékers D., 1991, A&A 243, 401
Hillier D.J., Jones, T.J., Hyland, A.R., 1983, ApJ 271, 221
Hillier D.J., Kudritzki R.P., Pauldrach A.W., Baade D., Cassinelli J.P., Puls J., Schmitt J.H.M.M., 1993, A&A 276, 117
Howarth I.D., Prinja R.K., 1989, ApJS 69, 527
Howarth I.D., Reid A.H.N., 1993, A&A 279, 148
Husfeld D., Butler K., Heber U., Drilling J.S., 1989, A&A 222, 150
Klein R.I., Castor J.I., 1978, ApJ 220, 902
Kudritzki R.P., 1980, A&A 85, 174
Kudritzki R.P., 1992, A&A 266, 395
Kudritzki R.P., Hummer D.G., 1990, ARAA 28, 303
Kudritzki R.P., Pauldrach A., Puls J., 1987, A&A 173, 293
Kudritzki R.P., Pauldrach A., Puls J., 1988, in: Conti P.S., Underhill A.B. (eds.) Monograph Series on Nonthermal Phenomena in Stellar Atmospheres – O Stars and Wolf-Rayet Stars. NASA SP-497, Washington, D.C., p. 173
Kudritzki R.P., Pauldrach A., Puls J., Abbott D.C., 1989, A&A 219, 205
Kudritzki R.P., Hummer D.G., Pauldrach A.W.A., Puls J., Najarro F., Imhoff J., 1992, A&A 257, 655
Kudritzki R.P., Lennon D.J., Becker S.R., Butler K., Gabler R., Haser S., Hummer D.G., Husfeld D., Pauldrach A.W.A., Puls J., Voels S., Walborn N.R., Heap S.R., Bohannan B., Conti P., Garmany C.D., Baade D., 1992a, in: Benvenuti P., Schreier E. (eds.) Science with the Hubble Space Telescope. ESO, Garching, p. 279
Kudritzki R.P., Lennon D.J., Puls J., 1995, in: Walsh J.R., Danziger I.J. (eds.) Science with the Very Large Telescope. ESO, Garching, in press
Lamers H.J.G.L.M., Leitherer C., 1993, ApJ 412, 771 (L&L)
Lamers H.J.G.L.M., Waters L.B.F.M., 1984, A&A 138, 25
Lamers H.J.G.L.M., Cerruti-Sola M., Perinotto M., 1987, ApJ 314, 726
Langer N., Hamann W.-R., Lennon M., Najarro F., Pauldrach A.W.A., Puls J., 1994, A&A 290, 819
Leitherer C., 1988, ApJ 326, 356
Leitherer C., 1988a, ApJ 334, 626
Leitherer C., Robert C., 1991, ApJ 377, 624
Lennon D.J., Dufton P.L., Fitzsimmons A., 1993, A&AS 97, 559
Lucy L.B., 1982, ApJ 255, 278
Lucy L.B., 1984, ApJ 284, 351
Lucy L.B., Abbott D.C., 1993, ApJ 405, 738
Lupie O.L., Nordsieck K.H., 1987, AJ 92, 214
Moffat A.F.J., Robert C., 1994, ApJ 421, 310
Owocki S.P., 1991, in: Crivellari L., Hubeny I., Hummer D.G. (eds.) Stellar Atmospheres, Beyond Classical Models. Kluwer, Dordrecht, p. 235
Owocki S.P., 1992, in: Heber U., Jeffery S. (eds.) The Atmospheres of Early-Type Stars. Springer-Verlag, Heidelberg, p. 393
Owocki S.P., 1995, in: Moffat A.F.J., Fullerton A.W., Owocki S.P., St-Louis N. (eds.) Instability and Variability of Hot Star Winds. Kluwer, Dordrecht (in press)
Owocki S.P., Rybicki G.B., 1985, ApJ 299, 265
Panagia N., 1988, in: Pudritz R.E., Fich M. (eds.) Galactic and Extragalactic Star Formation. Kluwer, Dordrecht, p. 25
Panagia N., Felli M., 1975, A&A 39, 1
Pauldrach A., Puls J., Kudritzki R.P., 1986, A&A 164, 86
Pauldrach A.W.A., Kudritzki R.P., Puls J., Butler K., 1990, A&A 228, 125
Pauldrach A.W.A., Kudritzki R.P., Puls J., Butler K., Hunsinger J., 1994, A&A 283, 525
Prinja R.K., Balona L.A., Bolton C.T., Crowe R.A., Fieldus M.S., Fullerton A.W., Gies D.R., Howarth I.D., McDavid D., Reid A.H.N., 1992, ApJ 390, 266
Puls J., 1987, A&A 184, 227
Puls J., Owocki S.P., Fullerton A.W., 1993, A&A 279, 457
Puls J., Pauldrach A.W.A., Kudritzki R.P., Owocki S.P., Najarro F., 1993a, in: Klare G. (ed.) Reviews in Modern Astronomy 6. Astronomische Gesellschaft, Hamburg, p. 271
Puls J., Feldmeier A., Springmann U., Owocki S.P., Fullerton A.W., 1995, in: Moffat A.F.J., Fullerton A.W., Owocki S.P., St-Louis N. (eds.) Instability and Variability of Hot Star Winds. Kluwer, Dordrecht (in press)
Reid A.H.N., Bolton C.T., Crowe R.A., Fieldus M.S., Fullerton A.W., Gies D.R., Howarth I.D., McDavid D., Prinja R.K., Smith K.C., 1993, ApJ 417, 320
Robert C., Moffat A.F.J., 1990, in: Garmany C.D. (ed.) Properties of Hot Luminous Stars, Boulder-Munich Workshop. PASPC 7, San Francisco, p. 271
Schaerer D., Schmutz W., 1994, A&A 288, 231
Scuderi S., Bonanno G., Di Benedetto R., Spadaro D., Panagia N., 1992, ApJ 392, 201

Sellmaier F., Puls J., Kudritzki R.P., Gabler R., Gabler A., Voels S.A., 1993, A&A 273, 533
Shortridge K., 1987, Figaro User Manual
Springmann U., 1994, A&A 289, 505
Springmann U.W.E., Pauldrach A.W.A., 1992, A&A 262, 515
Stahl O., Wolf B., Klare G., Cassatella A., Krautter J., Persi P., Ferrari-Toniolo M., 1983, A&A 127, 49
Vogt S.S., Penrod G.D., 1983, ApJ 275, 661
Walborn N.R., Lennon D.J., Haser S.M., Kudritzki R.P., Voels S.A., 1995, PASP, in press
Wright A.E., Barlow M.J., 1975, MNRAS 170, 41

This article was processed by the author using Springer-Verlag LaTeX A&A style file version 3.